Nanophotonic Systems for Novel Applications: From Spaceflight to Self-Assembled Materials to Thermal Radiation

By

Joel Franklin Siegel

A dissertation submitted in partial fulfillment of the requirements for the degree of

Doctor of Philosophy
(Physics)

at the
University of Wisconsin-Madison
2022

Date of final oral examination: August 4, 2022
This dissertation is approved by the following members of the Final Oral Committee:
Victor W. Brar, Professor, Physics
Mikhail A. Kats, Professor, Electrical and Computer Engineering
Padma Gopalan, Professor, Materials Science and Engineering
Shimon Kolkowitz, Professor, Physics

Abstract

The optical properties of a material can be altered by structuring the material with features on the order of the wavelength of interest. This patterning allows for materials to be designed with a targeted optical property, which can be used for any number of potential applications. The focus of this dissertation is a discussion on how the same fundamental principles of light manipulation can be applied to multiple distinct objectives, ranging from interstellar to the nanoscale. In the first section of the dissertation, there will be a discussion on how the microscopic optical forces exerted on a metasurface lightsail propelled by a high-power laser can be engineered via its optical properties to achieve passive self-stabilization, such that the sail is trapped inside the drive beam. In the second section of this dissertation, there will be a discussion on development of a large-scale nanofabrication technique of narrow (< 15 nm) graphene resonators based on block copolymer lithography and how the characteristic scaling laws of resonant graphene plasmons change for these narrow resonators. Additionally, there is a discussion on some potential avenues towards incorporating these into more complex optical designs. In the final section of the dissertation, a method to electronically change the angle of thermal emission from a device based on graphene is discussed.

For Zagreus, Winnie, Maddie, Polly, and all the other pets that support us through our lives

Acknowledgements

When I saved my acknowledgement section for last, I thought it would be the easiest part of my dissertation to write. But it ended up being the complete opposite. There are so many people who have helped me on my journey that I struggle to condense it to even a few pages. My success is only due to the support I received from everyone around me. So before I go into specifics, I want to say thank you. To everyone who helped me reach the monumental goal of earning my doctorate in physics.

The first person I want to thank, which should come as no surprise, is my advisor, Victor Brar. It was my absolute honor and privilege to join Victor's lab as his first graduate student (alongside Wyatt Behn). I still remember the moment I made my decision, it was when Victor had asked if I wanted to work on a laser sail. I knew nothing about laser sails, spacecraft, or nanophotonics (which would eventually become my dissertation topic!), but how could I turn down an opportunity to turn something from science fiction into reality? And I think that is always what I admired the most about Victor: he was always looking forward and willing to try something new. His curiosity was infectious and represented the best of what a scientist should be and I will always strive to follow the example that he set. Victor was a wonderful mentor during my graduate studies, from providing direct support early on to giving me freedom to perform research on my own as I developed my skills.

The next person I would like to thank is Mikhail Kats, an unofficial advisor of mine. His patience and support served as the bedrock to my research and I am extremely grateful to have worked with him. Even more than that, Mikhail helped me grow an important, but sometimes neglected skill, clarity. If anything was unclear during a talk, Mikhail would almost certainly ask about it, never in a negative manner, but because he was invested and

curious. Some of my proudest moments were being able to present something to him *without* any questions.

About half of my dissertation work is based on simulation work and the other half is taking measurements in the Kats' lab FTIR, so I feel that it is important to acknowledge everyone who helped me. The first person to thank would be Anthony Wang, a post-baccalaureate who started with our lab right after I joined. Working together, we were able run all sorts of simulations, up to that of a self-stabilizing laser sail. I also want to thank the Kats group and specifically Jad Salman, Alireza Shahsafi, Ray Wambold, Chenghao Wan, and Yuzhe Xiao for all of their assistance in answering my many Lumerical questions and teaching me how to use the FTIR, a tool without which, most of my PhD would be impossible.

Another large portion of my work is only thanks to the efforts of Padma Gopalan and her graduate students. Their expertise in block copolymer lithography served as the basis for one of my largest research projects, which could never have been accomplished without their assistance. Specifically, I want to thank Jonathan Dwyer, who developed the fabrication technique used in the graphene nanoribbon publication, Anjali Suresh, who assisted Jonathan in the development, and Jian Sun, who not only took over for Jonathan after he graduated, but worked with me to advance our work in new areas.

My work also gave me the opportunity for some international collaborations with Professor Min Seok Jang's group in South Korea. Sergey Menabde was an integral part of the laser sail portion of my dissertation and Shinho Kim created the theory behind the thermal steering device.

My work could also not have been accomplished without the assistance of the WCAM staff and their fabrication expertise. Kurt Kupcho, Frank Flack, and Ed Blucher were the main staff members I trained with and went to for help.

But I would be remiss if I did not highlight and thank the contributions of my very own group members. Margaret Fortman for always being willing to transfer graphene onto whatever weird substrate I produced, Keenan Smith for indulging my curiosity about whatever Van-der Waals material stacks he was making, Colin Whisler for explaining complex the-

ory in a manageable way, Zach Krebs for patiently explaining the interesting images on the STM computer, Greg Holdman for being a sounding board for all manner of ideas, whether simulation or experimental, Gabrial Jaffe for his fabrication expertise, and Seyoon Kim for his advice on challenging photonics simulations.

I'd like to give special thanks to my coworker and friend Wyatt Behn. Wyatt was one of the first friends I made in graduate school (first day too I believe) and he helped me get through the best and worst of it all, from spending hours together studying for the quals to living with each other during the Covid pandemic (and for a few years before that) to introducing me to all sorts of fun podcasts and other entertainment. And of course, thank you for introducing me to Ned, a fantastic kitty, who would inspire me to adopt a cat of my own.

On the topic of friends, I must mention one of my most treasured friend groups, my DND group: Harry Hausner, Miranda Waldman[1], Andrew Loeliger, Jocelyn Bock , Shoshana Rudin, and Michael Cervia. Our weekly DND sessions served as one of the most grounding experiences of my graduate career, a bit ironic considering we were playing a fantasy game. But you all were a wonderful group of people full of love and support that served as constant reminder that no matter what, I was not alone. It was an honor to DM for all of you and thank you for always being willing to have fun.

The last group of people that I want to thank are my family. Through it all, I've always been able to rely on them to be there when I needed it. I want to thanks to my sisters, Anna and Elizabeth, and brother-in-law, Dave, for helping me out with the many, many things outside my field of expertise. To Dad, thank you for always encouraging me to ask why and for explaining even complex things to me as a child. You taught me that I should never be afraid to try to understand the world around me and that is a lesson that has carrier me through my life. To Mom, thank you for always being willing to listen, even if most of the stuff I talked about made no sense to you. You were always there when I needed you and you taught me that not only is it ok to struggle, but how to work through it.

[1]I was also honored to officiate the wedding of Harry and Miranda

Finally, I want to give special thanks to Zagreus, my cat. Though I will only have had him for a year at the time of writing, he made what was certainly one of the most challenging years of my life significantly easier. I love you buddy.

Table of Contents

List of Tables

List of Figures

Chapter 1

Introduction

Nanophotonics is a field of study focused on the interaction of light with materials at a length-scale comparable to the light. Of particular interest is the ability of structured materials to control these interactions, and consequently the magnitude, phase, and polarization of light in the near and far-field [1–9]. This can be accomplished with nanostructuring of metals, dielectrics, semiconductors, 2D materials, etc., though the exact mechanism behind the interactions is material dependent. The field of nanophotonics has grown rapidly in recent years due to the advancements in fabrication technologies and the proliferation of simulation methods to solve Maxwell's equations over arbitrarily complex structures, allowing for more innovative methods to manipulate light beyond the conventional bulky optical components.

The interactions of light with a material comes fundamentally from its atomic composition, structure (crystalline, amorphous, etc.), and electronic properties [3, 10]. These various effects can be summarized by the frequency dependent (also known as the dispersive) permittivity

$$\epsilon(\omega) = \epsilon'(\omega) - i\epsilon''(\omega) \tag{1.1}$$

where ϵ' and ϵ'' are the real and imaginary parts of the refractive index and ω is the frequency of light. The permittivity of a material can also be given in relation to the free space permittivity, ϵ_0, by $\epsilon = \epsilon_r\epsilon_0$, where ϵ_r is the relative permittivity of the material. Furthermore, the permittivity is closely related to the refractive index of a material, n, via the relation

$$n = \sqrt{\epsilon_r\mu_r} \tag{1.2}$$

where μ_r is the relative permeability. All materials discussed in this work are non-magnetic at the relevant frequencies (and the majority of materials fall under this category), so μ_r is approximated as 1. A refractive index is generally used when considering Snell's law type calculations, whereas permittivity is used in Maxwell's equation calculations. These optical properties are based on the bulk material's interaction with light, but the interactions with light can be adjusted by additional structuring of the material [3–6]. The same way that the atomic structure determines the optical properties of a material (graphite and diamond are both carbon crystals, but the two materials are optically distinct), so too does the macroscopic structure affect the optical properties of a material.

1.1 Metamaterials

In the simplest case, the optical properties of a structured material would become a weighted average of the properties of the bulk material and vacuum (representing the removed sections), referred to as an effective medium. This effective medium can allow for a larger range of optical "materials" and can include multiple materials in various ratios. The properties of these composite materials are still fundamentally limited to what exists in nature as any resultant refractive index will just be a ratio of existing material properties. The effective medium approximation is valid under the assumption that while a material may be macroscopically heterogeneous as a mixture of materials, the electromagnetic field interactions behave as though it is a homogeneous material[3].

That situation can change though if the strfffuctured material exhibits a resonance that induces a new optical property in the constituent materials, breaking the homogeneity assumption of the effective medium. The sub-wavelength structuring allows for the optical properties to be dramatically altered to create a *metamaterial* or - for flat geometries *metasurface*. The base elements of these patterns are sometimes referred to as meta-atoms as they behave similar to how the atom and its resonances form the basis of a material. No longer limited to the atomic building blocks found in nature, these meta-atoms enable the design of metamaterials with arbitrary optical properties [3, 6, 11].

Metamaterials and metasurfaces can be made from many materials, such as dielectrics [4], or metals [5]. Recent advances in nanofabrication as well as optical design tools have allowed for the creation of metamaterials that can replace conventional bulky optics such as spherical lenses[12], beam steerers[5], and mirrors [4] to more advanced optics with no conventional counterpart such as holograms[13] or invisibility cloaks[9]. Metamaterials can be active as well by incorporating materials that can dynamically change the optical properties of the structure whether it is through mechanical [14, 15], temperature[16, 17], or electronic [18–20] means.

1.2 Plasmonics

One popular method in nanophotonics to manipulate light is through the use of a surface plasmonic resonance, a hybridization of a photon and charge carrier oscillation. A surface plasmon is an electron density wave traveling across the interface of a dielectric/heavily doped material (traditionally a metal, but other materials may satisfy the conditions as discussed below) boundary as shown in Figure 1.1. When light with an appropriate wavevector interacts with the interface, the electromagnetic wave will cause electrons to form a charge oscillation that travels across the surface, generating electromagnetic fields in the doped material and dielectric [10, 21]. Plasmons can also be excited in the bulk doped material, referred to as bulk plasmons, but these plasmons are significantly shorter lived than their surface counterparts and are not considered in this work. In the most general case, a surface plasmon can be formed from the propagating mode on the interface between a semi-infinite conductor and dielectric, though more complex geometric configurations are possible (such as metallic nanoparticles surrounded by a dielectric).

For this general case, the surface plasmon can be solved using Maxwell's equations when excited with transverse magnetic (TM) polarized light, though only the essential steps will be shown here. We start with Maxwell's equations

$$\nabla \cdot D = \rho_{ext}, \tag{1.3}$$

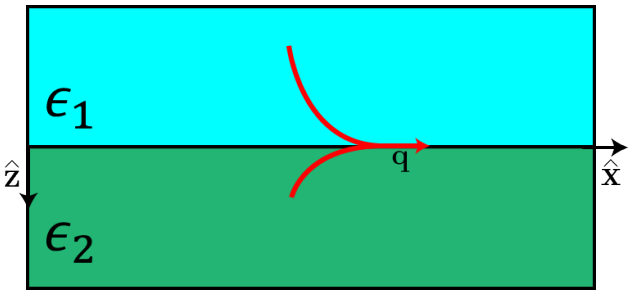

Figure 1.1: Cartoon schematic of surface plasmon at the interface of two materials. The field profile is shown with the plasmon (q) assuming ϵ_1 is a dielectric and ϵ_2 is a metal

$$\nabla \times H = \frac{\partial D}{\partial t} + J_{ext}, \tag{1.4}$$

$$\nabla \times E = -\frac{\partial B}{\partial t}, \tag{1.5}$$

$$\nabla \cdot B = 0, \tag{1.6}$$

where H denotes the magnetic field, B denotes the magnetic induction, E denote the electric field, D denotes the electric displacement, and ρ_{ext}/J_{ext} denote the free charge/current densities.

For TM polarized light, the solutions to the electric and magnetic fields can be written as follows,

$$E_j(x,y,z,t) = (E_{j,x}\hat{\boldsymbol{x}} + E_{j,z}\hat{\boldsymbol{z}})e^{-\kappa_j|z|}e^{i(qx-\omega t)} \tag{1.7}$$

$$B_j(x,y,z,t) = B_{j,y}\hat{\boldsymbol{y}}e^{-\kappa_j|z|}e^{i(qx-\omega t)} \tag{1.8}$$

where the index j = 1,2 denotes the medium, κ_j is the z component of the wavevector, q is the x component of the wavevector (due to continuity at the interface, $q_1 = q_2 = q$), and ω is the frequency of light. The wavevector components must additionally satisfy the following condition

$$\kappa_j^2 + q^2 = \epsilon_j(\frac{\omega}{c})^2 \tag{1.9}$$

By taking into account that there must be continuity of the tangential components of the electric and magnetic fields at the interface (z=0), i.e.

$$E_{1,x} = E_{2,x} \tag{1.10}$$

$$B_{1,y} = B_{2,y} \tag{1.11}$$

and substituting our equations of the TM field into Maxwell's equations, it is possible to arrive at the following set of simplified equations:

$$E_{1,x} = E_{2,x}, \tag{1.12}$$

$$\frac{\epsilon_1}{\kappa_1} E_{1,x} = \frac{\epsilon_2}{\kappa_2} E_{2,x}, \tag{1.13}$$

From these equations and some linear algebra not shown, the dispersion relation of the TM can be solved to return the result as follows

$$\frac{\epsilon_1}{\kappa_1} + \frac{\epsilon_2}{\kappa_2} = 0 \tag{1.14}$$

For the electromagnetic wave to be confined to the surface, the real part of κ_j must be positive. It follows then, from the result in Eq. 1.14, that the real parts of ϵ_1 and ϵ_2 must be of opposite sign. The classic example satisfying this relation is that of a dielectric ($Re[\epsilon_{dielectic}] > 0$) and a metal ($Re[\epsilon_{metal}] < 0$), but these are not the only potential materials that can satisfy this relation. One such example would be that of monolayer graphene, a 2D material with some unique electro-optical properties[21]. It is important to note that while this simple geometry allows for an analytic solution to the plasmonic resonance, Maxwell's equations can fully describe any complex geometry and the resultant behavior. For more complex plasmonic structures, commercial software that can calculate Maxwell's equations self-consistently at various points in space and time can be used to accurately simulate the optical response.

1.3 Graphene

Graphene is a single layer hexagonal lattice of sp^2-bonded carbon atoms, which gives rise to unique optical, mechanical, electronic, and thermal properties which have studied in great detail in recent decades [21]. Graphene was first properly isolated and characterized by Andre Geim and Konstantin Novoselov in 2004 using the "Scotch tape" technique to produce

high quality monolayers of graphene from bulk graphite by peeling them off the surface with tape[22]. Other techniques have since been developed for the creation of monolayer graphene, including Chemical Vapor Deposition (CVD), which can grow large (> 1 cm^2) areas of high quality graphene[23].

In this work, we will be focusing on the optical properties of graphene which are fully encompassed within graphene's band structure and the resultant surface conductivity. The band structure for graphene can be derived from the tight-binding model [21] and at low energies, the band structure is linear and has zero band gap. Due to the lack of a band gap, it is possible for the graphene to be neutral and have a zero energy Fermi level, referred to as the charge neutral point (CNP), where graphene behaves more like a dielectric. However, by adding or removing charge carriers, the graphene will have a net doping (p-doped or n-doped depending on the sign of the charge carrier) and become much more conductive, behaving more like a metal. There are many methods for doping graphene, but a simple method is to create a capacitor with graphene acting as one of the electrodes [24, 25]. By applying a voltage bias between the top and bottom electrodes, charges of opposite sign will build up on the electrodes, doping both materials. For most electrode materials, like metals or doped semi-conductors, the additional charges are insufficient to alter the Fermi level of the material due to the broad valence/conduction bands. The linear band structure of graphene and monolayer structure leads to a situation where relatively few charge carriers are needed to significantly shift the Fermi level. Typical charge carrier densities for graphene range from 0-1 x 10^{13} cm^{-2}, corresponding approximately to 0-0.8 eV. Shifting from 0 eV (CNP) to 0.6 eV has been experimentally achieved with the capacitor set up described above and other techniques can extend this range further[24, 25]. As a result, graphene's electronic properties can be continuously tuned from that of an insulator-like material to a metal, properties which also allow for tuning of the optical properties of graphene.

In addition to the linear band structure, the interaction of graphene with electromagnetic fields can be described with the graphene's optical conductivity (σ_G). This physical quantity can be split into two components, the interband (vertical transitions between the conduction

and valence bands) and the intraband (transitions within the conduction/valence bands).

$$\sigma_G = \sigma_{interband} + \sigma_{intraband} \tag{1.15}$$

Using the methods described in Ref [26], the intraband and interband terms are derived as the following results

$$\sigma_{intraband} = \frac{2ie^2T}{\pi\hbar(\omega + i\Gamma)} ln[2\cosh(\mu/2T)] \tag{1.16}$$

$$\sigma_{interband} = \frac{e^2}{\hbar}[\theta(\omega - 2\mu) - \frac{i}{2\pi} ln\frac{(\omega + 2\mu)^2}{(\omega - 2\mu)^2}] \tag{1.17}$$

where e is the electron charge, T is the temperature, ω is the angular frequency, Γ is the scattering rate, and μ is the chemical potential of the graphene. The interband transitions are Pauli-blocked at energies lower than twice the Fermi level, represented by the step function θ. It is of particular importance to note that graphene's optical surface conductivity depends explicitly on the chemical potential (equivalently the Fermi level for this application) and by changing the Fermi level, σ_G will also change as seen in Figure 1.2a.

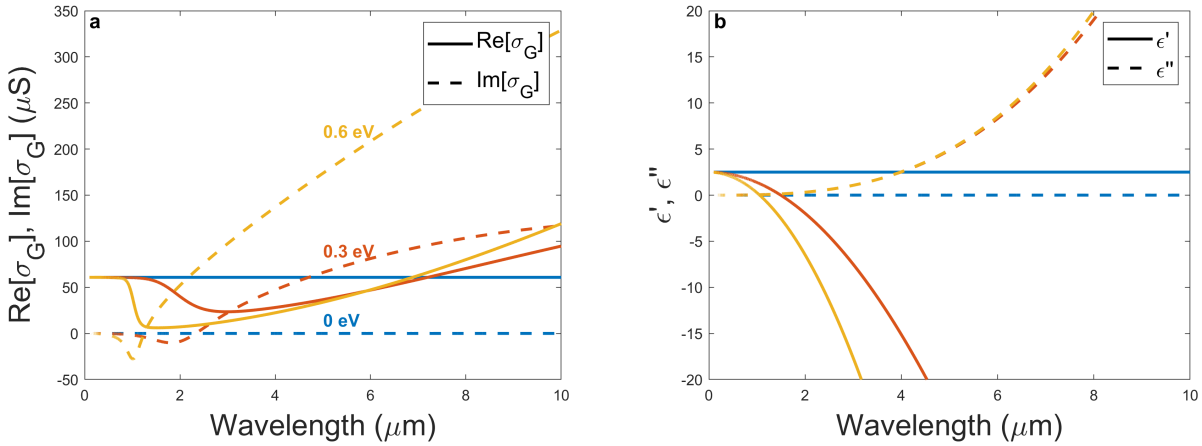

Figure 1.2: Calculated values for the real and imaginary parts of the conductivity of graphene, σ_G, (a) and effective permittivity ϵ (b). for three Fermi levels: 0 eV, 0.3 eV, and 0.6 eV.

It should also be noted that in place of a 2D material with a surface conductivity, graphene can be equivalently modeled as a thin (a single carbon atom thick) material with a permit-

tivity from the following equation

$$\epsilon = 1 + \frac{i\sigma_G}{\delta\omega\epsilon_0} \tag{1.18}$$

where δ is the thickness of graphene (generally modeled as 0.3 nm to mimic the thickness of carbon atoms). This can be a useful metric to understand the optical properties of graphene in context with other materials. Depending on the combination of frequency and Fermi level, graphene's permittivity will behave as either a dielectric or a metal as seen in Figure 1.2b.

With the surface conductivity model of graphene, it is possible to adapt the formalism discussed in the previous section and calculate the plasmonic response of a graphene sheet [21]. The modification will be placing a graphene sheet between the two materials (with the Ansatz that they are both dielectrics) which will be represented as a surface conductivity σ_G at z=0 (see Figure 1.3). The only change to our formalism will be that the boundary conditions at z=0 will read

$$E_{1,x} = E_{2,x}, \tag{1.19}$$

$$B_{1,y} - B_{2,y} = \mu_0 J_x = \mu_0 \sigma_G E_{2,x}, \tag{1.20}$$

where Equation 1.11 is modified due to the presence of graphene at the interface. From these modified boundary conditions, we arrive to a new solution for the plasmonic dispersion relation of graphene, a modification to Equation 1.14.

$$\frac{\epsilon_1}{\kappa_1} + \frac{\epsilon_2}{\kappa_2} + i\frac{\sigma_G(\mu)}{\omega\epsilon_0} = 0 \tag{1.21}$$

where the explicit dependence of σ_G on the chemical potential (or equivalently Fermi level), μ, is noted in the equation. Due to this, it becomes clear that the plasmonic resonance will have a different solution depending on the Fermi level, introducing tunability to the plasmonic resonance.

1.4 Thesis Outline

This thesis will be separated into three parts and represent an exploration of the applications in nanophotonic design from interstellar considerations down to the development of a large-scale, nano-resolution fabrication process to active tuning of thermal radiation.

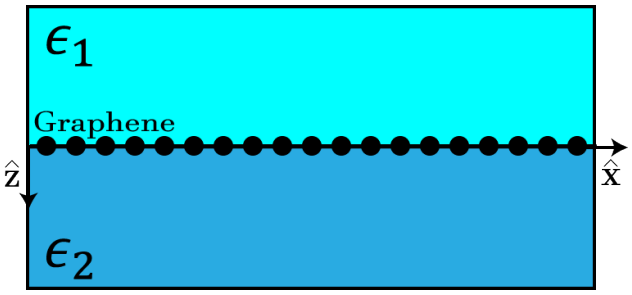

Figure 1.3: Schematic of monolayer graphene at the interface of two dielectrics.

Chapter 2 will be a discussion of the design of a dielectric metasurface based laser-sail that can passively stabilize itself as it is accelerated to one-fifth the speed of light. The motivation of this project is to send probes to our neighboring star system, Alpha Centauri, approximately 5 light years away [27]. Due to these large interstellar distances a new type of spacecraft is required that can accelerate to velocities many orders of magnitude greater than conventional rocketry. This spacecraft will be accelerated by a high power (order GigaWatts) laser beam focused onto the sail. At these high velocities and large distances, it is impossible to actively correct for any abnormalities in the transit of the laser-sail and any corrective actions must be accomplished passively. This section details how the local optical forces can be controlled through the optical properties of the metasurface to provide stabilizing forces for the laser-sail.

Chapter 3 will cover the fabrication, measurement, and modeling of sub 15 nanometer plasmonically active graphene ribbons. To reach these small length-scales, a technique based on self-assembling polymers, block copolymer lithography, was used to pattern the graphene over centimeter length-scales. In this work, it was found that for these narrow ribbons, the characteristic scaling laws for resonant graphene plasmons changed significantly, reducing the optical confinement of light, but also significantly blue shifting the plasmonic resonance wavelength. In addition, this section will discuss a technique to passively align the block copolymers to metastructures, allowing for the creation of large scale active metastructures with nanoscale graphene ribbons.

Chapter 4 will be a discussion of a compact thermal emitter on a chip capable of steering

emited thermal radiation at a continuous range of angles through the tuning of graphene's Fermi level. Thermal radiation is normally incoherent, isotropic, and broadband, but this metamaterial is engineered in such a way that the only emitted thermal radiation is coherent, isotropic and narrowband. The device emits light at only designated frequencies and incorporates an active material (graphene) to change the angle at which the light is emitted. This work demonstrated continuous tuning in the mid-infrared regime over a narrow bandwidth from $\pm 16^o$.

Chapter 2

Self-Stabilizing Laser Sails Based on Optical Metasurfaces

Joel F. Siegel, Anthony Y. Wang, Sergey G. Menabda, Mikhail A. Kats, Min Seok Jang, Victor Watson Brar, "Self-stabilizing laser sails based on optical metasurfaces", *ACS Photonics*, 2019.

DOI: https://doi.org/10.1021/acsphotonics.9b00484[1]

2.1 Introduction

The optical properties of a material can be dramatically altered by structuring the material on sub-wavelength length-scales to create a 'metamaterial' or - for flat geometries - a 'metasurface.' In these systems, the reflection and refraction of the macroscopic light is controlled by engineering the local, microscopic scattering properties. Metasurfaces can be made much thinner than standard optical elements, and recent advances in nano-fabrication as well as optical design tools have allowed for the creation of metasurfaces that generate parabolic lenses, constant-angle beam steerers, vortex beams, and holograms,[7, 12, 13, 28–40] with reflectivities exceeding 99% with low absorptive loss in some cases [41–44]. While the beam-shaping properties of metasurfaces are well known, the optical forces present on metasurfaces have been less explored. To understand these forces, consider Figure 2.1(a), which shows a standard metasurface consisting of resonators that scatter with different phases, reshaping

[1]This section is a reproduction of an already published work found in [1]. The text and figures are unaltered, except for formatting changes.

the wavefronts of reflected and transmitted light. Due to momentum conservation, there are both normal and in-plane optical forces generated across the surface that depend on the scattering behavior. These forces are ordinarily small and inconsequential, however, as the laser power is increased, they can become large enough to impart motion on the metasurface.

One scenario where the optical forces can become large is in 'laser sail' powered spacecraft, where a 100 GW beam is reflected off a mirror-like 'sail', accelerating it to fraction of the speed of light.[45] Among the many challenges facing these efforts is the construction of the sail itself, which must display high reflectivity, minimal absorption, low weight, and be large enough such that the beam can focus on it within solar space. A more strenuous requirement is that the sail and payload exhibit self-stability within the laser beam, such that the sail is passively steered to stay in a position of maximum thrust, and desired directionality. In this article, we show that dielectric metasurfaces provide a promising pathway for realizing a laser sail. We show that by locally controlling the angle and magnitude of reflection/transmission across the sail, metasurfaces can be constructed that enable both efficient propulsion, and a passive means of orientation correction that leads to self-stabilizing behavior when driven by a high-power laser.

This paper is split into two parts. We first conduct an analytical study that considers sails constructed of idealized beam-steering components and, by using dynamical modeling tools, we find deflection profiles that optimize for stability, propulsion efficiency, and operational tolerance. Second, we use finite-difference time-domain (FDTD) simulations to model the light-scattering behavior of actual dielectric metasurfaces that are designed to match the optimized force parameters, and we compare how close realistic metasurfaces can match idealized structures.

We note that there are several requirements of a laser sail that we do not directly address in this work. These include potential bending and folding of the sail, the ability of the sail to be tolerant of relativistic doppler shifting, the possibility of sail overheating, and the ability of the sail to act as an antenna to transmit data back to Earth. Those issues are discussed qualitatively at the end of this manuscript, but a comprehensive resolution is left for future

studies.

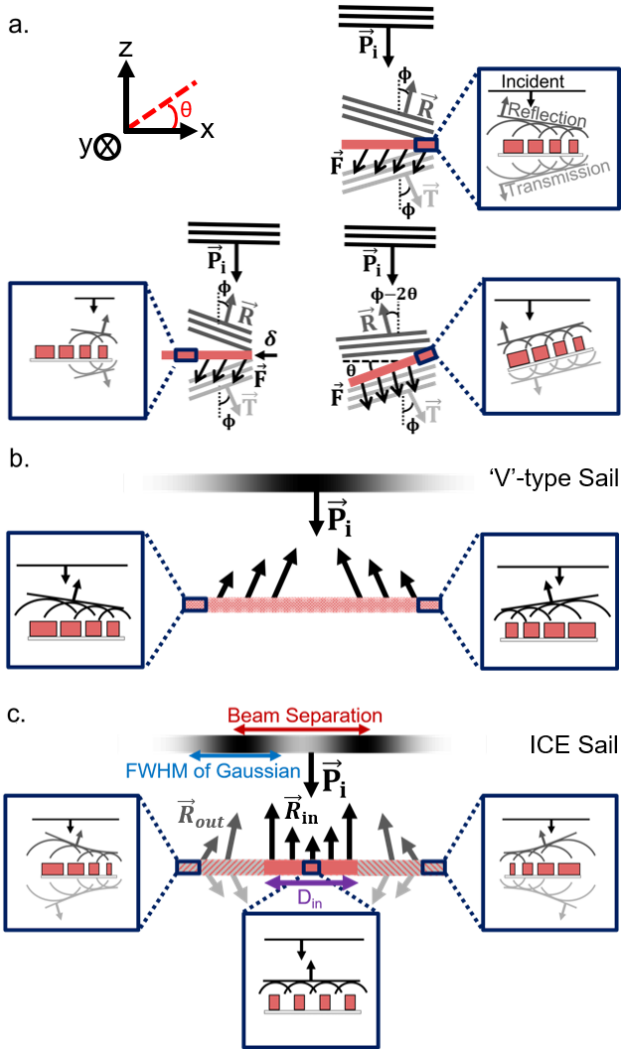

Figure 2.1: (a) Schematic of dielectric metasurface beam-steerer that deflects an incoming beam at a constant angle, ϕ. In black, the resultant forces created by radiation pressure on a beam-steering metasurface that is centered in the beam (upper right), offset by δ (lower left), tilted by an angle θ (lower right). The coordinate system used in this analysis with a rotation in the x-z plane shown in red (upper left). (b) Cartoon schematic of a 'V'-type sail with a Gaussian input beam. (c) Cartoon schematic of an ICE metasurface/sail with a double Gaussian input beam.

2.2 Motion of idealized metasurfaces

2.2.1 Dynamical Force Coefficients

In the simple metasurface beam-steering geometry shown in Figure 2.1(a), the scattered fields from individual optical resonators pick up a linear phase gradient that results in reflected and transmitted wavefronts that are tilted at an angle ϕ with respect to the surface. [5, 6, 46]. If the structure is rotated by an angle θ, the optical path length of reflected light changes linearly across the surface, resulting in an additional -2θ in the angle of the reflected light. The transmitted (refracted) light, meanwhile, maintains the same angle of transmittance as the metasurface is rotated. As the light is reflected/refracted, nonzero tangential (F_x) and normal (F_z) forces are imparted on the structure due to momentum conservation of the combined incoming/outgoing photon and metasurface system. For a generalized metasurface interacting with a non-uniform beam (i.e. Gaussian, flat top, donut, etc..), the local beam power, P_i, as well as the reflected light, $\vec{R}$, and transmitted light, $\vec{T}$, will all be functions of position across the metasurface, and the optical forces will have a non-trivial dependence on the metasurface's rotational or lateral offset relative to the incoming beam. By integrating the optical force and torque contributions across the sail at different relative positions and angles of the sail and drive beam, the first-order equations of motion can be derived as,

$$F = m\frac{\partial^2 \delta}{\partial t^2} = C_1\delta + C_2\theta \tag{2.1}$$

$$\tau = I\frac{\partial^2 \theta}{\partial t^2} = C_3\delta + C_4\theta \tag{2.2}$$

where F and τ are the lateral force and torque acting on the rigid sail, respectively, and δ and θ are the lateral and angular offsets, respectively. $C_{1,2,3,4}$ are the first-order dynamical force coefficients ($\frac{\partial F}{\partial \delta}, \frac{\partial F}{\partial \theta}, \frac{\partial \tau}{\partial \delta}, \frac{\partial \tau}{\partial \theta}$) which are specific for each combination of incident beam and metasurface profile. In this work, we considered metasurfaces that are 4 m wide, with a mass, m, and moment of inertia, I, of 8.5 g and 17 gm^2, respectively. These parameters were extracted from the actual metasurfaces that are described in more detail in the Full-Wave Simulations section. The coefficients $C_{1,2,3,4}$ were derived by calculating the total forces and

torques on the metasurfaces as they are shifted over 2 cm, and tilted by up to 0.1°. We find that the linear approximation can be valid for offsets on the order of tens of centimeters and rotations on the order of degrees, but there is variability between sail and beam combinations.

The dynamical force analysis conducted in our work was restricted to a 2D model of the system where the sail has translational invariance along the y-axis. The motion of the sail is constrained to translations along the x and z axes and rotations in the x-z plane. This approximation is made so that the sails can be faithfully modeled within our computational restraints in the Full-Wave Simulations section. We note that this 2D model does not differ significantly from a full 3D model for three reasons. First, assuming a cylindrically symmetric system in 3D, the dynamic force coefficients for the motion along y and rotation about the x axis are identical to the reversed case. Second, we do not assume the sail is spinning about the z axis, so the two types of motion are uncoupled up to a first-order approximation[47]. Third, while the dynamic force coefficients change when converting from a 2D model to a 3D model of the system, the general trends and approximate magnitudes of the coefficients remain the same (see Supplemental Materials), allowing for conclusions drawn in the 2D case to remain applicable to the 3D situation.

2.2.2 Motion Simulation

Using equations 2.1 and 2.2, we use a 'Leapfrog' integration method [48]–the positions and velocities are updated at interleaved time points, such that they 'leapfrog' over each other–to simulate the motion of a metasurface in a particular beam profile in the presence of beam intensity fluctuations, or with initial lateral and angular offsets of 1 cm or 0.05°. We find that the sail motion can display a large range of behavior depending on the metasurface structure, as well as the drive beam profile, and these behaviors can be described as either 'stable' or 'unstable'. We classify a sail structure and beam combination as 'stable' if, during a 60 second period, the sail does not move or rotate beyond 2 cm or 0.1°, respectively, where the linear approximation is valid. Qualitatively, 'stable' sail behavior is manifested as small oscillations about the origin, while 'unstable' behavior is characterized as the sail quickly

diverging in position and/or angle, as seen in Figure 2.2.

In order to illustrate how metasurface structure can impart stability on a laser sail, consider the sail geometry shown in Figure 2.1(b). This design—referred to as a 'V'-type sail—reflects light at two constant angles that are equal and opposite on the left and right sides of the sail. When the sail moves to the left (right) relative to an incident Gaussian beam, higher power strikes the right (left) side of the sail, and a force is imparted that pushes the sail back to the right (left), thus establishing a lateral restoring force. This sail geometry, however, is not stable against rotational offsets, which force the sail to be pushed out of the beam. An advantage of a metasurface sail, however, is that it can exhibit complex reflection and transmission behaviors without distorting the geometrical shape of the surface or changing the constituent materials; as a result, beneficial force profiles can be generated in realistic structures. As an example, in Figure 2.1(c), we show an 'inverted cat eye' (ICE) type sail that consists of a highly reflective ($R_{in} = 0.95$) inner region that reflects the beam normal to the surface, and a more transmissive outer region (R_{out}) that acts as a 'metalens' with a parabolic reflection/transmission profile. When placed in a 'donut' beam—modeled as two offset Gaussians in 2D—the ICE geometry can correct for both lateral and rotational offsets, as we show below.

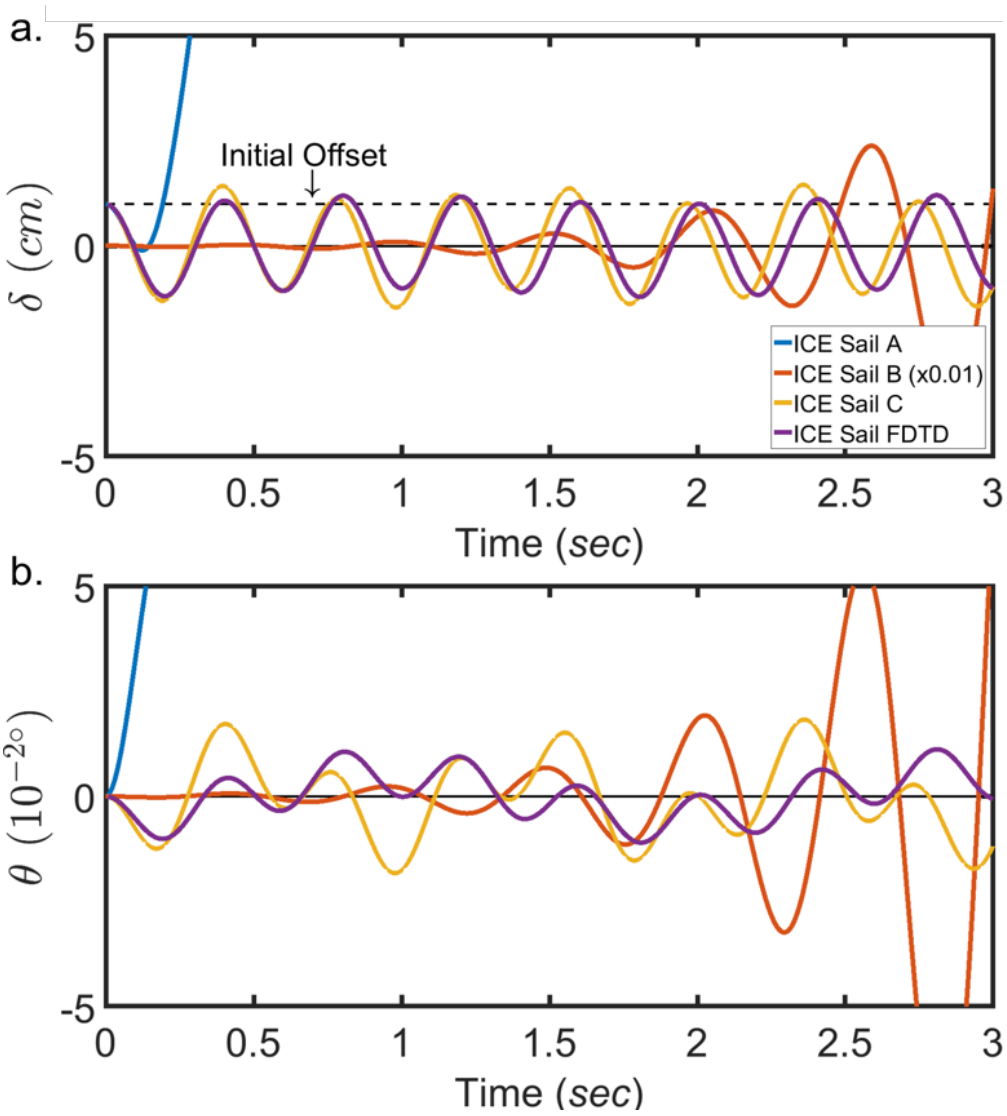

Figure 2.2: Plots of the displacement (a) and rotation (b) for three different sail and beam combinations over a three second time interval. Each sail is four meters wide with an initial offset of 1 cm. The incident beam power is 100 GW. For the three ICE sails, R_{out}=0.3, D_{in} = 2 m, and the incident beam is a double Gaussian with a 1.65 meter FWHM. ICE Sail A is for an incident beam with Beam Separation = 1.8 m, ICE Sail B is for an incident beam with Beam Separation = 2.56 m, and ICE Sail C is for an incident beam with Beam Separation = 2.40 m. ICE Sail FDTD is the motion of an FDTD simulated sail (see the Full-Wave Simulations section for details)

.

Figure 2.2 illustrates the motion of four different ICE sail and beam combinations for the same initial offset of 1 cm. These behaviors can be understood by considering the dynamic force coefficients. ICE sail 'A', shown in Figure 2.2, has $C_1 < 0$, suggesting stability against lateral offsets, but it also has $C_{2,3} > 0$ and $C_4 \sim 0$, indicating that: (1) positive angular rotations create positive lateral forces ($C_2 > 0$); (2) positive lateral offsets create positive torque ($C_3 > 0$); and (3) positive rotations create minimal torque ($C_4 \sim 0$). These conditions create a positive feedback effect between rotation and offset, which acts to quickly destabilize the sail. This can be described quantitatively by considering that $C_1C_4 + C_2C_3 < 0$ is a necessary condition for marginal stability [47], and for $C_4 \ll 1$ this condition cannot be satisfied when $C_{2,3} > 0$.

In contrast, by changing the beam separation of the double Gaussian beam, a *negative* C_3 value can be realized, meaning positive offsets create negative torques, and vice versa. This provides a route towards a stable sail motion where positive rotational offsets drive positive lateral motion ($C_2 > 0$) which, in turn, creates a negative torque ($C_3 < 0$) that corrects for the initial rotation, leading to small oscillations about the origin (Figure 2.2, ICE Sail 'C', yellow line). We note, however, that while the $C_1C_4 + C_2C_3 < 0$ condition is generally satisfied when $C_3 < 0$, this is not a sufficient condition to predict stable sail behavior, which depends on the relative ratios of $C_{1,2,3,4}$ within a narrow range of parameter space. ICE sail 'B', for example, has a *negative* C_3, but it displays an oscillatory motion with increasing magnitude, and does not achieve stability.

2.2.3 Metasurface Stability Optimization

In order to search for and classify stable ICE sail configurations, we simulated the motion of 4 meter wide sails with varying reflection coefficients for the outer region (R_{out} $= 0.15, 0.3$), inner region widths ($D_{in} = 1.33\ m,\ 2\ m$), and outer edge deflection angle ($\theta_{max} = 5.7°, 11.4°$ and $22.6°$) (an expanded analysis is shown in the Supplementary Materials). We model the motion of these sails in a continuum of double-Gaussian beam profiles with an incident beam composed of two Gaussian beams symmetrically offset from the cen-

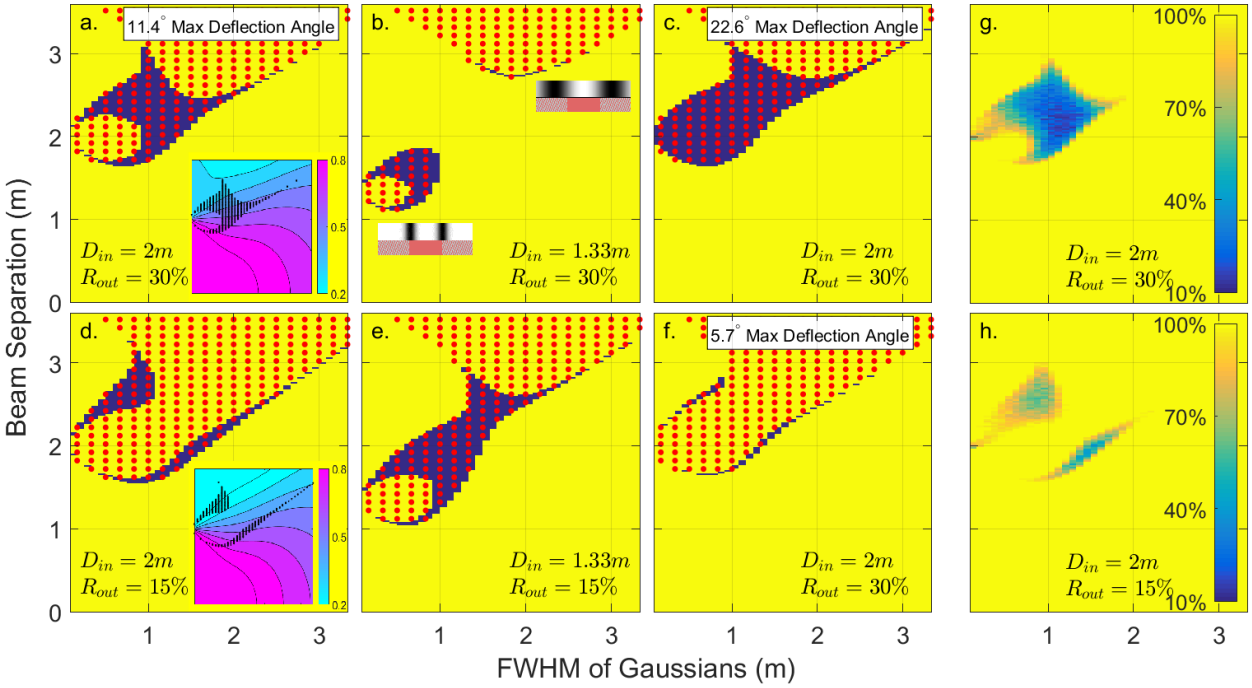

Figure 2.3: (a-f) Analysis of stability for 6 ICE-sail configurations driven by double-Gaussian beams with varying beam separation and FWHM for an initial offset of 1 cm, 50% of the maximum allowable offset for stability. Yellow (purple) regions indicate sails configurations that are unstable (stable). The dotted red areas indicate sail configurations that satisfy the $C_1C_4 + C_2C_3 < 0$ condition. (a,b), are ICE sails R_{out} = 0.3 and D_{in} = 2 m, 1.33 m, respectively. Insets in (a,d) show the fraction of maximum thrust achievable for each sail/beam combination and the dotted black areas indicate sails that were stable when initially offset by 1 cm. Insets in (b) show a cartoon of the beams on the sail in those regions. (d,e) are ICE sails with R_{out} = 0.15 and D_{in} = 2 m, 1.33 m, respectively. (c,f) are ICE sails with D_{in} = 2 m and R_{out} = 0.3 (similar to a), but their angle of deflection at each point is halved or or doubled in comparison to (a), respectively. The motion was simulated over a 60 second period. (g,h) Analysis of stability for two ICE-sail configurations both with D_{in}=2 m or R_{out}=30% (g) and R_{out}=15% (h) reflection efficiencies for their outer regions. The motion of the sail is tracked over 5 minutes with 0.12% noise introduced to the beam. Yellow regions indicate sails that failed 100% of the time. Blue indicates regions that maintained the lowest rates of failure.

ter, with the beam defined by the FWHM of the Gaussians, and the separation between them. The results of these simulations are shown in Figure 2.3.

These results demonstrate that stability is strongly dependent on the metasurface profile, as well as the beam shape. Overall, as R_{out} decreases and D_{in} increases, the number of regions that satisfy $C_1C_4 + C_2C_3 < 0$ increases, a result that occurs because these sails can achieve negative values of C_3 for more beam combinations. The number of configurations that show actually stable sail behavior, however, does not show a strong, intuitive dependence on R_{out} or D_{in}. There is, however, a stronger dependence on the outer edge deflection angle. Figures 2.3 (a), (c), and (f) compare the stability behaviors of a sails that have identical R_{out} and D_{in} values, but with different outer edge deflection angles. These figures indicate that steeper deflection angles (or, equivalently, parabolic lens profiles with shorter focusing distances) allow for more stability conditions, and loosen constraints on the drive laser.

In order to determine which sail/beam configurations are 'maximally stable', it is necessary to consider beam intensity profiles that contain time dependent distortions which, in real world scenarios, could be caused by laser interference ('speckle') and atmospheric fluctuations, which can destabilize the sail. Here we analyze the sensitivity of metasurface sails to such perturbations by using a Monte Carlo method to introduce randomized, time-varying intensity fluctuations in the beam profile while simulating the motion of the sail. We assume intensity variations that occur over 10 cm characteristic lengthscales, with time correlations of 1 ms, corresponding to timescales associated with atmospheric turbulence [49]. With the fluctuation intensity set to 0.12%, we ran 100 simulations for each configuration show in Figure 2.3 (a) and (d) and we recorded the probability that a sail maintained stability. The result of those simulations are shown in Figure 2.3 (g) and (h), where we observe a large variation in stability rates between sail configurations. When R_{out} =0.3 (g), the stable region forms a large basin of stability that achieve a failure rate of as low as 13%. If we decrease R_{out} to 0.15 (h), we increase our minimum failure rate to 40%.

These simulations also provide insight for deducing which stable configuration provide maximum thrust, which is plotted in the insets of Figure 2.3 (a) and (d). Considering only

beams that have a FWHM > 1.6 m (i.e. realistic, diffraction-limited beams) , the maximum thrust achievable with a stable sail/beam configuration is 370 N and 400 N for $R_{out} = 0.3$ and 0.15, respectively. For comparison, the maximum theoretical thrust—which occurs when 100% of the light is reflected normally, is 667 N.

2.3 Full-Wave Simulations

In the Motion of Idealized Metasurfaces section, we modeled the behavior of theoretical beam-steering metasurfaces with idealized optical properties. Actual dielectric metasurfaces, however, rely on using dielectric nanostructure arrays designed to control the optical wavefronts of the scattered laser fields, and these structures diverge from ideal behavior due to phase slips in the structure, phase-dependent reflectivity/transmissivity, and interactions between nano-resonators. These effects lead to sub-optimal efficiencies, and can potentially create large modifications in the dynamical force coefficients of a metasurface laser sail. In this section, we design and model large-scale ICE metasurfaces and we extract the optical forces on those structures as they are tilted and offset in a drive beam. We then compare the dynamical force coefficients of an actual dielectric surface to those of an idealized structure, and show that the self-stability behavior described in the Motion of Idealized Metasurfaces section is achievable in real-world structures.

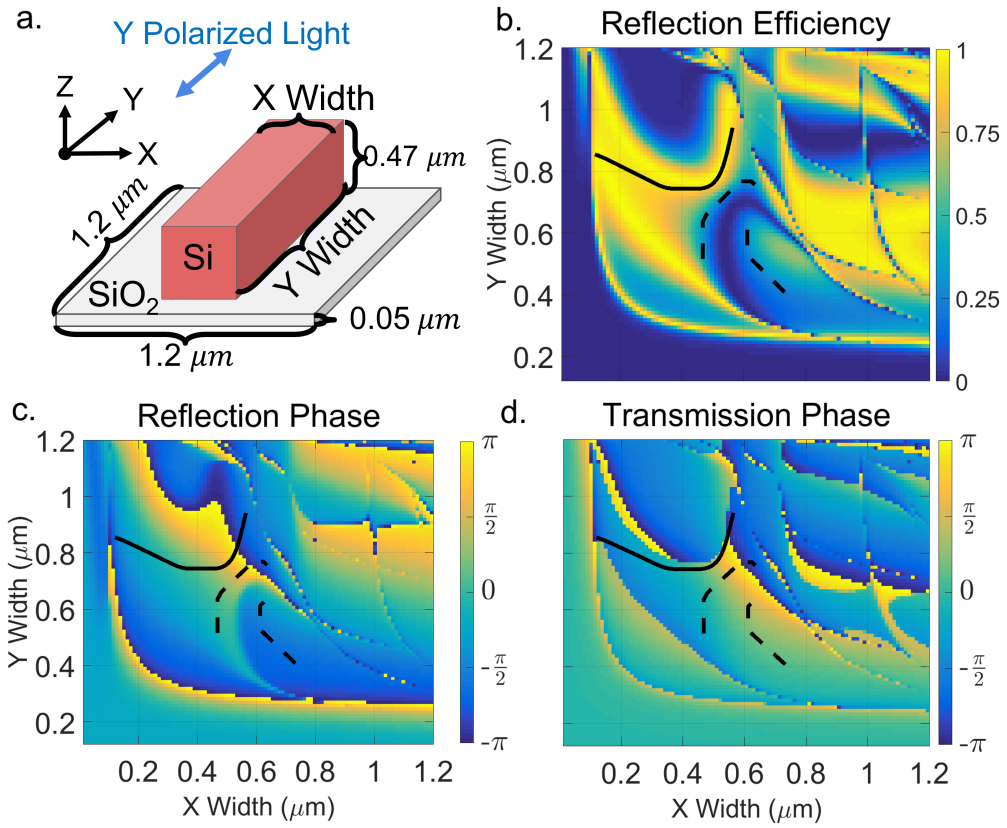

Figure 2.4: Diagram of the unit cell, reflected magnitude/phase, and transmission phase. (a) Metasurface unit cell consisting of a rectangular block of Si on a SiO_2 surface. The boundary conditions in the X and Y direction are periodic. (b) Magnitude of reflected light as the X and Y dimensions of the Si block vary. (c) Phase of reflected light as the X and Y dimensions of the Si block vary. (d) Phase of transmitted light as the X and Y dimensions of the Si block vary. The solid (dashed) lines indicate a 95% (30%) reflectivity path covering 2π phase.

2.3.1 Optical Design

In order to achieve full control of optical wavefronts, it is necessary to engineer a set of dielectric resonators that can scatter light with phase shifts ranging from 0 to 2π, and with arbitrarily small or large reflection/transmission efficiencies. Here we use Si nanoresonators on SiO_2, which have previously been shown to be effective in the construction of metasurfaces with high reflectivity [41, 42] as well as metasurfaces that act as efficient focusing optics. In order to minimize atmospheric losses and absorptive heating losses within the sail, we assume a drive beam wavelength of 1.55 μm. The set of resonators we use in this work are shown in Figure 2.4(a); 470-nm-high Si blocks with variable length and width are placed on a 50-nm-thick SiO_2 substrate, and the spacing between resonators (center to center) is maintained at a constant 1.2 μm. The scattering properties of these resonators (and all future metasurfaces described in this work) are calculated using commercial finite-difference time domain tools (Lumerical FDTD). As the resonator dimensions are varied, the magnitude and phase of the reflected/transmitted fields also change, as shown in Figure 2.4(b-d). Contours of constant reflectivity that cover 2π phase can be selected from these plots. Two examples are shown in Figure 2.4 as solid and dashed lines for 95% and 30% reflectivities, respectively. Note that for 95% reflectivity a single continuous path can be chosen, while for 30% reflectivity, two separate paths are required for full phase coverage. Similar contour selection can be performed for reflectivities ranging from 95-15%.

The sets of resonators described above can be used to construct metasurfaces as outlined in the Introduction and Motion of Idealized Metasurfaces sections, where the magnitude and direction of the reflected/transmitted wavefront is locally controlled by placing resonators with the desired scattering profiles at each location on the surface. This is demonstrated in Figure 2.5 where we have plotted the electric field profile of the scattered waves from one side of an ICE sail constructed using the nanoresonators in Figure 2.4. For this metasurface and all others studied below, periodicity is assumed along the y-dimension. The structure has a total width is 504 μm containing 420 individual resonators with constant period of

1.2 μm. The input beam is a 'double Gaussian' beam, with a FWHM of 82.9 μm and an annular diameter of 334 μm. The resonators placed from 0 to 125 microns were chosen from the dashed black paths in Figure 2.4 and provide 30% reflection, along with a parabolic beam-steering profile that ranges from 5.7° at the edge of the sail to 2.8° at the boundary between the outer and inner regions. The inner region is formed by 95% reflective resonators that all have the same phase, which is chosen to match the phase of the innermost resonators of the outer 30% reflective region. Details of how the resonators are chosen at each position are provided in the Supplemental Materials.

2.3.2 Optical Forces

In order to exhibit the self-stabilized behavior described in the Motion of Idealized Metasurfaces section, it is necessary to design metasurface sails that faithfully generate particular dynamical force coefficients, and that are free from perturbations that could lead to localized folding. Here, we calculate the optical forces locally by by integrating the Maxwell Stress Tensor (MST) around boxes enclosing individual resonators or small groups of resonators. We then sum the vector components of those local forces to calculate the overall lateral and normal forces, as well as the torque on the sail as it is tilted and displaced within the beam. In Figure 2.5 (b,c) we plot an example of these force components for a metasurface ICE sail illuminated by a double Gaussian beam. These forces display the following expected general trends: (1) there is a lateral force on the outer region that stretches the sail and scales with steering angle and beam intensity; (2) there is no lateral force on the center region, which is designed to be strictly normally reflecting; (3) there is a normal force across the sail that scales with beam intensity and sail reflectivity. In this example, we have integrated the MST over a bounding box that groups resonators between phase slips in the metasurface, such that each x,z force shown in Figure 2.5(b,c) is determined by calculating the net optical force on groups of 5-10 resonators, depending on the local steering angle. This is done to decrease calculation time, and it has a negligible effect on the net torque or force on the sail, which was confirmed by comparing to calculations where the MST was integrating over individual

resonators.

When forces are analyzed on individual resonators, it is observed that there are discontinuities in the force profile that occur due to phase slips and interactions between pairs of resonators, which can cause to actual scattering phase to diverge from the predicted phase. Those effects—which cause anomalies in the scattered E-field profile visible in Figure 2.5(a)—are discussed more in the Supplementary Materials. In most cases those local discontinuities create forces that are several orders weaker than the elastic restoring forces in the underlying SiO_2 slab. However, even when averaged over several resonators, the effects of phase shifts due to resonator interactions can be observable. For example, the depression in lateral forces for the resonators located at $\sim$78 μm in Figure 2.5(b) is due to such interactions. Moreover, the lateral force reverses sign at the end of the sail due to diffraction from the sail edge, and from the altered scattering properties of the last resonator, which is in an asymmetric environment. For small steering angles, these effects have a minor contribution to the overall forces on the sail, however, as beam steering angles are increased so is the frequency of phase slips, which leads to larger contributions to the overall lateral force. Methods for potentially ameliorating and/or accommodating for such effects are discussed in the 'Conclusions' section.

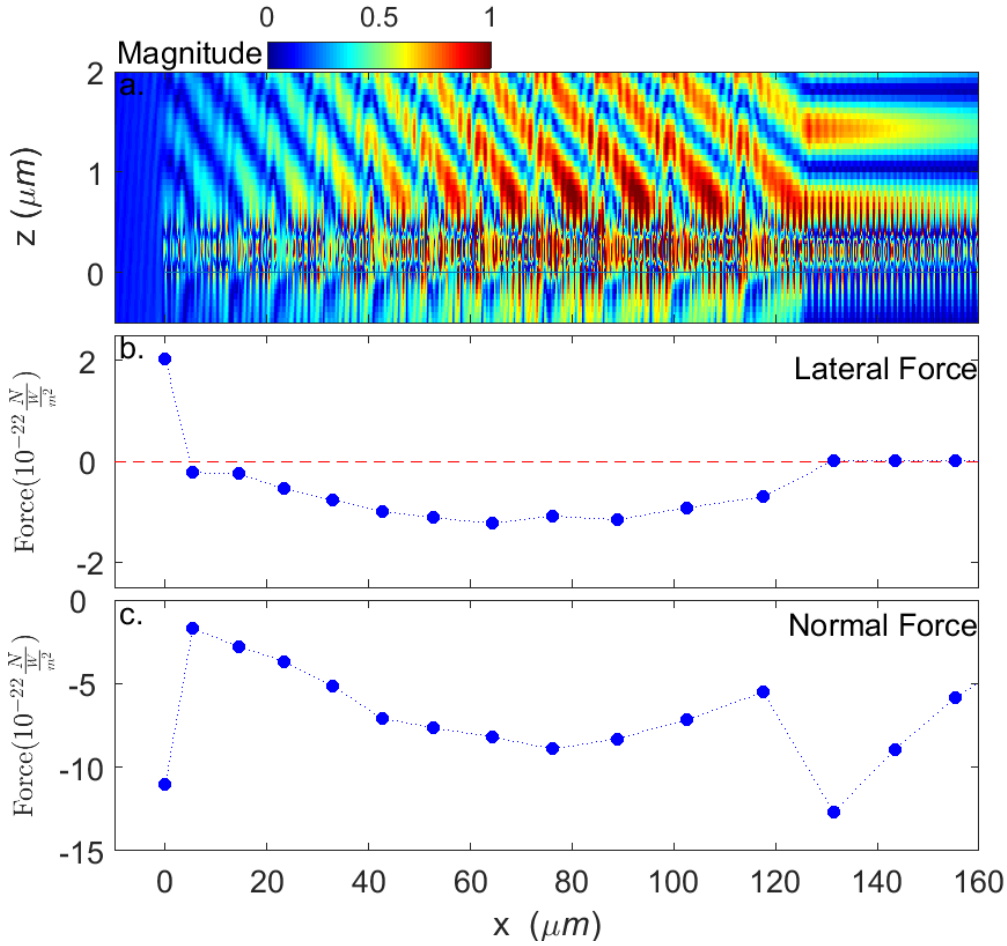

Figure 2.5: (a) Electric Field Profile of half of a ICE sail with a reflective (95% reflectivity) inner radius of 127 μm and an outer transmissive (30% reflectivity) region with a parabolic scattering profile where the inner edge steers at 2.8° and the outer edge steers at 5.7°. (b,c) The local lateral and normal components of the optical forces on the sail, calculated by integrating the Maxwell stress tensor (MST) over a surface that encloses local groups of resonators. For the outer region the bounding surfaces contain resonator groups that are between phase slips which ranges from five resonators for the outer edge, 10 resonators inner edge. For the inner, reflective region, the bounding surfaces contains 10 resonators each. The force is normalized using an input beam power of 1 Watt across the sail.

In order to extract the dynamical force coefficient from our simulations, it is necessary to calculate the local optical forces as the metaurface sail is shifted and tilted within the beam, and then perform linear fits to the position/tilt vs. force/torque dependencies. Figure 2.6 shows the numerically simulated local forces for offsets of 0 μm and 40 μm and, separately, rotations of 0° and 3°, for the ICE sail shown in Figure 2.5. In these plots, we include analytical calculations (lines) of local optical forces for a sail made of ideal beamsteering components, which show good agreement with the forces extracted from the FDTD simulated metasurfaces. Shifted simulations were performed over lateral and rotational steps of 5-10 μm and 0.5-1°, respectively, and we found that the force/torque showed a linear dependence on offset/rotation angle over ranges of 20-40 μm and 1-3°. First-order fits were used to determine the effective dynamical force coefficients, $C_{1,2,3,4}$, which are shown in 2.1. We find that the coefficients from an actual dielectric metasurface are of the same sign and order-of-magnitude as those calculated analytically, but can vary by as much as 40%. These differences can be attributed to the aforementioned phase slips and inter-resonator interactions which add distortions to the reflected/transmitted phase fronts of the scattered light, and can also lead changes in the overall reflection coefficients.

ICE Sail	C_1 ($\frac{N}{Wm}$)	C_2 ($\frac{N}{Wdeg}$)	C_3 ($\frac{N}{W}$)	C_4 ($\frac{Nm}{Wdeg}$)
Ideal	-1.43E-6	6.06E-11	-2.23E-10	1.03E-15
Full-wave	-1.79E-6	4.13E-11	-2.23E-10	3.00E-15
Full-wave Scaled	-2.29E-10	4.13E-11	-2.23E-10	2.36E-11

Table 2.1: Dynamic Force Coefficients of an ICE Sail. The Full-Wave dynamic force coefficients scaled up to a 4 meter wide sail are shown as well.

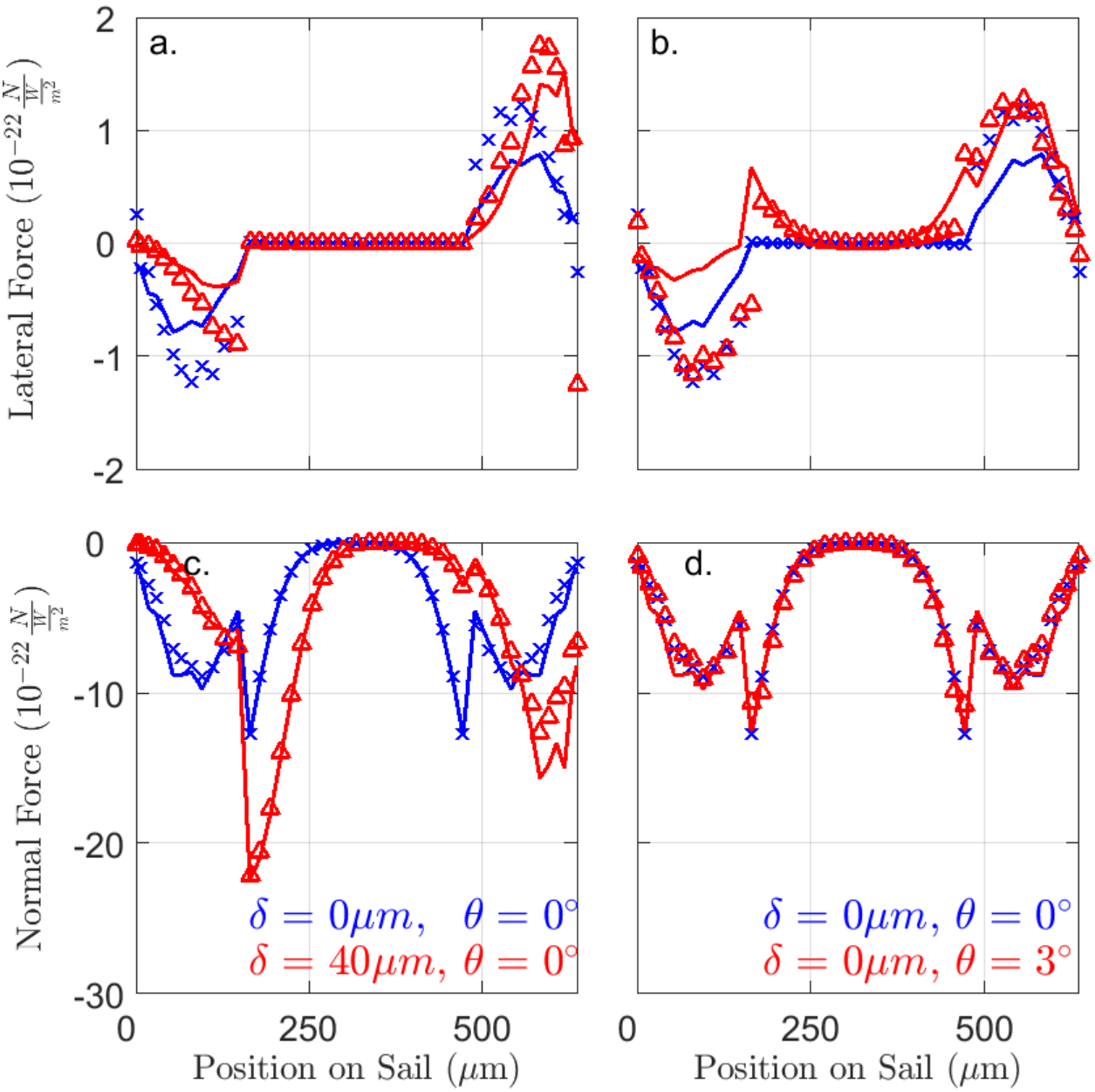

Figure 2.6: The local lateral (x) and normal (z) components of the optical forces on the entire sail shown in Figure 2.5, calculated from the Full-Wave simulations (blue xs and red triangles) or calculated using the methods described in the Motion of Idealized Metasurfaces section (solid blue/red lines). (a) corresponds to the force in the x direction when the sail is offset. (b) corresponds to the force in the x direction when the sail is rotated. (c) correspond to the force in the z direction when the sail is offset. (d) corresponds to the force in the z direction when the sail is rotated. In all plots, the un-offset, unshifted force is shown for comparison in blue and the offset or rotated force is shown in red.

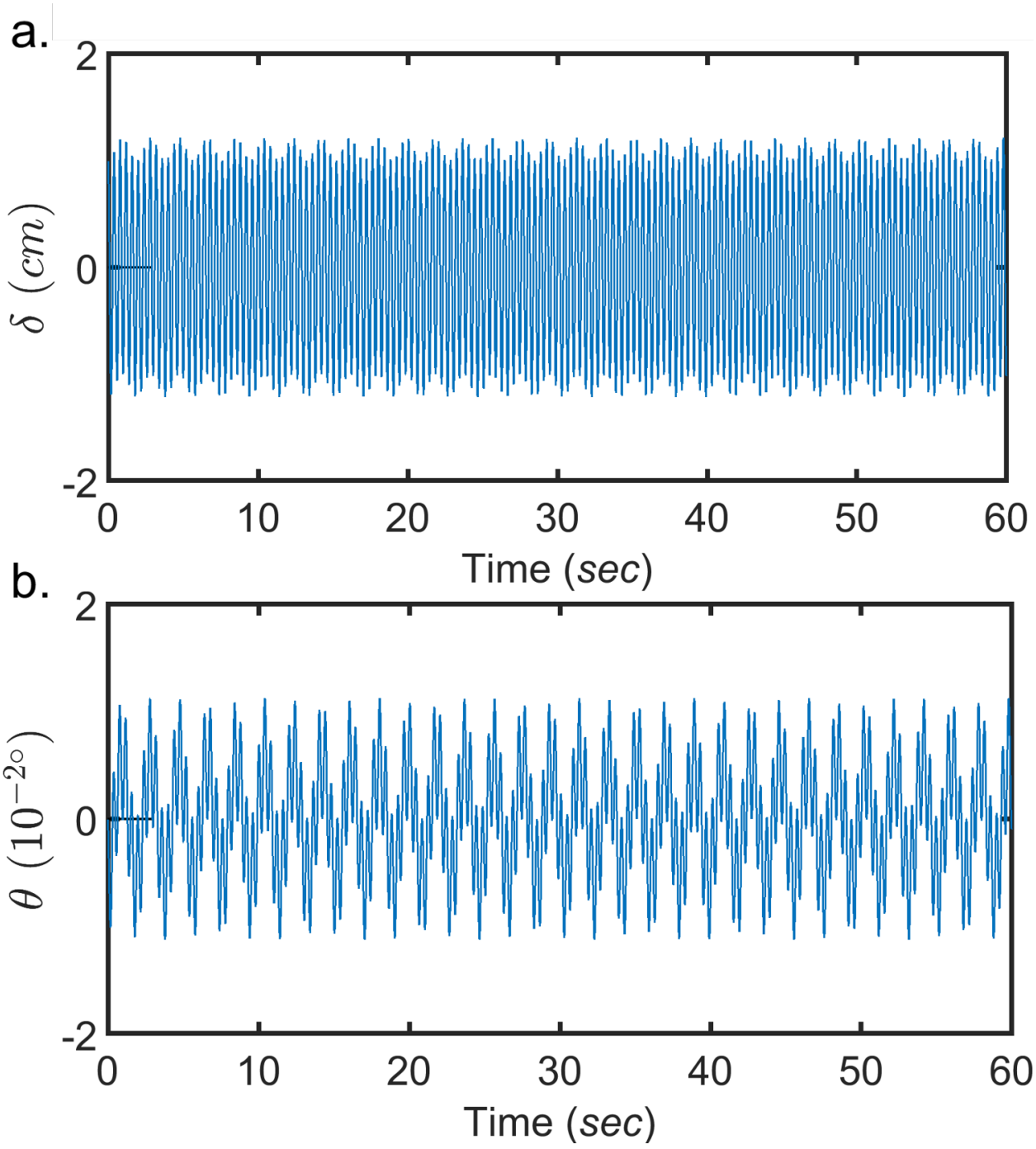

Figure 2.7: Motion (a) and rotation (b) of an FDTD simulated sail with an initial offset of 1 cm for 60 seconds.

The overall stability of the ICE metasurface sail can be tested by using the dynamical force coefficients in Table 2.1, along with the methods described in the Motion of Idealized Metasurfaces section. However, in order to test the viability of a 4 meter metasurface, these coefficients must be scaled accordingly as the beam size (annulus and FWHM of individual Gaussians) and sail size are increased by $\sim$8000$\times$. Such scaling has no effect on C_2 or C_3, but C_1 will scale inversely with size, while C_4 will scale linearly with size. This behavior was confirmed by calculating $C_{1,2,3,4}$ analytically for 504 μm and 4 m ICE sails with equivalent ratios for reflective/transmissive regions, and equivalent steering angles. An analysis of these scaling laws is provided in the Supplementary Materials. The resulting scaled dynamical coefficients for a 4 meter ICE metasurface sail are given in the bottom row of Table 2.1 and, using these values, we can model the motion of a sail with an initial lateral offset of 0.01 cm, which is shown in Figure 2.7. These results show that a metasurface sail constructed from Si nanoresonators can exhibit self-stability within a drive beam for over 300 seconds, without ever leaving the range where the linear approximation is valid and exhibiting behavior that closely resembles the motion of the idealized structures discussed in the Motion of Idealized Metasurfaces section.

2.4 Discussion

The combined results of the Motion of Idealized Metasurfaces and the Full-Wave Simulations sections show that dielectric metasurfaces offer a viable pathway for creating laser sails that maintain directionality and stability within high-power laser beams. In order to comprehend the real world speed that such a metasurface sail may achieve, we can consider a 100 GW drive laser constructed from a 100km diameter ground-based array of projectors. Operating at wavelength of 1.55 μm and for distances up of up to 10$\hat{8}$ km, such a beam can maintain features with a FWHM of 1.67 m, which—in an assumed annular geometry—would generate a thrust of $\sim$360 N and allow for self-stable behavior for the sail modeled in Figure 2.7. The weight of such a sail is $\sim$8.5 g, and if we assume a 5 g payload, these conditions would allow for final velocities of 0.21c to be achieved in $\sim$50 minutes, after which the craft travels too

far to project a laser shape that yields stability[50]. In addition to self-stability and a high achievable velocity, we note that the ICE sails discussed in this work contains an outer region that can be utilized as a parabolic collimator with a 4 meter aperture, that could potentially be used to transmit a signal.

While these results are promising, the analysis presented in this work makes several assumptions and simplifications, and ultimately the design of a metasurface laser sail will require new breakthroughs in metasurface architectures, more powerful simulation tools, and the development of new constituent materials. The key issues we would like to address are as follows:

Folding, strain, and local forces - Throughout this work, we have assumed that the metasurface sail maintains a rigid flat shape, regardless of local force gradients. In a real world situation, however, a 50 nm thick SiO_2 substrate will easily bend and fold over both macroscopic and microscopic lengthscales. Those perturbations will alter the optical performance of the metasurface, and second-generation designs must incorporate mitigation strategies for such effects. The primary cause of microscopic strain—which occurs between 2-10 nanoresonators—is interactions between resonators, which alters their scattering properties such that the beamfronts and optical forces are distorted. Those effects can be compensated for by using inverse design and optimization methods that consider such interactions and adjust resonator shape accordingly. Such methods should not only allow for the creation of metasurfaces with smoother force profiles, but they could also enable higher scattering angles, which increases the lateral forces. More problematic is the macroscopic strain, which occurs due to non-uniform beam intensity and changes in the metasurface reflectivity. Figure 2.5 (c), for example, shows that the normal forces on the sail is not constant, which will lead to bowing of the sail. In order to correct for those effects, it is necessary to design a sail with a favorable relationships between structure and light scattering such that, for example, outwardly bowed surfaces reflect light less. Alternatively, metasurface sails that exhibit stability within flat beam profiles would suffer less from such effects, or metasurface elements that pull outwardly on the sail can be incorporated. We note that the ICE sail

design contains some elements of this latter concept, with the edges of the sail scattering at steeper angles and generating larger lateral forces which pull the sail taught. The strain issue can also be addressed by exploring new materials systems. While Si membranes fabricated from SOI display compressive strain, SiN membranes have intrinsic tensile strain, and—when fabricated into photonic crystal geometries—have been recently shown to have reflectivities >90% for 56 nm membrane thicknesses, making them a promising candidate material system[51]. Finally, we note that abnormal optical forces are easily generated on the rim of the sail, where edge diffraction can drive large distortion in the scattered beam fronts. Those effects must be compensated for by designing metasurface edges that minimize diffraction, or by using drive beams that have negligible intensity on the edge of the sail.

Doppler shift - The metasurfaces discussed in the Full-Wave Simulations section are designed to work at a single fixed wavelength (1.55 μm), while relativistic light propulsions requires a reflectors that works across a range of Doppler shifted frequencies. Achieving velocities up to $0.21c$, for example, requires a metasurface that exhibits effective propulsion and self-stability from 1.55 - 1.99 μm. Typically, the scattering phase of an individual nanoresonator is dependent on wavelength and that dependence can lead to distorted beamfronts, and local optical forces that disturb self-stabilizing motion. However, we note that the design of broadband, achromatic metasurfaces that shape light equally across many wavelengths is an active area of research with several recent successes [30, 52, 53], and those methods can be equally applied to the metasurface laser sail problem.

Absorptive Heating - In this work, we have assumed that the high-power laser imparts optical forces on the metasurface sail, without heating. In fact, some fraction of the light will be absorbed by the sail due to intrinsic properties of the constituent materials and defects, and that absorption will increase the sail temperature. A final, steady state temperature is reached when the power absorbed at the laser wavelengths is equal to the thermal power radiated over all wavelengths. An accurate estimate of this final temperature requires full-angle simulations over all wavelength, using precise values of the temperature-dependent extinction coefficients of Si and SiO_2, which is left for future work. However, by using

published room temperature values for Si and SiO_2 [54–58], we can estimate a wavelength-integrated emissivity of 0.05, and an absorptivity at 1.55 μm near 10^{-5}, yielding a final temperature of $\sim$2200 K–outside the range of the melting points of Si (1687 K) and SiO_2 (1983 K). This temperature can be systematically decreased by engineering the structure to have higher emissivities or lower absorption by changing the constituent materials, or by layering and/or shaping the material stack. For example, it has been shown that the inclusion of mid-IR resonators can enhance the emissivity of metals and polar materials [59–61], and that thin, structured material films can display novel thermal emission properties [16, 62]. Using these methods to increase the emissivity to 0.5, for example, would result in a steady state temperature of $\sim$1200 K.

Residual motion - The force models used in the Motion of Idealized Metasurfaces section were first-order, and did not include damping terms, which lead to oscillatory sail motion that did not decay in magnitude. In order to achieve true stability, however, it is necessary to discover conditions where the amplitude of oscillation is reduced to zero, which prevents lateral motion or rotations that would persist after the drive laser is turned off, and would misdirect the spacecraft. Optical damping terms could potentially be included through Doppler effects, however, such methods would require relativistic lateral motion, and unrealistic fabrication parameters. More promising is to incorporate some hysteretic motion in the sail whereby, for example, some bending in the sail leads to changes in the optical scattering that is dependent on the velocity. Such stabilization methods are used in other mechanical systems [63], and they are an attractive option for laser sail applications, where no obvious damping method exists.

In conclusion, we have studied the use of dielectric metasurfaces to act as laser sails for relativistic, interstellar spacecraft. We have shown that the ability of metasurfaces to reshape optical beamfronts can also be used to control local optical forces, and for extremely high-power lasers those forces can impart an optical trapping-like effect on the metasurface. That effect is potentially useful for stabilizing laser sails and we find a large parameter space that such behavior is expected to occur. These results represent a new area of metasur-

face research that will benefit greatly from recent advances in metasurface design, and also introduces new challenges for the nanophotonics community.

Chapter 3

Large Scale Fabrication of Graphene Nanostructures

3.1 Using Bottom-Up Lithography and Optical Nonlocality to Create Short-Wave Infrared Plasmonic Resonances in Graphene

Joel. F. Siegel, Jonathan H. Dwyer, Anjali Suresh, Nathaniel S. Safron, Margaret A. Fortman, Chenghao Wan, Jonathan W. Choi, Wei Wei, Vivek Saraswat, Wyatt Behn, Mikhail A. Kats, Michael S. Arnold, Padma Gopalan, and Victor W. Brar, "Using Bottom-Up Lithography and Optical Nonlocality to Create Short-Wave Infrared Plasmonic Resonances in Graphene", *ACS Photonics*, 2021.

DOI:https://doi.org/10.1021/acsphotonics.1c00149[1]

3.1.1 Introduction

Optoelectronic devices based on tunable graphene plasmonic resonances offer a promising route toward next-generation devices[64–66] that include chemical sensors,[67–69] perfect absorbers,[20, 70] photodetectors,[71–74] tunable filters,[75] and high-speed intensity and phase modulators[76, 77]. Many of these devices require the patterning of graphene sheets into nanoribbons,[20, 24, 68, 69, 76, 78] nanoperforated sheets,[67, 79, 80] or nanodisks[75, 79] that support plasmonic oscillations with a resonant frequency set by the characteristic

[1]This section is a reproduction of an already published work found in [25]. The text and figures are unaltered, except for formatting changes.

length of the nanostructure and the carrier density of the graphene[24, 79, 80]. Thus far, these devices have operated at mid- and far-infrared wavelengths. There have been both theoretical[81]and experimental[82, 83] investigations that have indicated the plasmonic response of graphene should be heavily damped at free-space wavelengths shorter than 6 μm due to plasmon–phonon interactions. Nevertheless, graphene plasmonic resonances at wavelengths as short as 3.5 μm have been experimentally observed[24] and, at present, it is not clear if there is a high frequency cutoff for graphene plasmons and, if so, what sets that limit. If the resonant plasmonic response of graphene could be pushed to shorter wavelengths and into the short-wave infrared (SWIR), there would be substantial fundamental and technological implications. For example, theoretical models predict, and experiments demonstrate, that graphene plasmons could create extremely high Purcell-enhanced rates of emission[24, 84, 85] and could even be used to drive optically forbidden transitions[86]. These processes are expected to become more dramatic in the SWIR and, unlike the mid-infrared, there are numerous fluorescent SWIR emitters–including quantum dots,[87, 88] lanthanide ions,[89] and III–V materials[90]–that can be used as a platform to observe these effects. Meanwhile, from a technological perspective, a tunable SWIR plasmonic response would allow for the creation of high-speed, low-cost devices that operate at telecommunication wavelengths. To date, however, no experiments have demonstrated a resonant plasmonic response in graphene in the SWIR, largely due to the unique plasmonic dispersion relation in graphene, which leads to a very large mismatch between the plasmonic (λ_p) and free-space wavelengths (λ_0)[66]. For the mid-infrared (MIR), this mismatch, or confinement factor (λ_0/λ_p), is typically around 50-100. Therefore, to achieve a plasmonic resonance at $\lambda_0 = 5$ μm, graphene nanostructures with 30 nm length scales are needed (the nanostructure width approximately defines $\lambda_p/2$)[24]. In the SWIR, however, the confinement factor has been predicted to increase to 100–200,[81] such that achieving resonance at $\lambda_0 = 2$ μm would require patterning the graphene to feature sizes of 8 nm. Creating periodic patterns with these length scales over large (>100 μm^2) areas is difficult for top-down lithography methods such as electron beam lithography (EBL)–which was previously used to create plasmonic resonators down to 15

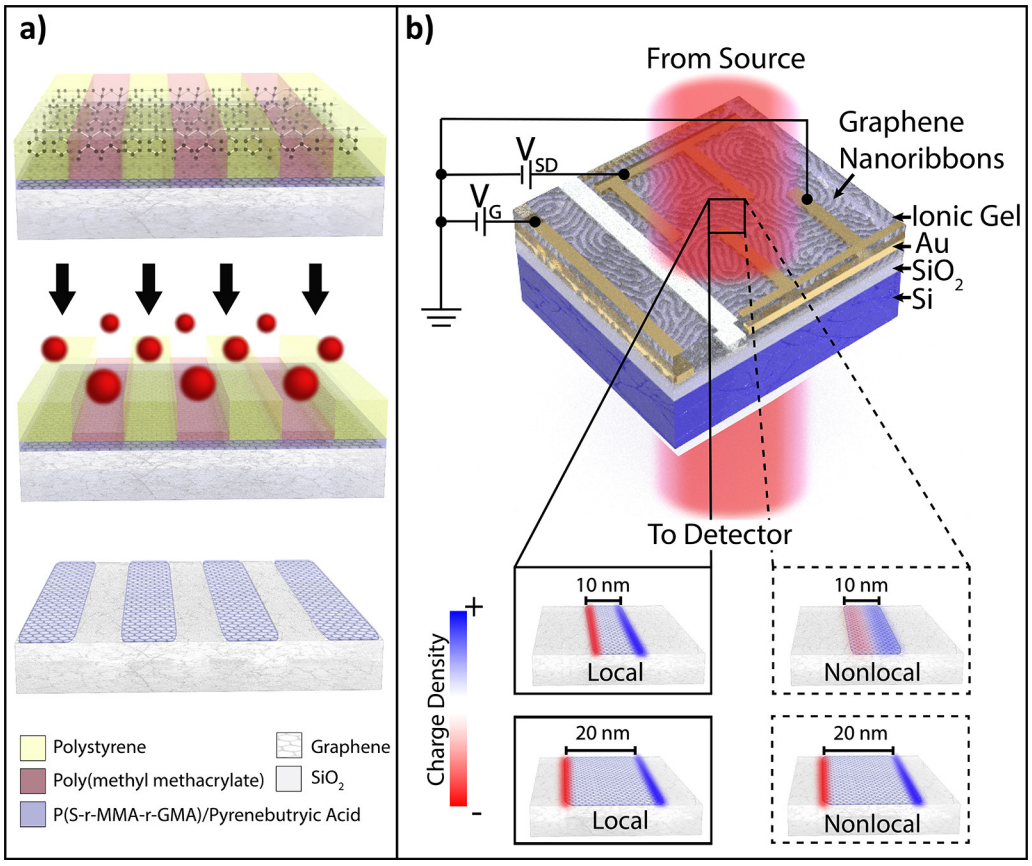

Figure 3.1: . (a) Overview of the block copolymer (BCP) procedure for fabricating graphene nanoribbons (GNRs), illustrating (top) the sample after BCP deposition, (middle) during RIE etch, and (bottom) after BCP removal. (b) Schematic of experimental device with gold finger contacts and an ionic gel gate placed atop the GNR "zen-garden" (shown as an embedded SEM image). The circuit illustrates the electrical setup where a gate voltage (V_G) is applied between the separated areas of graphene and the resistance across the graphene is measured by applying a source/drain bias (V_{SD}) across the active area. Insets in (b) illustrate the exaggerated charge density distribution of graphene plasmonic resonances for local and nonlocal, for widths of ribbons 10 and 20 nm

nm[24]–due to proximity effect distortions. Thus, to explore the SWIR regime, new lithographic methods must be developed that are capable of creating graphene nanostructures at sub-15 nm length scales over centimeter-scale areas. A promising alternative to EBL is block copolymer (BCP) lithography, a bottom-up method that creates etch masks with dense nanoscale features over waferscale areas. BCP lithography has been shown to be effective at patterning graphene into nanostructures, including graphene nanoribbons (GNR)[91, 92] and nanoperforated graphene (NPG)[67, 93, 94].

In this paper, we show that graphene nanostructures fabricated using BCP lithography down to 12 nm length scales can act as resonant plasmonic cavities with tunable resonant free-space wavelengths down to 2.2 μm, substantially shorter than the previous record of 3.5 μm[24]. Additionally, the confinement factors of our devices reach approximately 137, matching the highest experimentally demonstrated value of an optical cavity in a 2D material[24, 95]. Our ability to create resonators well into the SWIR is aided by a larger-than expected blue-shift in the measured resonant frequency of our smallest resonators in comparison to what is predicted by a local electrodynamic model. We attribute this blue-shift to both nonlocal and electron-quantization effects in the GNRs,[96–98] which alter the characteristic scaling laws of plasmonic resonances in sub-15 nm graphene structures.

3.1.2 Results

Graphene Nanostructre Fabrication

We fabricated resonant graphene plasmonic devices using a BCP lithographic process outlined in Figure 3.1a, where a self-assembled pattern in a BCP film acts as an etch mask for creating graphene nanostructures. Graphene's surface, however, is not energetically favorable for thin film assembly, making it incompatible with standard BCP techniques (see SI[2], section S1). Two previous approaches to overcoming this challenge involve preassembling the BCP film on a sacrificial substrate and the transferring the preassembled film onto graphene[99], or depositing BCP on a wetting layer of a thin oxide[93] or poly(dopamine)[100] layer on

[2]SI can be found at https://pubs.acs.org/doi/10.1021/acsphotonics.1c00149?goto=supporting-info

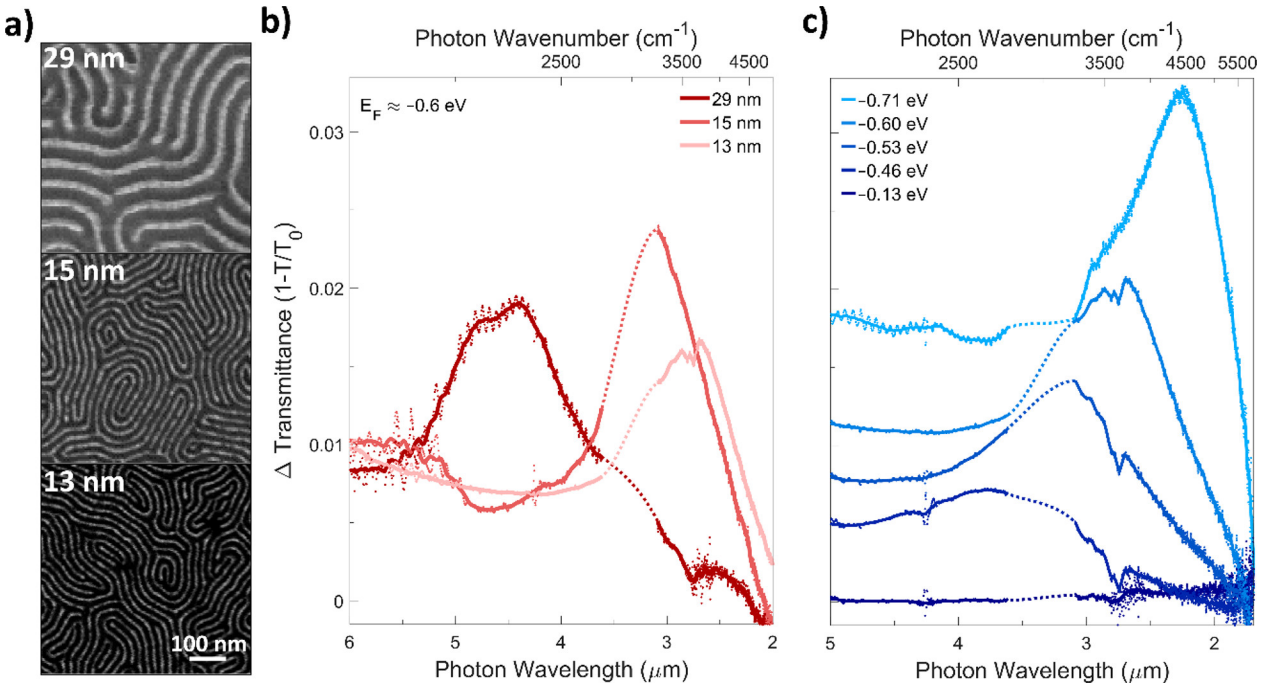

Figure 3.2: (a) Schematic of graphene nanoribbons (GNRs) and SEM images containing GNRs with 29 ± 3, 15 ± 2, and 13 ± 2 nm widths. (b) Differential transmittance through GNRs at a fixed doping level of approximately 0.6 eV normalized to transmittance at the charge neutral point (CNP). (c) Differential transmittance through 13 ± 2 nm wide GNRs as a function of doping level, normalized to transmittance at the CNP. Dashed colored lines indicate regions where the signal strength was small due to absorption in the ionic gel.

the graphene. While functional, these methods lead to either significant film loss during the transfer process or an oxide layer on the graphene that can perturb the optical properties. We developed a new approach by using a molecular monolayer of pyrene butyric acid (PBA) to alter the surface energy of the graphene (see SI, section S1). This approach leads to large patterned areas with minimal (<2 nm) residue on the patterned graphene surface (see SI, sections S2 and S3), enabling the optical properties of the graphene nanostructures to be unaffected by adventitious surface phonons.

Using this new PBA-based BCP methodology, we fabricated GNRs from CVD-grown graphene[101] on a 525 μm Si wafer with 285 nm of thermal oxide. The GNRs were etched in a "zen-garden" pattern with widths ranging from 29 ± 3 nm down to 12 ± 2 nm, as measured using both scanning electron microscopy (SEM) and atomic force microscopy (AFM, see Figure 3.2a and SI, section S2). The shape and size of the polymer microdomains (and

the resultant ribbon dimensions) can be controlled by the molecular weights and relative volume fractions of each block[102, 103]. The minimum ribbon width of 12 nm represents the thermodynamic limit of self-assembly for the BCP used in this study, poly(styrene-b-methyl methacrylate), but smaller features are theoretically achievable using more complex BCP compositions[102, 104]. In addition to GNRs, we also applied our technique to fabricate nanoperforated graphene, which exhibited optical properties similar to the GNRs (see SI, section S4).

After GNR fabrication, EBL was used to create gold-finger electrical contacts to the sample, and an ionic gel was used to vary the carrier density of the GNRs,[105]as shown in Figure 3.1b[3]. As-prepared, CVD graphene sheets were hole-doped due to the iron chloride transfer process, with the background Fermi level (EF) ranging from 0.4–0.5 eV (see SI, section S6)[106]. The ionic gel gate allowed E_F to be varied continuously from 0–0.74 eV on ribbons as small as 13 nm[107]. Measurements were also performed using an electrostatic backgate rather than the ionic gel, including on 12 nm GNRs. Those measurements produced results similar to the ionic gel gate data, however, the E_F could only be varied from 0–0.59 eV, giving a less dynamic range (see SI, section S5). The Fermi level in these experiments was determined through measurements of the interband-transition spectrum of the sample (see SI, section S6)[108]. The width and doping-dependent infrared transmission spectra of the GNRs were obtained using a Fourier transform infrared (FTIR) spectroscopy microscope. Doping-dependent transmittance spectra for each sample were normalized to spectra obtained at a Fermi level of 0 eV, the charge neutral point, taken from the same area of the sample.

[3]Ionic gel was prepared as discussed in Ref. [25], the origin of this text. To prepare the GNRs, a plastic tweezer was rubbed along the ribbons to remove sections to isolate areas, a necessity for the top gate to have electronically isolated regions. Once the gel was prepared, 2-3 drops of the ionic gel were dropped onto the surface of a fully wired up sample, coating it in a thin liquid film. The sample was then placed in the transfer chamber of a glove-box where it was pumped on for 5 minutes to evaporate. The final result is a thin, clear film over the surface of the sample. To gate the GNRs, a voltage bias was applied between the two separated areas of GNRs. In this work, there would be two independent sets of "finger" contacts with the GNRs between them removed via the aforementioned scrapping. Voltage range was +/- 3 V (CNP was around + 0.5-1V).

3.1.3 Optical Properties of BCP-Fabricated Graphene Nanoresonators

Infrared spectroscopy measurements of BCP-fabricated GNR devices revealed sharp absorption peaks associated with plasmonic resonances in the GNRs. Figure 3.2b shows the width-dependent spectra of plasmonic resonances in the GNRs for a constant Fermi level of ∼0.6 eV. The wavelength of these resonances shows a distinct blue-shift as the width of GNR dimensions are systematically decreased, which is consistent with previously reported plasmonic resonances in graphene nanostructures[24, 69, 80]. Variance in the GNR width, as determined by SEM images, is measured to be approximately 2-3 nm, which creates a large fractional change in the width of the smallest features. This effect leads to substantial inhomogeneous broadening in plasmonic resonances for smaller GNRs. Other sources of inhomogeneous broadening may include regions with poor electronic contact and uneven background doping.

Next, we measured the carrier-density dependence of these samples, as shown in Figure 3.2c for a representative sample with 13 nm wide GNRs. These measurements show that increased doping leads to a blue-shift in the plasmonic resonant frequency and an increase in the intensity of the spectral features. For the largest achievable doping levels, the resonant energies of the GNRs were observed to occur at SWIR frequencies, well beyond the mid-infrared energies that have been observed in previous experiments. The highest resonant energies that we observed were for 13 nm GNRs with E_F = –0.73 eV, where the resonance frequency was tuned to 4500 cm^{-1} (2.2 μm).

The plasmonic resonances we observe display doping- and width-dependencies that, for large GNR widths, are qualitatively similar to theoretical predictions and experimental measurements[24, 84]. However, for narrow (<15 nm) widths, we observe behavior that deviates from theoretical expectations. These behaviors can be observed in Figure **??**a, where we plot the resonant frequencies of three representative GNR devices as a function of width for different Fermi levels. For comparison, we also plot the theoretical width-dependent resonant frequencies simulated using a first-order random phase approximation (RPA) model for the

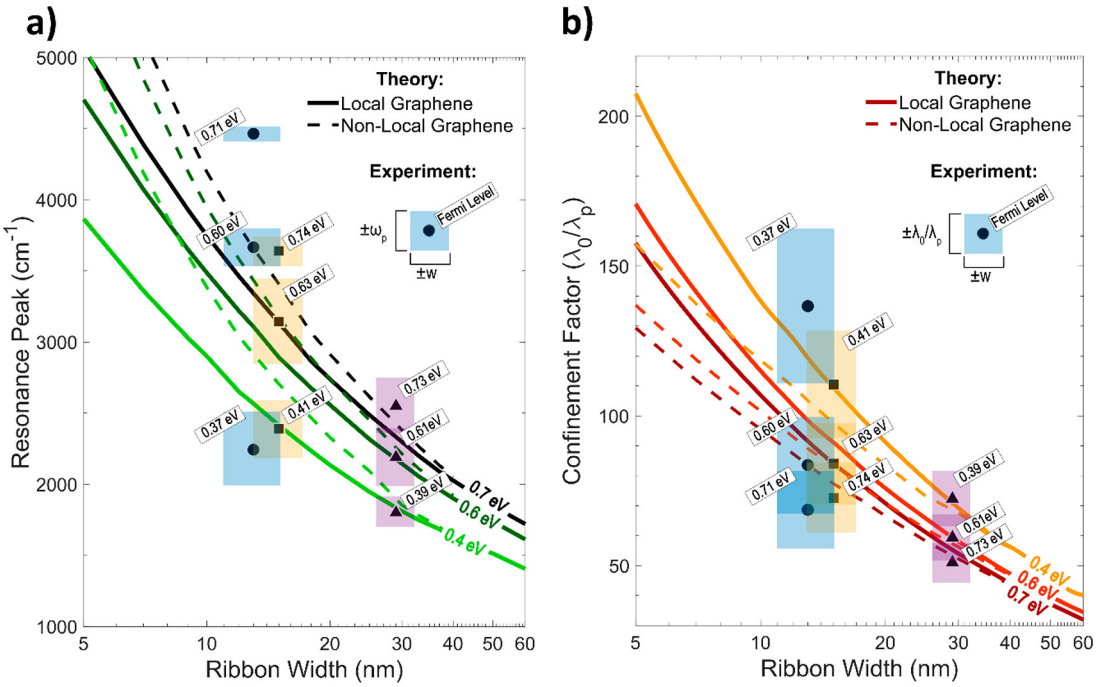

Figure 3.3: (a) Theoretical dispersion (lines) of GNR plasmons as a function of ribbon width for various Fermi levels with experimental measurements (symbols) of the resonance energy at specific ribbon widths and Fermi levels. (b) Theoretical (lines) and experimental (symbols) confinement factors of resonant graphene plasmons in GNRs of varying width, plotted for different Fermi energies denoted on the graph. For both (a) and (b), solid lines indicate the local approximation model of graphene, while dashed lines include a nonlocal term. The experimental points are the same measurements across both plots.

conductivity of graphene[109] and a finite-difference time-domain solver (solid lines). For the widest resonators (purple triangles) there is good agreement between our experiment and theoretical predictions, namely, that the resonances occur at the expected Fermi levels given our uncertainties. However, our measurements reveal that, when the GNR width is decreased below 15 nm, the plasmonic resonances are blue-shifted from first order RPA-based calculations[109]. For example, Figure **??**a shows that 13 nm wide GNRs with an E_F of 0.71 eV display a resonance near 4500 cm^{-1}, while first-order RPA predicts the resonance to occur near 3600 cm^{-1}, an offset of more than 20%. In order to match the theoretical curves of the first-order RPA model, the widths of the GNRs would need to be nearly half the widths measured using SEM (see SI, section S2), or the carrier density would need to be at least 30% more than what we estimate based on the experimentally measured interband

transition cutoff (see SI, section S6). Both scenarios are unlikely based on our experimental uncertainty.

We can further analyze the properties of these plasmonic modes by calculating their confinement factors, the ratio of the free-space wavelength to the plasmon wavelength. ($\lambda_0/lambda_p$). We extracted the plasmonic wavelength through our simulations, where the plasmonic resonators behave as Fabry–Perot oscillators with a nontrivial edge scattering phase[24]. The resulting confinement factors are shown in Figure 3.3b for different ribbon widths and doping levels. We found that our smallest ribbons, 13 nm wide GNRs, featured confinement factors as large as 137 ± 25. This value is 25% higher than what has previously been achieved in 20 nm wide GNRs,[24] and within a margin of error of the largest observed confinement factor in an optical cavity of a 2D material, which was demonstrated using vertically confined acoustic graphene plasmons[95].

3.1.4 Discussion

Our results reveal that the behavior of graphene plasmons strongly deviates from first-order optical models at SWIR frequencies, and that this deviation manifests as a blue-shift in the characteristic frequency of graphene plasmonic resonances. We believe that the large blue-shifts that we observe in narrow GNRs are not due to potential experimental errors, but rather can be understood as nonlocal and electron-quantization effects perturbing the graphene plasmons,[96–98, 110] as described below.

Optical nonlocality describes the effect of an electric field in one location producing a polarization in the nearby vicinity. Such perturbations are known to occur most strongly in regions of high optical field enhancement, as in metallic nanostructures with small (¡10 nm) geometric features[111, 112]. These effects can be described mathematically as a modification to Ohm's Law, by connecting the in-plane currents J and electric fields E as follows: $J = \sigma(\omega)E - -\frac{\beta^2}{\omega^2}\nabla(\nabla)$, where $\sigma(\omega)$ is the conductivity of graphene and the β^2 term accounts for the pressure of an inhomogeneous electron fluid, representing the approximation of the nonlocal effects in a semiclassical approach[96]. In order to determine the magnitude of

the shift of the plasmonic resonances in our GNR devices due to nonlocality, we included this modification to Ohm's law to our finite element Maxwell equation solver (COMSOL) simulations of the GNRs[96, 112]. The plasmonic behavior was modeled by electromagnetic waves scattering off the GNRs, which created resonances in the transmission spectra. The results of those calculations (shown in Figure 3.3a,b as dashed lines) indicate that nonlocal effects blue-shift the resonant plasmon energies in GNRs and that this effect is more dramatic as the ribbon width is decreased and for lower doping levels. For example, for 29 nm GNRs at $E_F = 0.73$ eV, nonlocal effects shift the resonant frequency by 2%, while for 13 nm wide GNRs at $E_F = 0.71$ eV, the resonant frequency is shifted by 12%. While these corrections bring the theoretical predictions closer to the 20% shift we observed in our experiment, they do not fully account for the total blue-shift.

A second possible contribution we consider is electron quantization in the GNRs, where the continuum model for graphene quasiparticles breaks down, forming low-energy band gaps and exotic edge states that depend on the exact edge termination of the GNRs[113–118]. Such effects become stronger for more narrow GNRs, and calculations from ref [98] indicate that quantum effects should blue-shift the plasmonic resonance of 13 nm wide GNRs by approximately 5%[97, 98]. The prospectof electron quantization occurring in these devices is supported by transport measurements performed on similarly prepared NPG samples with characteristic widths of 18 $\pm$ 2 nm[93]. Those measurements revealed an effective electronic bandgap of 100 meV, which could strongly perturb the infrared graphene dielectric properties and drive changes in the resonant plasmonic response.

The combined effects of optical nonlocality and electron quantization, evaluated independently, account for the majority of the experimentally observed blue shifts in our measurements, but they do not completely describe the offsets that we observe. The remaining discrepancies could potentially be due to GNRs that have effective widths that are slightly thinner than what we observed in SEM/AFM measurements caused by, for example, damaged graphene edges due to RIE undercutting (see SI, section S2). We also note that a complete theoretical model should consider both optical nonlocality and electron quantiza-

tion effects concurrently and should include additional effects such as band renormalization and Landau damping[119]. Such a model is beyond the scope of this work and left to future investigation.

The blue-shift in the resonance frequency that we observe has broad implications for the limits of future optoelectronic devices based on graphene plasmons. Most importantly, our results reveal that graphene nanostructures can exhibit a strong, tunable optical response in the SWIR. Moreover, the length scales needed to realize such behavior are larger than previously predicted and directly accessible to BCP lithography. For example, our first-order RPA calculations indicated that to show plasmonic activity at telecommunication frequencies (1.55 μm), GNR widths of 4.5 nm at a carrier density of 1 eV would be necessary, requiring significant advances in large-scale fabrication techniques. However, because nonlocal and quantum perturbations increase in magnitude as GNR width is decreased, it may be possible to reach telecommunication frequencies in GNRs with widths of 7–10 nm, requiring only modest improvements over the fabrication methods described in this work. Another important consequence of the blue-shift that we observe is that the confinement factors of graphene plasmons with short wavelengths are smaller than previously predicted, as illustrated in Figure 3.3b[81]. This decrease in confinement indicates that several predicted phenomena that leverage graphene plasmondriven light–matter interactions, including SPASing,[120] enhanced spontaneous emission of forbidden transitions,[86] and enhanced sensing,[68] may occur at lower rates than previously anticipated. For example, 13 nm GNRs were previously calculated[81] to exhibit a confinement factor of $\sim$120 with an E_F of 0.64 eV in comparison to the 84 $\pm$ 13 confinement factor we observed in this work for an E_F of 0.63 eV. Since two plasmon spontaneous emission rates scale as (λ_0/λ_p)[69, 86] our results indicate emitters coupled to such GNRs will undergo two-plasmon spontaneous emission at a rate 1 order of magnitude lower than previously thought.

3.1.5 Conclusion

In conclusion, we developed a fabrication technique based on block copolymer (BCP) lithog-

raphy that allowed us to probe new regimes of graphene plasmonics and enabled the first measurement of resonant graphene plasmons in the short wavelength infrared (SWIR). Our results provide direct evidence that scaling laws of graphene plasmons change at sub-15 nm length scales. These changes correlate with the modeled predictions of both nonlocal and electron quantization effects. Consequently, reaching the SWIR wavelengths, and even shorter, can be achieved in larger structures than previously thought, facilitating a new avenue of research for graphene-based devices. The graphene nanostructures we fabricated also exhibit, to the best of our knowledge, among the largest lateral confinement factors as 2D optical cavities in the literature[95, 121–124]. However, these results demonstrate that confinement is actually smaller than previously predicted,[81] limiting the anticipated ability of graphene to enhance light– matter interactions. Our findings show that graphene plasmonic devices created using BCP lithography represent an exciting platform to expand the tunable working range of graphene plasmonics, enhance light–matter interactions, explore quantum effects, and create new types of graphene devices.

3.2 Graphioepitaxy

A limitation for the graphene nanostructure fabricated via the BCP technique is their poor coupling to free-space light. As seen in Figures 3.2b,c, the majority of the light does not interact with the graphene ribbons. By incorporating the graphene ribbons into metastructures, it has been theoretically and experimentally demonstrated the efficiency can be greatly enhanced and the graphene ribbons can be utilized to tune the optical behavior [19, 20]. These hybrid structures require precise patterning of the graphene as well as the metastructure. That level of precision cannot be accomplished by the surface neutralization technique which does not produce any long range ordering as seen in Figure 3.4a. Order can be enforced on the self-assembly process by topographically patterning the substrate, a technique referred to as graphoepitaxy. In graphoepitaxy, bars with an affinity for one of the composite polymer blocks are deposited on the substrate and the preferential block will maintain contact with the side-wall, inducing alignment as seen in Figure 3.4b[125, 126].

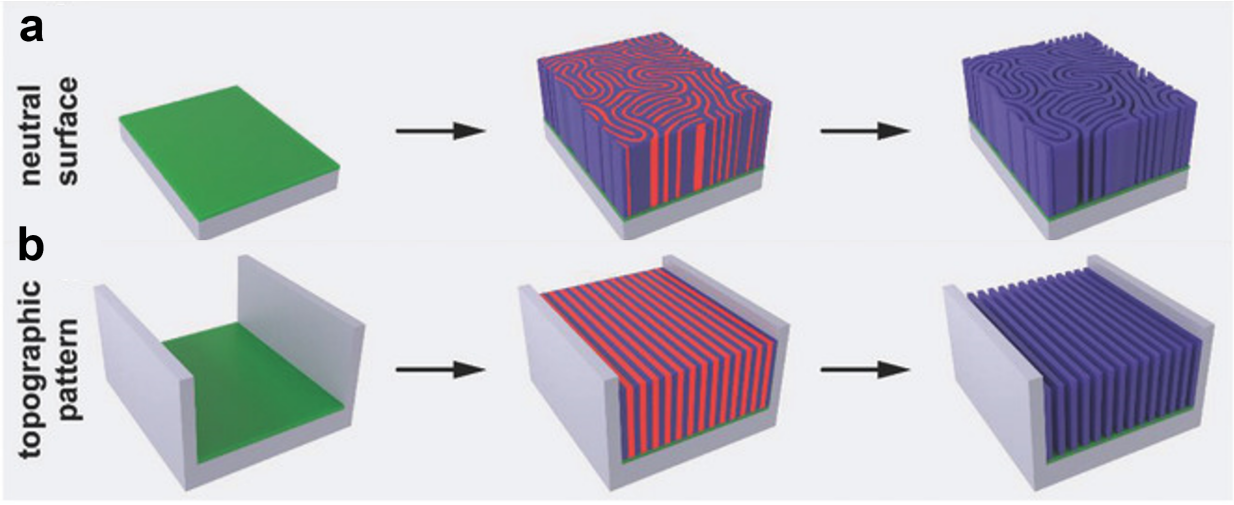

Figure 3.4: (a). BCP self-assembly on neutralized substrate with uncorrelated ordering. (b). Topographic patterning of the neutralized substrate with side-walls preferential to one block (blue polymer), inducing order[125].

3.2.1 Graphioepitaxy metamaterial

The topographic structure can serve dual purposes, it can be used to order the BCP *and* it can serve as a metasurface. Graphioepitaxy imparts some constraints on the topographic structure, and therefore the metasurface designs. The gap width must fit an integer multiple of the BCPs so that the BCP has the appropriate space to align and the structure height should be greater than the BCP length so that the BCP stays within the gap. As a proof of concept, we propose a mid infrared thermal tuner based on a hybrid graphene-metasurface that will be fabricated via graphioepitaxy self-assembly. The device consists of a dielectric (either SiN or Al_2O_3 were considered) with a gold backreflector, gold/silicon bars with 30 nanometer wide GNRs in the gaps. It should be noted that the silicon on top of the bars assists in promoting the self-assembly (graphioepitaxial alignment was only successful in our work with the gold/silicon bars), but does not contribute to the optical response of the designs considered. Though this does not preclude other possible designs where the silicon does contribute. A schematic of the device can be seen in Figure 3.5. Due to time constraints, we were only able to demonstrate successful graphioepitaxy alignment of the anticipated structure on a SiO_2/Si substrate (see Figure 3.5b).

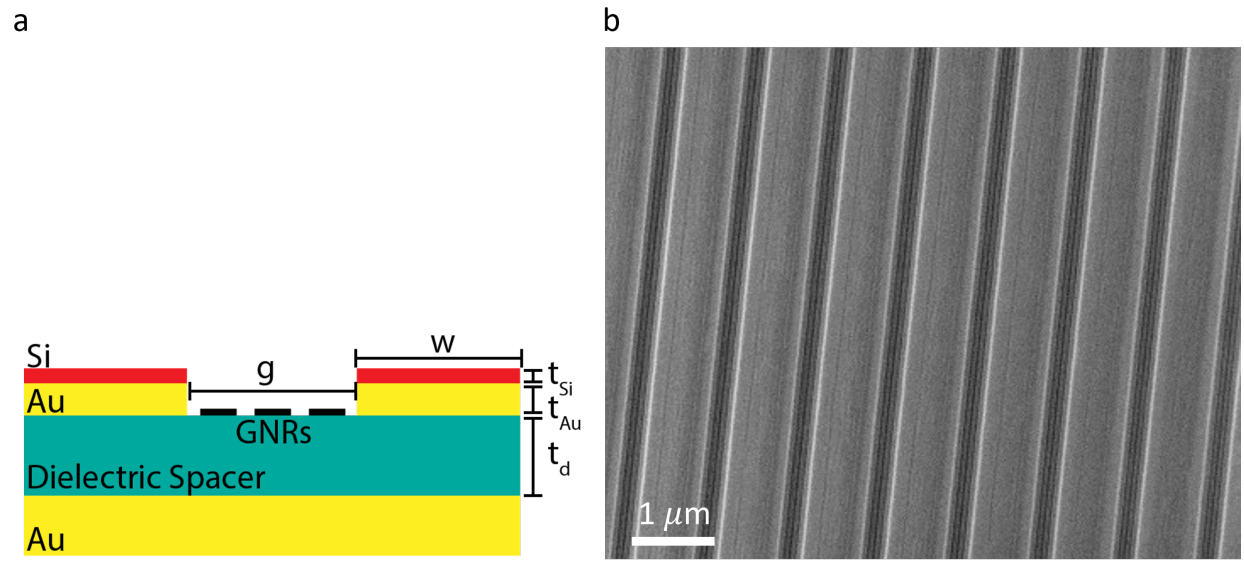

Figure 3.5: (a). Schematic representation of the proposed hybrid metastructure. (b). SEM image of an array of bars with graphioepitaxial aligned ribbons in the gaps on a 285 nm SiO_2/Si substrate with w = 800 nm, g = 180 nm, t_{Si} = 50 nm, t_{Au} = 30 nm, and t_d = 285 nm.

The sample in Figure 3.5 was measured in the FTIR at various locations, corresponding to areas with and without graphene and with and without the metastructure, as shown in Figure 3.6. The two aligned structures should nominally be identical (patterned with the same parameters on the same day, but on different locations of the chip), barring the presence of graphene. When the aligned structure is present, the overall transmission behavior is reduced when compared to that of the bare substrates. There is also a variation in the resonance of the aligned with and without GNRs present that may indicate the presence of the GNRs affecting the resonance. However, the measurements of the bare substrate and bare GNRs does not show any variation that would indicate the presence of a plasmonic mode in the GNRs as seen in the previous section and the variation is across a much larger bandwidth than the expected GNR response. This indicates that any variation we are observing is not due to the GNRs, but some variation in the patterns themselves.[4]

[4]The next step for this type of work would be to recreate this result of SiO2/Si, but make a tunable device. Measure the GNR resonance in an area off the aligned ribbons to confirm the presence of the GNR plasmon, then measure the behavior in the aligned ribbons. Maintaining the same location, but changing the Fermi level will remove any doubt of structure variations. While not as strongly enhanced as the designs discussed later, the SiO2/Si structure should still show some signal enhancement from a fraction of a percent

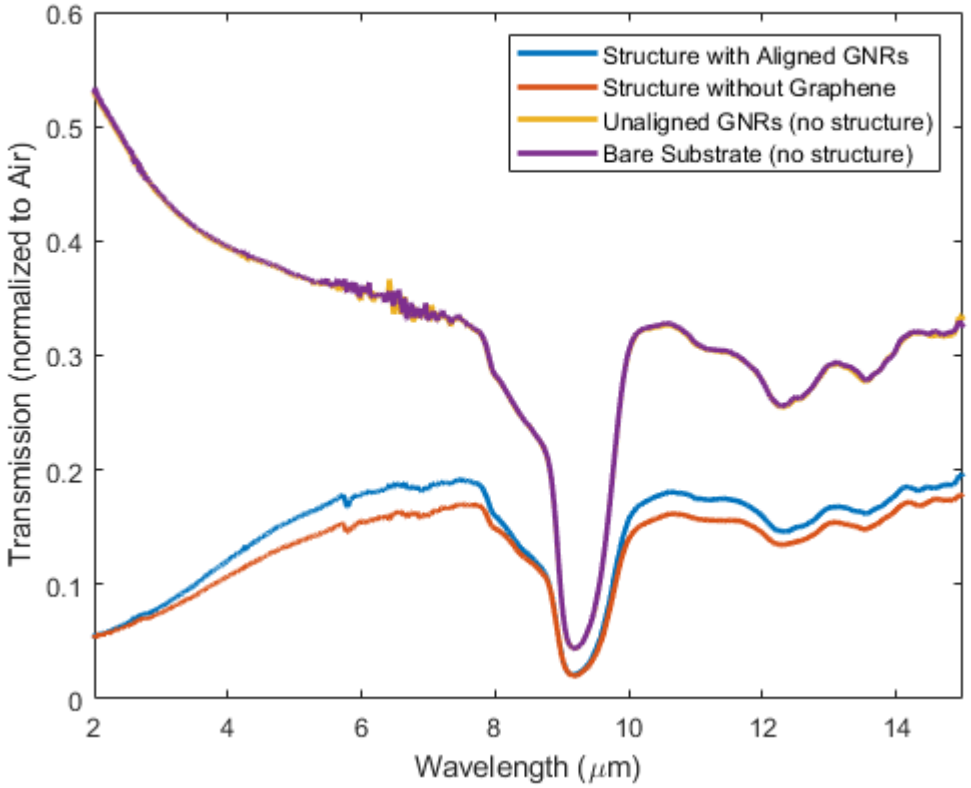

Figure 3.6: Experimental transmission data taken at four points on the same sample: metastructure with aligned GNRs in the gaps, metastructure without aligned GNRs in the gaps (no graphene was present underneath), no metastructure (so no alignment) GNRs, and no GNRs present. The later two measurements are in principle the same as those taken in the previous section.

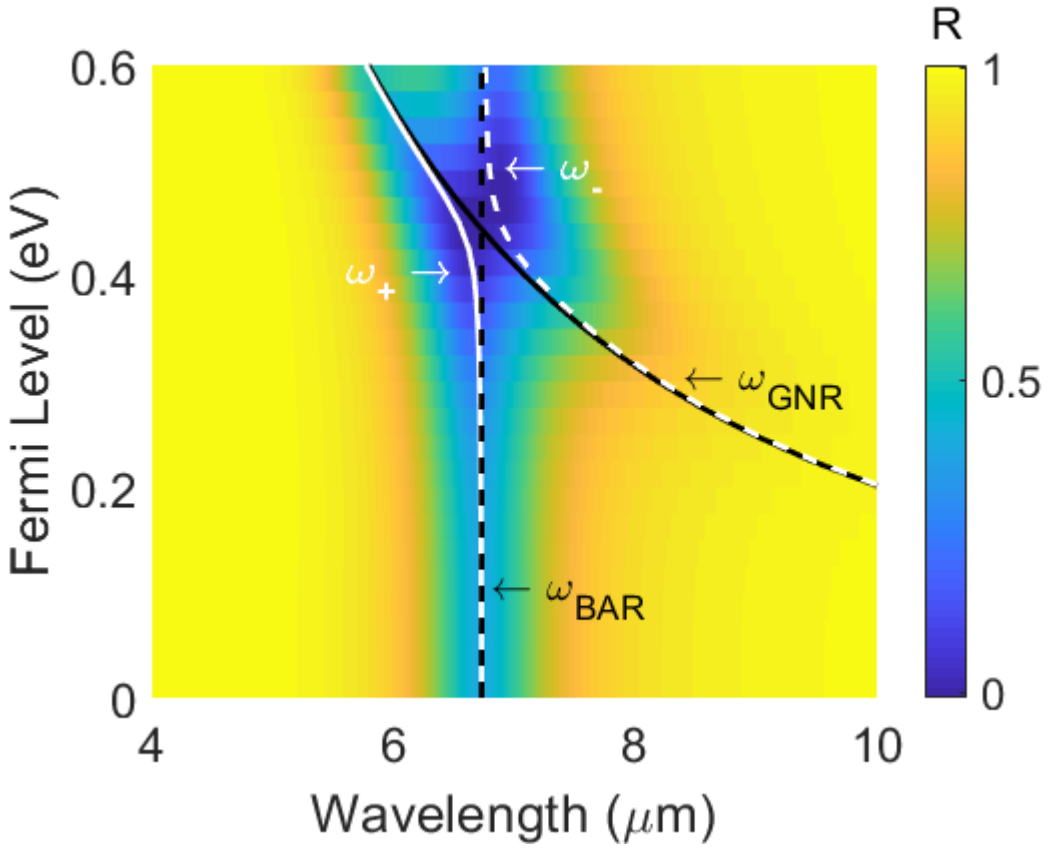

Figure 3.7: Reflection behavior of the hybrid metasurface as a function of wavelength and Fermi level. Black solid/dashed lines correspond to the resonance of the GNRs/Bar ($\omega_{GNR}/\omega_{Bar}$) and the white solid/dashed lines correspond to the upper/lower branches of hybridized modes (ω_+/ω_-). w = 1230 nm, g = 180 nm, t_{Si} = 10 nm, t_{Au} = 80 nm, t_d = 100 nm, and the dielectric spacer is SiN.

The operating principle of this device is that the resonance of the bars will produce a strongly localized electric field in the gap, which can then strongly couple to the localized resonance of the GNRs in the gap [19, 20, 127]. The behavior can then be described by an anti-crossing mode of two strongly coupled resonances [127, 128]

$$\omega_{\pm} = \frac{\omega_{BAR}^2 + \omega_{GNR}^2}{2} \pm \sqrt{\frac{(\omega_{BAR}^2 - \omega_{GNR}^2)^2}{4} + \beta^2 \omega_{BAR}^2 \omega_{GNR}^2} \tag{3.1}$$

where ω_{BAR} is the resonance of the bars, ω_{GNR} is the resonance of the GNRs and β is the coupling parameter. This theoretical framework is used in Figure 3.7 to accurately model the simulated behavior of the hybrid structure.

The coupling behavior, and consequent resonance enhancement, occurs once a threshold Fermi level is reached and ω_{GNR} is near in energy to ω_{BAR}. At lower Fermi levels, the anti-crossing mode does not occur, leaving the uncoupled resonance of the GNRs to be present. By adjusting the bar dimensions and dielectric spacer, the response of the system can be tailored, in our case, to maximize the tunability of the resonance. This can be seen in Figure 3.8, as changing the bar dimensions from 800 nm to 1200 nm red-shifts ω_{BAR} from 6.6 μm to 8 μm and the hybridized mode occurs at a lower Fermi level, correspondingly increasing the tuning range.

3.2.2 Summary and Outlook

Block copolymer lithography presented a solution to patterning large areas with nanostructures. However, the random orientation of the BCP limits the potential optical behaviors in comparison to a precisely ordered structure. However, by topographically patterning the substrate, i.e. graphioepitaxy, order can be enforced on the self-assembly process. In addition, the topographic structure can be designed to also have an optical response that couples to that of the GNRs. As a proof of concept, a theoretical graphioepitaxy GNR metamaterial was designed that can tune a reflection dip across the MIR spectrum with a demonstration of the graphioepitaxy alignment for the potential structure. This demonstration represents

to a few percent and be measurable in an FTIR. Fabrication details can be found in the fabrication section of the dissertation.

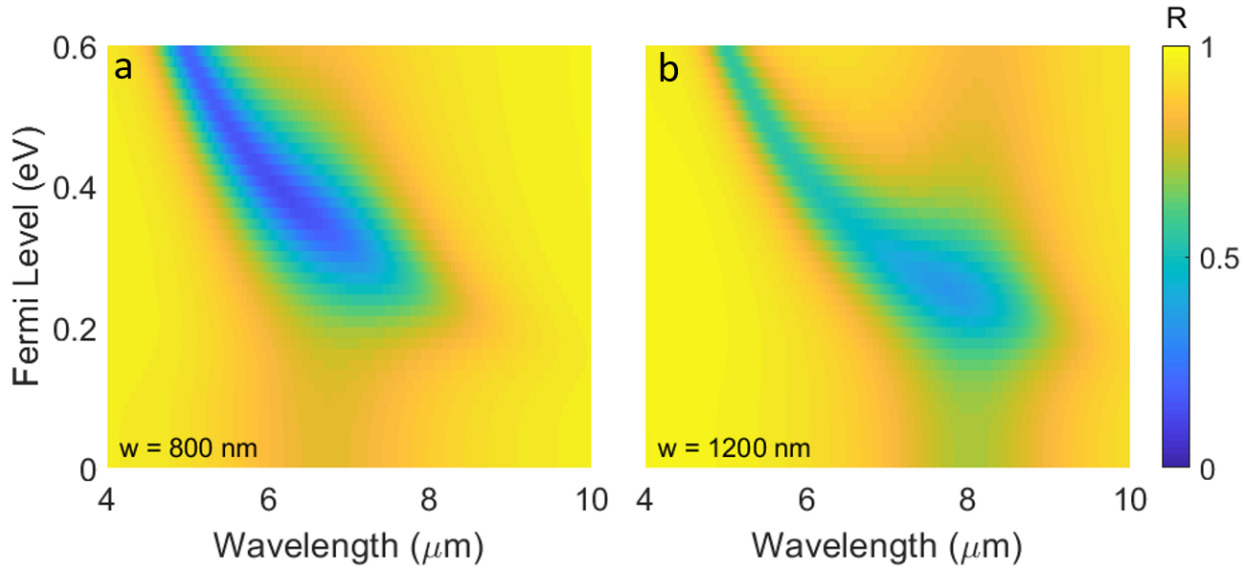

Figure 3.8: Reflection behavior of two hybrid metasurfaces as a function of wavelength and Fermi level with varying bar width. In (a), w = 800 nm and in (b), w = 1200 nm. All other constants are the same between a and b: g = 180 nm, t_{Si} = 50 nm, t_{Au} = 30 nm, t_d = 500 nm, and the dielectric spacer is Al_2O_3.

the simplest type of structure, a periodic array of bars, but more complicated designs are possible, such as curved structures, varied bar dimensions and gap sizes, different sidewall materials, etc., all of which can induce more complex optical responses. Graphioepitaxy advances the general BCP benefits of large scale patterning with nanoscale features to become compatible with more advanced optical design. As a further extension, this technique was shown to work with graphene, enabling a new technique for the fabrication of tunable metamaterials.

Chapter 4

Dynamic Beam Steering of Thermal Emission by Graphene-Metal Metasurface

4.1 Introduction

[1]

The mid infrared (MIR) regime is an important band of light for applications ranging from free-space laser communications[129] to chemical sensing applications[130, 131]. A narrowband source with high-speed directional control of the emitted light is required for these applications. Typically, the beam-steering can be controlled with mechanical devices [132] (such as gimbal-mounted mirrors), optical phased arrays of antenna that can control the relative phase of each element[19, 133], or more recently, liquid crystal-based geometries[134]. While each technique has its own set of advantages and disadvantages, one limitation common to them all is that they require an external source of light, such as the bulky and expensive quantum cascade laser.

An alternative source of MIR light is one that can be found everywhere, thermal radiation. Any material at a non-zero temperature will, due to the movement of charged particles, emit radiation over a broad range of frequencies. The thermal radiation from a generic material will be incoherent, isotropic, and broadband, making it a seemingly poor choice for

[1]The results discussed in this section are unpublished, but a paper based on this chapter is expected to published.

narrowband, directional steering applications. However, recent advances in nanoengineering have demonstrated that it is possible to engineer the emissivity of a structured material to create narrowband [135], anisotropic[136] , or coherent thermal radiation sources[136]. Heating the sample is all that is necessary to produce the desired light, thus providing an efficient source of MIR radiation. However, the above examples are static and unable to be dynamically tuned.

Recently, graphene has been considered as a candidate material to be incorporated into thermal engineered devices to enable active control of the thermal emission[137]. Graphene, a two-dimensional lattice of carbon atoms, can undergo significant changes to its optical permittivity in the MIR by changing its charge-carrier density via electronic control[24]. It has been theoretically predicted and experimentally demonstrated [137] that graphene can dynamically tune blackbody emissions, however no angular tuning at a constant magnitude has been demonstrated.

In the present work, we experimentally demonstrate the active control of angular thermal emission for a continuous range up to +/- 16^o around 1500 cm^{-1}. The device is controlled through electronic control of the carrier density of graphene that is incorporated into the metastructure illustrated in Figure 4.1. The metasurface emits the thermal radiation into angular lobes, with the electrostatically tuned graphene beneath the grating changing the interference condition of the emitted light, actively tuning the angle of emission.

4.2 Results

4.2.1 Tunable, Directional Thermal Emitter Device Geometry and Beam Steering Mechanism

Following Kirchhoff's law, altering the absorptivity of a thermal emitter by an engineered optical structures is equivalent to altering the emissivity to obtain the desired spatial and temporal thermal emission spectrum[138]. Directional thermal absorption/emission can be obtained by the constructive interference between adjacent antenna elements in the device, which correspond to thermally excited dipoles in the thermal emitter. Thermal dipoles,

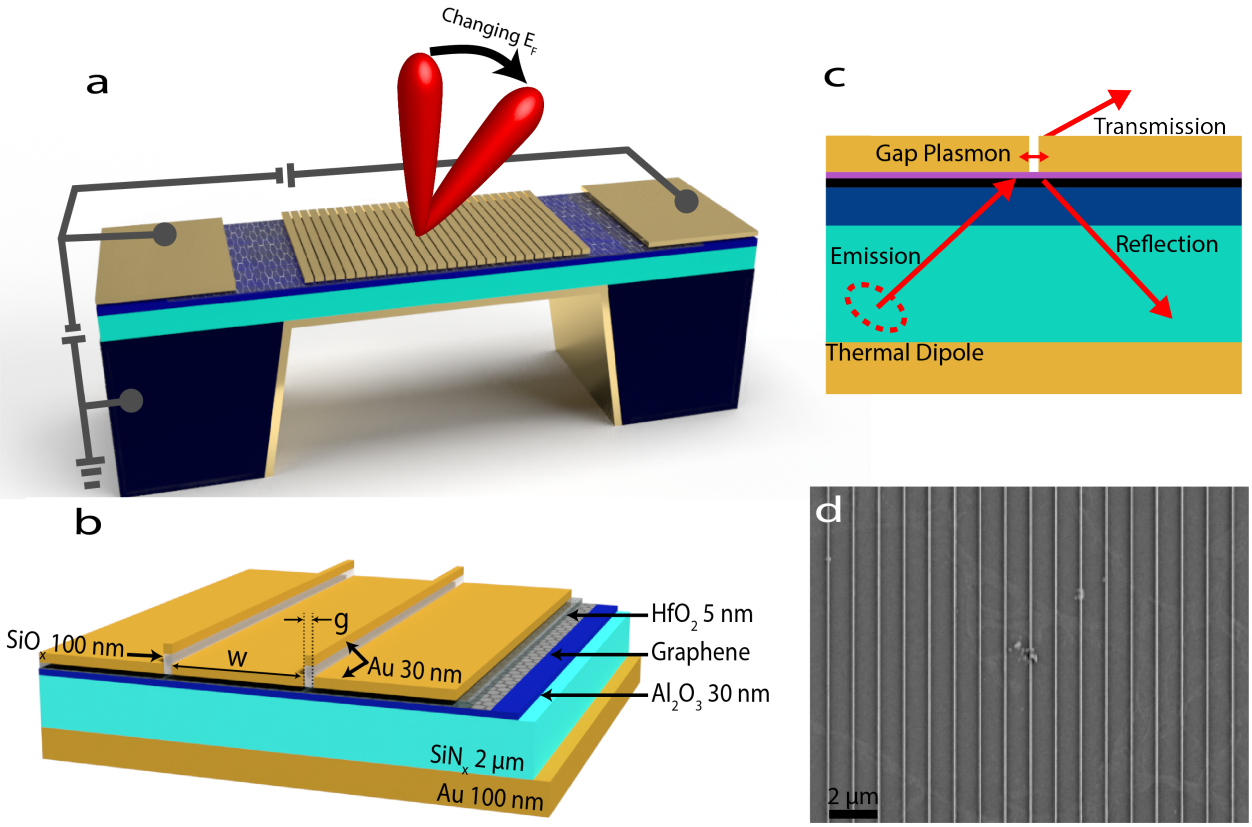

Figure 4.1: (a) Cartoon schematic of thermal emitter. (b). Detailed schematic of the design parameters. (c). Conceptual illustration of device operation. Thermal dipole emits radiation that couples to a Fabry-Perot resonance and upon interaction with the metasurface, a gap plasmon is formed that strongly couples the light to graphene, enabling a variable phase of reflection. (d). SEM image of the thermal emitter.

however, are excited at random spatial and temporal positions, not well ordered as required for constructive interference. To obtain directional thermal emission, the dominant emission pathway should be a spatially delocalized resonant optical mode such that the only emitting thermal dipoles are coupled to and in phase with this resonant optical mode. All other dipoles will not emit radiation out of the device, keeping the energy within the thermal emitter. The operating principle behind this specific device is that a Fabry-Perot mode is supported in the thick dielectric sandwich between the back-gate electrode and metasurface where the emission profile can be modulated by altering the reflection phase change at the

graphene interface[24, 136].

A schematic of the device geometry are shown in Figure 4.1 (see methods for measurement setup). The device consists of 30 nm thick, 1 micron wide gold nanoresonators spaced 40 nm apart on top of a material stack that consists of 5 nm of HfO_2, a graphene sheet, 30 nm of Al_2O_3, and a 2 micron SiN membrane with a gold back reflector that also serves as the backgate electrode. A bilayer of 100 nm thick SiOx and 30 nm of gold is within the space between the gold nanoresonators, a result of the negative tone resist used to pattern the structure via Electron Beam Lithography (see methods). The patterned area dimensions are 4 mm x 4 mm and the membrane is supported on a 200 micron thick Si frame. Electrical contact to the graphene is made by wire bonding to separated gold electrodes through the thin protective layer of HfO_2.

To measure the thermal emission of the active region, the sample (with electrical connections for gating) is placed on a heating stage with positioning and rotational control. The acceptance angle of the emitted light was 3^o and because the signal is polarized along the gold nanoresonator, a polarizer was used.

4.2.2 Tunable Emission Measurements on Thermal Emitter

Figure 4.2a (left axis) shows the emissivity at 250^oC of the device at normal incidence for two doped graphene Fermi levels, doped via a backgate geometry (see Figure 4.1a). The emissivity of the structure is calculated by normalizing the emitted radiation of our sample to the emitted radiation of a reference carbon nanotube blackbody (see right axis). By electrostatically tuning the graphene's Fermi level from 0.3 eV to 0.6 eV (corresponding to 560V and -560V respectively), the emission peak red-shifts from 1500 cm^{-1} to 1450 cm^{-1}, indicating that the thermal emission peaks are broadly tunable with minor variation in the intensity.

To investigate the angle dependent features of these emission peaks, we rotated the sample and measured the change in emissivity as a function of emission angle, as seen in Figure 4.2b. These measurements are for a constant doping value and temperature. By increasing the

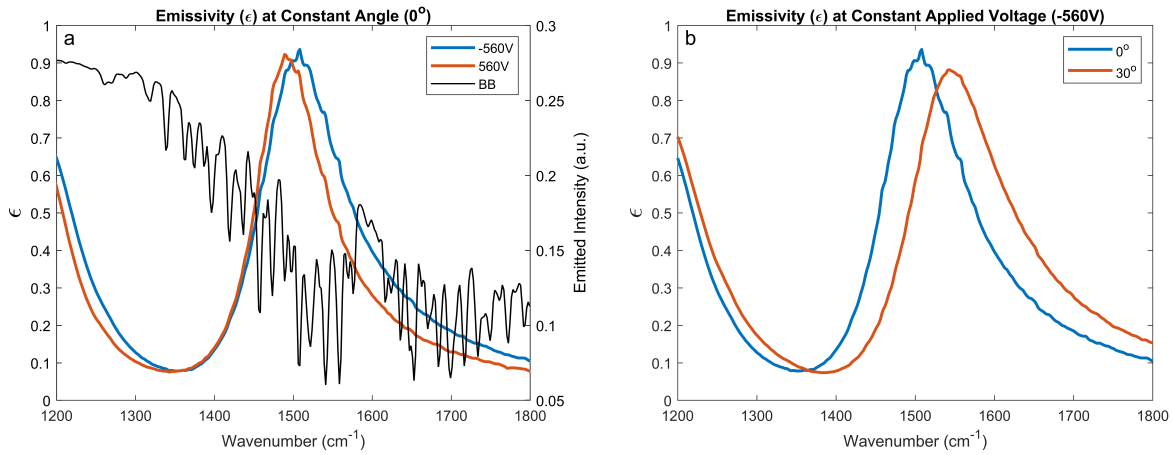

Figure 4.2: Experimental emission results (a) Emissivity tunability as a function of applied voltage. Emitted thermal radiation from carbon nanotubes, the black body (BB) reference. (b) Angle dependence of emissivity at a constant applied voltage. All measurements were taken at 250^{o}C and the black body reference is assumed to have emissivity equal to unity.

emission measurement angle from 0^o to 30^o, we observe a blue-shift in the thermal radiation feature, confirming the structures directional thermal emission. This result is consistent with previous results for similar angle dependent thermal emitters [136]. A minor reduction in the peak intensity at the larger angle (30^o) is in part due to measurement area elongating at larger angles to include some low emissivity, unpatterned gold areas, reducing the apparent emission peak magnitude. There are also higher order features present around 2400 cm^{-1} that show similar, but more limited shifting as seen in Figure 4.3.

4.2.3 Tuning angular dependence of the emissivity at a specific wavelength

Figure 4.4 plots the angle dependent emissivity of the hybrid graphene-metastructure as a function of doping value for a wavenumber of 1508 cm^{-1}. The emission peaks form lobes ranging from 0^o at high doping and 16^o at low doping. For the doping value of 0.6 eV, we observe that emission peak is most intense at normal incidence and decreases in intensity as the angle is increased. As the Fermi level is decreased, the lobe shifts from normal incidence to increasing angles, up to 16^o, allowing for continuous tuning in that range.

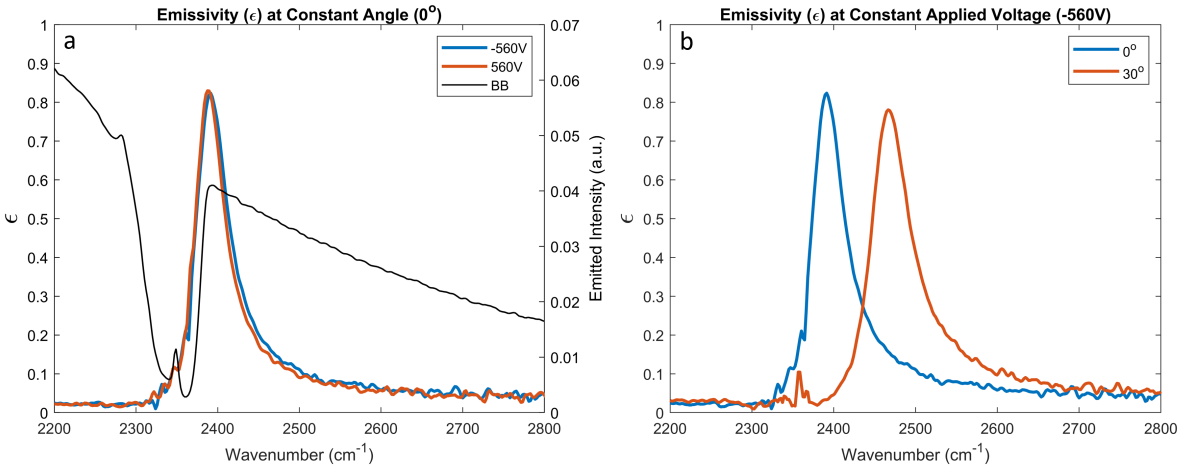

Figure 4.3: Experimental emission results (a) Emissivity tunability as a function of applied voltage. Emitted thermal radiation from carbon nanotubes, the black body (BB) reference. (b) Angle dependence of emissivity at a constant applied voltage. Same measurements as Figure 4.2, but for a different wavenumber range.

4.3 Discussion

In the proposed structure, spatially delocalized resonant optical mode is the vertically oscillating Fabry-Perot (F-P) resonance in the dielectric stack. The resonance condition of the F-P mode is electrically modulated by altering the surface impedance of the graphene-based metasurface. Resonant emission for the F-P mode occurs when the out-of-plane wavevector k_{out}, satisfies the constructive interference condition,

$$2k_{\text{out}}h + \phi_{\text{m}} + \phi_{\text{b}} = 2\pi * m \tag{4.1}$$

where ϕ_m and ϕ_b are phases shift of propagating optical mode upon reflection at metasurface and bottom reflector, respectively, h is the thickness of the dielectric spacer, and m is an integer. In the infrared range, the metallic film acts as a perfect electric conductor, resulting in $\phi_{\text{b}} \approx \pi$. The out-of-plane wavevector can be equivalently defined in terms of the angle the light is traveling in the F-P cavity, $\theta_{\text{F-P}}$ and momentum in the cavity, $k_{\text{F-P}}$ i.e.

$$k_{\text{out}} = k_{\text{F-P}} cos(\theta_{\text{F-P}}) \tag{4.2}$$

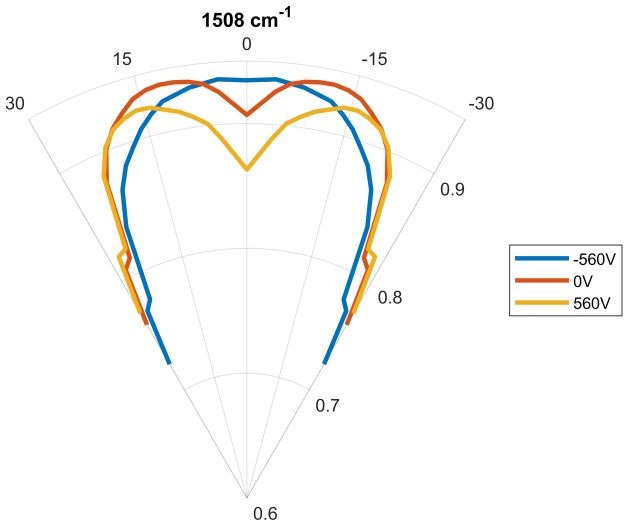

Figure 4.4: Experimental tuning of the emission lobes for three applied voltages.

The angle of emission in free space, θ_{free}, for the oscillating F-P mode can then be derived from Snell's law as

$$k_{\text{F-P}} sin(\theta_{\text{F-P}}) = k_{\text{free}} sin(\theta_{\text{free}}) \tag{4.3}$$

We note that ϕ_{b} and $k_{\text{out}}h$ are both independent of the graphene sheet's Fermi level.

In contrast, the reflection phase shift, ϕ_{m}, of the graphene-based metasurface depends on the optical conductivity of the graphene sheet. The metal metasurface forms a gap plasmon that strongly enhances the light matter interaction at the graphene interface, deviating from the perfect metallic mirror reflection. Figure 4.5(a) shows the phase of reflection coefficient of the graphene-based metasurface for transverse magnetic polarized light as a function of the Fermi level. As the Fermi level is increased, the optical losses of the gap plasmon are increased, further deviating the reflection phase from that of a perfect mirror, changing ϕ_{m}. We emphasize that the source of reflection phase shift is not due to a graphene plasmon, but due to the strong interaction of the F-P resonance at the graphene surface. Consequently, a change in ϕ_{m} will require a change in the angle of emission, θ_{free}, to maintain the constructive interference condition.

To model and optimize our structure, we made use of both FEM and FDTD simulation methods. These results are plotted in Figure 4.5b for our experimental device. The overall

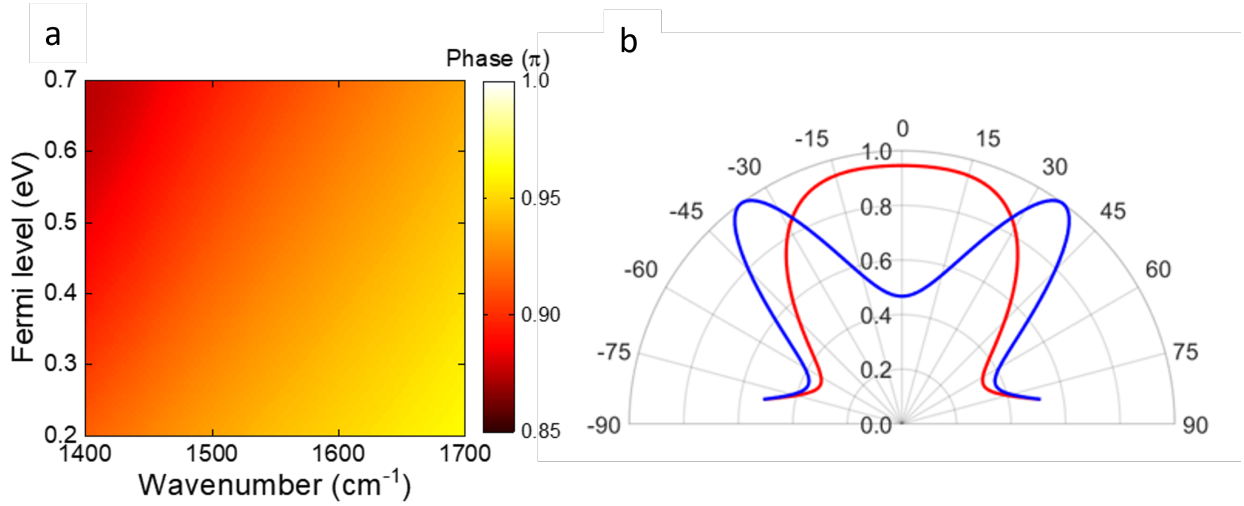

Figure 4.5: (a) Calculated values of ϕ_m as a function of Fermi level. (b) Theoretical emission lobes for the device.

behavior is consistent with our experimental observations (see Figure 4.4), but the emission lobes are broader and the tuning range of the emitter is less in our experiment than was theoretically predicted. The likely sources of this inconsistency is the metasustructure width variations across the full 4 x 4 mm^2 device (as shown in Figure 4.6), nonlocal interactions in the graphene, and carrier density variation during the heating process.

The power of the thermal emitter measured in this text can be calculated from Planck's law for the spectral radiance of a gray body. Using the measured emissivity ($\sim$0.9) and bandwidth of constant angular tuning (4 cm^{-1}), we calculate that the emitted power over the full 4 mm x 4 mm area would be $\approx$ 0.14 mW. This emission power requires, allowing for convection and radiation loss, 200 mW to maintain the temperature of the device, leading to an extremely efficient MIR source.

An important distinction between this device and other, more conventional LED or laser sources is the underlying physics of this device. According to Planck's law, all objects at non-zero temperatures will emit thermal radiation across the electromagnetic spectrum, with the exact wavelengths and strength dependent on the temperature of the object. Our device was designed to maximize the signal tuning around 1500 cm^{-1}, but the design principle is not limited to this particular wavenumber and can be applied across the mid-infrared spectrum

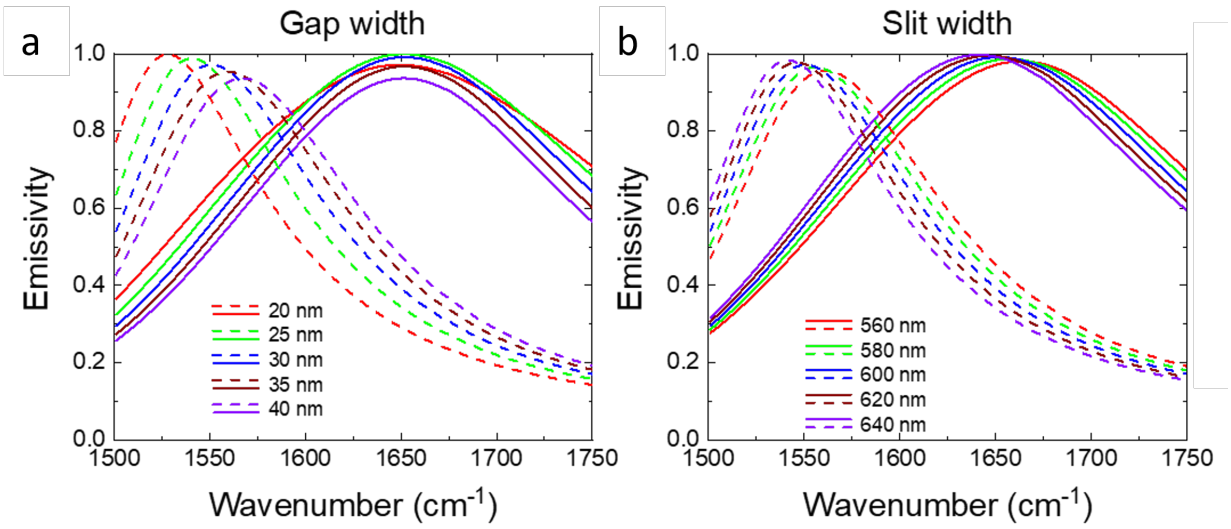

Figure 4.6: Variation of emission resonance for various geometric parameters. Dashed lines correspond to low Fermi levels and solid lines correspond to high Fermi levels.

or beyond. And while this device was designed to maximize the tunability of graphene, the mechanism only required the changing of the reflection phase which may be achievable by other 2D or 3D materials not considered in this work.

4.4 Conclusion

In conclusion, we have demonstrated a thermal emitter that can continuously change the angle of emission for a designated frequency. A Fabry-Perot like optical mode is excited by the thermal dipole and the phase of reflection at the metasurface is modulated by the Fermi level of graphene. The modulation is strengthened by the gap-plasmon, strongly coupling the electric fields to the graphene surface. For device simplicity, the SiN served as both the F-P cavity and the dielectric gate for the electrostatic gating of graphene. As a result, voltages on the order of hundreds of volts were required to gate the graphene, presenting a practical limitation on the achievable tuning range. By divorcing the dielectric gate from the SiN cavity, such as the inclusion of a doped semiconductor separated from graphene by 10s of nanometers of some dielectric, the gating can be accomplished with a significantly smaller voltage, allowing for a larger doping range and therefore larger tuning range.

This structure forms an efficient source of tunable MIR radiation that can operate without the need for mechanical[132], optical phase arrays [19, 133] or liquid crystals [134] based geometries. In addition, our device operates on a different set of principles than typical thermal steerers which take advantage of the momentum matching of a grating structure to out-couple light [136], instead relying on a supported Fabry-Perot mode in the structure. We hope this work may serve as inspiration for new approaches to controlling thermal emission.

Bibliography

[1] J. Siegel, A. Y. Wang, S. G. Menabde, M. A. Kats, M. S. Jang, and V. W. Brar, "Self-stabilizing laser sails based on optical metasurfaces," *ACS Photonics*, Jun. 2019. DOI: 10.1021/acsphotonics.9b00484. [Online]. Available: https://doi.org/10.1021/acsphotonics.9b00484.

[2] M. M. Salary and H. Mosallaei, "Photonic metasurfaces as relativistic light sails for doppler-broadened stable beam-riding and radiative cooling," *Laser & Photonics Reviews*, vol. 14, no. 8, p. 1 900 311, Aug. 2020, ISSN: 1863-8880, 1863-8899. DOI: 10.1002/lpor.201900311.

[3] W. S. V. M. Cai, *Optical metamaterials : fundamentals and applications*. 2009. [Online]. Available: http://site.ebrary.com/id/10355916.

[4] B. Slovick, Z. G. Yu, M. Berding, and S. Krishnamurthy, "Perfect dielectric-metamaterial reflector," *Physical Review B*, vol. 88, no. 16, p. 165 116, Oct. 2013, ISSN: 1098-0121, 1550-235X. DOI: 10.1103/PhysRevB.88.165116.

[5] N. Yu *et al.*, "Light propagation with phase discontinuities: Generalized laws of reflection and refraction," *Science*, vol. 334, 333—337, 2011. DOI: 10.1126/science.1210713.

[6] N. Yu and F. Capasso, "Flat optics with designer metasurfaces," *Nature Materials*, vol. 13, 139—150, 2014. DOI: 10.1038/nmat3839.

[7] D. Sell, J. Yang, S. Doshay, R. Yang, and J. A. Fan, "Large-angle, multifunctional metagratings based on freeform multimode geometries," *Nano Letters*, vol. 17, 3752—3757, 2017. DOI: 10.1021/acs.nanolett.7b01082.

[8] D. Fattal, J. Li, Z. Peng, M. Fiorentino, and R. G. Beausoleil, "Flat dielectric grating reflectors with focusing abilities," *Nature Photonics*, vol. 4, no. 7, DOI: 10.1038/nphoton.2010.116.

[9] J. Valentine, J. Li, T. Zentgraf, G. Bartal, and X. Zhang, "An optical cloak made of dielectrics," *Nature Materials*, vol. 8, no. 7, pp. 568–571, 2009, ISSN: 1476-4660. DOI: 10.1038/nmat2461. [Online]. Available: https://doi.org/10.1038/nmat2461.

[10] C. Kittel, *Introduction to Solid State Physics*, 8th ed. Wiley, 2004, ISBN: 9780471415268. [Online]. Available: http://www.amazon.com/Introduction-Solid-Physics-Charles-Kittel/dp/047141526X/ref=dp_ob_title_bk.

[11] H.-T. Chen, A. J. Taylor, and N. Yu, "A review of metasurfaces: Physics and applications," *Reports on Progress in Physics*, vol. 79, no. 7, p. 076 401, Jul. 2016, ISSN: 0034-4885, 1361-6633. DOI: 10.1088/0034-4885/79/7/076401.

[12] D. Fattal, J. Li, Z. Peng, M. Fiorentino, and R. G. Beausoleil, "Flat dielectric grating reflectors with focusing abilities," *Nature Photonics*, vol. 4, p. 466, 2010.

[13] G. Zheng, H. Mühlenbernd, M. Kenney, G. Li, T. Zentgraf, and S. Zhang, "Metasurface holograms reaching 80% efficiency," *Nature Nanotechnology*, vol. 10, 308—312, 2015. DOI: 10.1038/nnano.2015.2.

[14] X. Liu and W. J. Padilla, "Dynamic manipulation of infrared radiation with mems metamaterials," en, *Advanced Optical Materials*, vol. 1, no. 8, 559–562, Aug. 2013, ISSN: 21951071. DOI: 10.1002/adom.201300163.

[15] C. Xu, G. T. Stiubianu, and A. A. Gorodetsky, "Adaptive infrared-reflecting systems inspired by cephalopods," *Science*, vol. 359, no. 6383, pp. 1495–1500, 2018. DOI: 10.1126/science.aar5191. [Online]. Available: https://www.science.org/doi/abs/10.1126/science.aar5191.

[16] M. A. Kats *et al.*, "Vanadium dioxide as a natural disordered metamaterial: Perfect thermal emission and large broadband negative differential thermal emittance," *Physical Review X*, vol. 3, 2013. DOI: 10.1103/physrevx.3.041004.

[17] A. Shahsafi *et al.*, "Temperature-independent thermal radiation," *Proceedings of the National Academy of Sciences*, vol. 116, no. 52, pp. 26 402–26 406, 2019. DOI: 10.1073/pnas.1911244116. eprint: https://www.pnas.org/doi/pdf/10.1073/pnas.1911244116. [Online]. Available: https://www.pnas.org/doi/abs/10.1073/pnas.1911244116.

[18] M. S. Jang *et al.*, "Tunable large resonant absorption in a midinfrared graphene salisbury screen," *Physical Review B*, vol. 90, no. 16, p. 165 409, Oct. 2014. DOI: 10.1103/PhysRevB.90.165409.

[19] S. Han, S. Kim, S. Kim, T. Low, V. W. Brar, and M. S. Jang, "Complete complex amplitude modulation with electronically tunable graphene plasmonic metamolecules," *ACS Nano*, vol. 14, no. 1, pp. 1166–1175, 2020, ISSN: 1936-086X (Electronic) 1936-0851 (Linking). DOI: 10.1021/acsnano.9b09277. [Online]. Available: https://www.ncbi.nlm.nih.gov/pubmed/31904220.

[20] S. Kim, M. S. Jang, V. W. Brar, K. W. Mauser, L. Kim, and H. A. Atwater, "Electronically tunable perfect absorption in graphene," *Nano Lett*, vol. 18, no. 2, pp. 971–979, 2018, ISSN: 1530-6992 (Electronic) 1530-6984 (Linking). DOI: 10.1021/acs.nanolett.7b04393. [Online]. Available: https://www.ncbi.nlm.nih.gov/pubmed/29320203.

[21] P. Goncalves and N. Peres, *An Introduction to Graphene Plasmonics*. World Scientific, 2016. DOI: https://doi.org/10.1142/9948.

[22] K. S. Novoselov *et al.*, "Electric field effect in atomically thin carbon films," *Science*, vol. 306, no. 5696, pp. 666–669, 2004. DOI: 10.1126/science.1102896. eprint: https://www.science.org/doi/pdf/10.1126/science.1102896. [Online]. Available: https://www.science.org/doi/abs/10.1126/science.1102896.

[23] Y. Zhang, L. Zhang, and C. Zhou, "Review of chemical vapor deposition of graphene and related applications," *Accounts of Chemical Research*, vol. 46, no. 10, pp. 2329–2339, 2013, PMID: 23480816. DOI: 10.1021/ar300203n. eprint: https://doi.org/10.1021/ar300203n. [Online]. Available: https://doi.org/10.1021/ar300203n.

[24] V. W. Brar, M. S. Jang, M. Sherrott, J. J. Lopez, and H. A. Atwater, "Highly confined tunable mid-infrared plasmonics in graphene nanoresonators," *Nano Lett*, vol. 13, no. 6, pp. 2541–7, 2013, ISSN: 1530-6992 (Electronic) 1530-6984 (Linking). DOI: 10.1021/nl400601c. [Online]. Available: https://www.ncbi.nlm.nih.gov/pubmed/23621616.

[25] J. F. Siegel *et al.*, "Using bottom-up lithography and optical nonlocality to create short-wave infrared plasmonic resonances in graphene," *ACS Photonics*, vol. 8, no. 5, pp. 1277–1285, 2021. DOI: 10.1021/acsphotonics.1c00149. [Online]. Available: https://doi.org/10.1021/acsphotonics.1c00149.

[26] L. A. Falkovsky, *Journal of Physics: Conference Series*, 2008.

[27] *Breakthrough initiatives*, https://breakthroughinitiatives.org/initiative/3, 2021. [Online]. Available: https://breakthroughinitiatives.org/initiative/3, (accessed: 07.11.2021).

[28] Y. Yang, W. Wang, P. Moitra, I. I. Kravchenko, D. P. Briggs, and J. Valentine, "Dielectric meta-reflectarray for broadband linear polarization conversion and optical vortex generation," *Nano letters*, vol. 14, pp. 1394–1399, 2014.

[29] F. Aieta, M. A. Kats, P. Genevet, and F. Capasso, "Multiwavelength achromatic metasurfaces by dispersive phase compensation," *Science*, vol. 347, pp. 1342–1345, 2015.

[30] M. Khorasaninejad *et al.*, "Achromatic metasurface lens at telecommunication wavelengths," *Nano letters*, vol. 15, pp. 5358–5362, 2015.

[31] W. Zhao, B. Liu, H. Jiang, J. Song, Y. Pei, and Y. Jiang, "Full-color hologram using spatial multiplexing of dielectric metasurface," *Optics letters*, vol. 41, pp. 147–150, 2016.

[32] E. Karimi, S. A. Schulz, I. D. Leon, H. Qassim, J. Upham, and R. W. Boyd, "Generating optical orbital angular momentum at visible wavelengths using a plasmonic metasurface," *Light: Science & Applications*, vol. 3, 2014. DOI: 10.1038/lsa.2014.48.

[33] J. Cheng, D. Ansari-Oghol-Beig, and H. Mosallaei, "Wave manipulation with designer dielectric metasurfaces," *Optics Letters*, vol. 39, p. 6285, 2014. DOI: 10.1364/ol.39.006285.

[34] M. Decker *et al.*, "High-efficiency dielectric huygens' surfaces," *Advanced Optical Materials*, vol. 3, 813—820, 2015. DOI: 10.1002/adom.201400584.

[35] Z. Ma *et al.*, "Terahertz all-dielectric magnetic mirror metasurfaces," *ACS Photonics*, vol. 3, 1010—1018, 2016. DOI: 10.1021/acsphotonics.6b00096.

[36] R. C. Devlin, M. Khorasaninejad, W. T. Chen, J. Oh, and F. Capasso, "Broadband high-efficiency dielectric metasurfaces for the visible spectrum," *Proceedings of the National Academy of Sciences*, vol. 113, 10 473—10478, 2016. DOI: 10.1073/pnas.1611740113.

[37] D. Lin, P. Fan, E. Hasman, and M. L. Brongersma, "Dielectric gradient metasurface optical elements," *Science*, vol. 345, 298—302, 2014. DOI: 10.1126/science.1253213.

[38] X. Ni, A. V. Kildishev, and V. M. Shalaev, "Metasurface holograms for visible light," *Nature Communications*, vol. 4, 2013. DOI: 10.1038/ncomms3807.

[39] L. Huang *et al.*, "Three-dimensional optical holography using a plasmonic metasurface," *Nature Communications*, vol. 4, 2013. DOI: 10.1038/ncomms3808.

[40] P. R. West *et al.*, "All-dielectric subwavelength metasurface focusing lens," *Optics Express*, vol. 22, p. 26 212, 2014. DOI: 10.1364/oe.22.026212.

[41] P. Moitra, B. A. Slovick, Z. Gang Yu, S Krishnamurthy, and J. Valentine, "Experimental demonstration of a broadband all-dielectric metamaterial perfect reflector," *Applied Physics Letters*, vol. 104, p. 171 102, 2014.

[42] P. Moitra *et al.*, "Large-scale all-dielectric metamaterial perfect reflectors," *ACS Photonics*, vol. 2, pp. 692–698, 2015.

[43] J.-S. Ye, N. Matsuyama, Y. Kanamori, and K. Hane, "Silicon suspended resonant grating filters fabricated from a silicon-on-insulator wafer," *IEEE Photonics Technology Letters*, vol. 20, 851–853, 2008. DOI: 10.1109/lpt.2008.921840.

[44] Y. Wang, Y. Kanamori, J. Ye, H. Sameshima, and K. Hane, "Fabrication and characterization of nanoscale resonant gratings on thin silicon membrane," *Optics Express*, vol. 17, p. 4938, 2009. DOI: 10.1364/oe.17.004938.

[45] O. Ilic, C. M. Went, and H. A. Atwater, "Nanophotonic heterostructures for efficient propulsion and radiative cooling of relativistic light sails," *Nano Letters*, vol. 18, 5583––5589, 2018. DOI: 10.1021/acs.nanolett.8b02035.

[46] C. L. Holloway, E. F. Kuester, J. A. Gordon, J. Ohara, J. Booth, and D. R. Smith, "An overview of the theory and applications of metasurfaces: The two-dimensional equivalents of metamaterials," *IEEE Antennas and Propagation Magazine*, vol. 54, 10—35, 2012. DOI: 10.1109/map.2012.6230714.

[47] Z. Manchester and A. Loeb, "Stability of a light sail riding on a laser beam," *The Astrophysical Journal Letters*, vol. 837, p. L20, 2017.

[48] C. K. Birdsall and A. B. Langdon, *Plasma physics via computer simulation*. McGraw-Hill, 1985.

[49] M. Deserno, *How to generate exponentially correlated gaussian random numbers*.

[50] C. R. McInnes, *Solar sailing: technology, dynamics, and mission applications*. Springer, 2004.

[51] J. P. Moura, R. A. Norte, J. Guo, C. Schäfermeier, and S. Gröblacher, "Centimeter-scale suspended photonic crystal mirrors," *Optics Express*, vol. 26, p. 1895, 2018. DOI: 10.1364/oe.26.001895.

[52] S. Wang *et al.*, "Broadband achromatic optical metasurface devices," *Nature Communications*, vol. 8, 2017.

[53] B. Wang *et al.*, "Visible-frequency dielectric metasurfaces for multiwavelength achromatic and highly dispersive holograms," *Nano Letters*, vol. 16, 5235—5240, 2016. DOI: 10.1021/acs.nanolett.6b02326.

[54] T. Satō, "Spectral emissivity of silicon," *Japanese Journal of Applied Physics*, vol. 6, 339—347, 1967. DOI: 10.1143/jjap.6.339.

[55] N. Ravindra, S. Abedrabbo, W. Chen, F. Tong, A. Nanda, and A. Speranza, "Temperature-dependent emissivity of silicon-related materials and structures," *IEEE Transactions on Semiconductor Manufacturing*, vol. 11, 30—39, 1998. DOI: 10.1109/66.661282.

[56] P. J. Timans, "Emissivity of silicon at elevated temperatures," *Journal of Applied Physics*, vol. 74, 6353—6364, 1993. DOI: 10.1063/1.355159.

[57] R. Kitamura, L. Pilon, and M. Jonasz, "Optical constants of silica glass from extreme ultraviolet to far infrared at near room temperature," *Applied Optics*, vol. 46, p. 8118, 2007. DOI: 10.1364/ao.46.008118.

[58] C. Schinke *et al.*, "Uncertainty analysis for the coefficient of band-to-band absorption of crystalline silicon," *AIP Advances*, vol. 5, p. 067 168, 2015. DOI: 10.1063/1.4923379.

[59] W. Streyer *et al.*, "Engineering absorption and blackbody radiation in the far-infrared with surface phonon polaritons on gallium phosphide," *Applied Physics Letters*, vol. 104, p. 131 105, 2014. DOI: 10.1063/1.4870255.

[60] X. Liu, T. Tyler, T. Starr, A. F. Starr, N. M. Jokerst, and W. J. Padilla, "Taming the blackbody with infrared metamaterials as selective thermal emitters," *Physical Review Letters*, vol. 107, 2011. DOI: 10.1103/physrevlett.107.045901.

[61] C. Arnold *et al.*, "Coherent thermal infrared emission by two-dimensional silicon carbide gratings," *Physical Review B*, vol. 86, 2012. DOI: 10.1103/physrevb.86.035316.

[62] S.-H. Wu *et al.*, "Thermal homeostasis using microstructured phase-change materials," *Optica*, vol. 4, p. 1390, 2017. DOI: 10.1364/optica.4.001390.

[63] M. E. Semenov, D. V. Shevlyakova, and P. A. Meleshenko, "Inverted pendulum under hysteretic control: Stability zones and periodic solutions," *Nonlinear Dynamics*, vol. 75, 247—256, 2013. DOI: 10.1007/s11071-013-1062-x.

[64] T. Low and P. Avouris, "Graphene plasmonics for terahertz to mid-infrared applications," *ACS Nano*, vol. 8, no. 2, pp. 1086–1101, 2014, ISSN: 1936-0851. DOI: 10.1021/nn406627u. [Online]. Available: https://doi.org/10.1021/nn406627uhttps://pubs.acs.org/doi/pdf/10.1021/nn406627u.

[65] A. N. Grigorenko, M. Polini, and K. S. Novoselov, "Graphene plasmonics," *Nature Photonics*, vol. 6, no. 11, pp. 749–758, 2012, ISSN: 1749-4885 1749-4893. DOI: 10.1038/nphoton.2012.262.

[66] M. Jablan, M. Soljacic, and H. Buljan, "Plasmons in graphene: Fundamental properties and potential applications," *Proceedings of the IEEE*, vol. 101, no. 7, pp. 1689–1704, 2013, ISSN: 0018-9219 1558-2256. DOI: 10.1109/jproc.2013.2260115.

[67] A. Cagliani, D. M. A. Mackenzie, L. K. Tschammer, F. Pizzocchero, K. Almdal, and P. Bøggild, "Large-area nanopatterned graphene for ultrasensitive gas sensing," *Nano Research*, vol. 7, no. 5, pp. 743–754, 2014, ISSN: 1998-0124 1998-0000. DOI: 10.1007/s12274-014-0435-x.

[68] D. Rodrigo *et al.*, "Mid-infrared plasmonic biosensing with graphene," *Science*, vol. 349, no. 6244, p. 165, 2015. DOI: 10.1126/science.aab2051. [Online]. Available: http://science.sciencemag.org/content/349/6244/165.abstracthttps://science.sciencemag.org/content/sci/349/6244/165.full.pdf.

[69] Y. Li *et al.*, "Graphene plasmon enhanced vibrational sensing of surface-adsorbed layers," *Nano Lett*, vol. 14, no. 3, pp. 1573–7, 2014, ISSN: 1530-6992 (Electronic) 1530-6984 (Linking). DOI: 10.1021/nl404824w. [Online]. Available: https://www.ncbi.nlm.nih.gov/pubmed/24528250.

[70] A. Andryieuski and A. V. Lavrinenko, "Graphene metamaterials based tunable terahertz absorber: Effective surface conductivity approach," *Opt Express*, vol. 21, no. 7, pp. 9144–55, 2013, ISSN: 1094-4087 (Electronic) 1094-4087 (Linking). DOI: 10.1364/OE.21.009144. [Online]. Available: https://www.ncbi.nlm.nih.gov/pubmed/23572003.

[71] F. Xia, T. Mueller, Y.-m. Lin, A. Valdes-Garcia, and P. Avouris, "Ultrafast graphene photodetector," *Nature Nanotechnology*, vol. 4, no. 12, pp. 839–843, 2009, ISSN: 1748-3395. DOI: 10.1038/nnano.2009.292. [Online]. Available: https://doi.org/10.1038/nnano.2009.292.

[72] T. Mueller, F. Xia, and P. Avouris, "Graphene photodetectors for high-speed optical communications," *Nature Photonics*, vol. 4, no. 5, pp. 297–301, 2010, ISSN: 1749-4893. DOI: 10.1038/nphoton.2010.40. [Online]. Available: https://doi.org/10.1038/nphoton.2010.40.

[73] M. Freitag, T. Low, W. Zhu, H. Yan, F. Xia, and P. Avouris, "Photocurrent in graphene harnessed by tunable intrinsic plasmons," *Nature Communications*, vol. 4, no. 1, p. 1951, 2013, ISSN: 2041-1723. DOI: 10.1038/ncomms2951. [Online]. Available: https://doi.org/10.1038/ncomms2951.

[74] Q. Guo *et al.*, "Efficient electrical detection of mid-infrared graphene plasmons at room temperature," *Nature Materials*, vol. 17, no. 11, pp. 986–992, 2018, ISSN: 1476-4660. DOI: 10.1038/s41563-018-0157-7. [Online]. Available: https://doi.org/10.1038/s41563-018-0157-7.

[75] H. Yan *et al.*, "Tunable infrared plasmonic devices using graphene/insulator stacks," *Nat Nanotechnol*, vol. 7, no. 5, pp. 330–4, 2012, ISSN: 1748-3395 (Electronic) 1748-3387 (Linking). DOI: 10.1038/nnano.2012.59. [Online]. Available: https://www.ncbi.nlm.nih.gov/pubmed/22522668.

[76] Z. Li, K. Yao, F. Xia, S. Shen, J. Tian, and Y. Liu, "Graphene plasmonic metasurfaces to steer infrared light," *Sci Rep*, vol. 5, p. 12 423, 2015, ISSN: 2045-2322 (Electronic) 2045-2322 (Linking). DOI: 10.1038/srep12423. [Online]. Available: https://www.ncbi.nlm.nih.gov/pubmed/26201677.

[77] Z. Li and N. Yu, "Modulation of mid-infrared light using graphene-metal plasmonic antennas," *Applied Physics Letters*, vol. 102, no. 13, 2013, ISSN: 0003-6951 1077-3118. DOI: 10.1063/1.4800931.

[78] Y. Fan, N.-H. Shen, T. Koschny, and C. M. Soukoulis, "Tunable terahertz metasurface with graphene cut-wires," *ACS Photonics*, vol. 2, no. 1, pp. 151–156, 2015, ISSN: 2330-4022 2330-4022. DOI: 10.1021/ph500366z.

[79] X. Zhu *et al.*, "Plasmon-phonon coupling in large-area graphene dot and antidot arrays fabricated by nanosphere lithography," *Nano Lett*, vol. 14, no. 5, pp. 2907–13, 2014, ISSN: 1530-6992 (Electronic) 1530-6984 (Linking). DOI: 10.1021/nl500948p. [Online]. Available: https://www.ncbi.nlm.nih.gov/pubmed/24707792.

[80] K. K. Gopalan *et al.*, "Scalable and tunable periodic graphene nanohole arrays for mid-infrared plasmonics," *Nano Lett*, vol. 18, no. 9, pp. 5913–5918, 2018, ISSN: 1530-6992 (Electronic) 1530-6984 (Linking). DOI: 10.1021/acs.nanolett.8b02613. [Online]. Available: https://www.ncbi.nlm.nih.gov/pubmed/30114919.

[81] M. Jablan, H. Buljan, and M. Soljačić, "Plasmonics in graphene at infrared frequencies," *Physical Review B*, vol. 80, no. 24, p. 245 435, 2009. DOI: 10.1103/PhysRevB.80.245435. [Online]. Available: https://link.aps.org/doi/10.1103/PhysRevB.80.245435https://journals.aps.org/prb/abstract/10.1103/PhysRevB.80.245435.

[82] H. Yan *et al.*, "Damping pathways of mid-infrared plasmons in graphene nanostructures," *Nature Photonics*, vol. 7, no. 5, pp. 394–399, 2013, ISSN: 1749-4885 1749-4893. DOI: 10.1038/nphoton.2013.57.

[83] Z. Fang *et al.*, "Gated tunability and hybridization of localized plasmons in nanostructured graphene," *ACS Nano*, vol. 7, no. 3, pp. 2388–2395, 2013, ISSN: 1936-0851. DOI: 10.1021/nn3055835. [Online]. Available: https://doi.org/10.1021/nn3055835https://pubs.acs.org/doi/pdf/10.1021/nn3055835.

[84] F. H. Koppens, D. E. Chang, and F. J. Garcia de Abajo, "Graphene plasmonics: A platform for strong light-matter interactions," *Nano Lett*, vol. 11, no. 8, pp. 3370–7, 2011, ISSN: 1530-6992 (Electronic) 1530-6984 (Linking). DOI: 10.1021/nl201771h. [Online]. Available: https://www.ncbi.nlm.nih.gov/pubmed/21766812.

[85] K. J. Tielrooij *et al.*, "Electrical control of optical emitter relaxation pathways enabled by graphene," *Nature Physics*, vol. 11, no. 3, pp. 281–287, 2015, ISSN: 1745-2473 1745-2481. DOI: 10.1038/nphys3204.

[86] N. Rivera, I. Kaminer, B. Zhen, J. D. Joannopoulos, and M. Soljačić, "Shrinking light to allow forbidden transitions on the atomic scale," *Science*, vol. 353, no. 6296, p. 263, 2016. DOI: 10.1126/science.aaf6308. [Online]. Available: http://science.sciencemag.org/content/353/6296/263.abstract.

[87] J. Zhang, R. W. Crisp, J. Gao, D. M. Kroupa, M. C. Beard, and J. M. Luther, "Synthetic conditions for high-accuracy size control of pbs quantum dots," *The Journal of Physical Chemistry Letters*, vol. 6, no. 10, pp. 1830–1833, 2015. DOI: 10.1021/acs.jpclett.5b00689. [Online]. Available: https://doi.org/10.1021/acs.jpclett.5b00689.

[88] I. Moreels, Y. Justo, B. De Geyter, K. Haustraete, J. C. Martins, and Z. Hens, "Size-tunable, bright, and stable pbs quantum dots: A surface chemistry study," *ACS Nano*, vol. 5, no. 3, pp. 2004–2012, 2011, ISSN: 1936-0851. DOI: 10.1021/nn103050w. [Online]. Available: https://doi.org/10.1021/nn103050w.

[89] M. J. Dejneka *et al.*, "Rare earth-doped glass microbarcodes," *Proceedings of the National Academy of Sciences*, vol. 100, no. 2, p. 389, 2003. DOI: 10.1073/pnas.0236044100. [Online]. Available: http://www.pnas.org/content/100/2/389.abstract.

[90] K. F. Renk, "Quantum well lasers from the uv to the infrared," in *Basics of Laser Physics: For Students of Science and Engineering*, K. F. Renk, Ed. Cham: Springer International Publishing, 2017, pp. 485–490, ISBN: 978-3-319-50651-7. DOI: 10.1007/978-3-319-50651-7_24. [Online]. Available: https://doi.org/10.1007/978-3-319-50651-7_24.

[91] T. H. Chang *et al.*, "Directed self-assembly of block copolymer films on atomically-thin graphene chemical patterns," *Sci Rep*, vol. 6, p. 31 407, 2016, ISSN: 2045-2322 (Electronic) 2045-2322 (Linking). DOI: 10.1038/srep31407. [Online]. Available: https://www.ncbi.nlm.nih.gov/pubmed/27528258.

[92] Conference Paper, 2015. DOI: 10.1117/12.2085836.

[93] M. Kim, N. S. Safron, E. Han, M. S. Arnold, and P. Gopalan, "Fabrication and characterization of large-area, semiconducting nanoperforated graphene materials," *Nano Lett*, vol. 10, no. 4, pp. 1125–31, 2010, ISSN: 1530-6992 (Electronic) 1530-6984 (Linking). DOI: 10.1021/nl9032318. [Online]. Available: https://www.ncbi.nlm.nih.gov/pubmed/20192229.

[94] D. S. Lee *et al.*, "Selective protein transport through ultra-thin suspended reduced graphene oxide nanopores," *Nanoscale*, vol. 9, no. 36, pp. 13 457–13 464, 2017, ISSN: 2040-3372 (Electronic) 2040-3364 (Linking). DOI: 10.1039/c7nr01889d. [Online]. Available: https://www.ncbi.nlm.nih.gov/pubmed/28682407.

[95] D. Alcaraz Iranzo *et al.*, "Probing the ultimate plasmon confinement limits with a van der waals heterostructure," *Science*, vol. 360, no. 6386, p. 291, 2018. DOI: 10.1126/science.aar8438. [Online]. Available: http://science.sciencemag.org/content/360/6386/291.abstracthttps://science.sciencemag.org/content/sci/360/6386/291.full.pdf.

[96] W. Wang and J. M. Kinaret, "Plasmons in graphene nanoribbons: Interband transitions and nonlocal effects," *Physical Review B*, vol. 87, no. 19, 2013, ISSN: 1098-0121 1550-235X. DOI: 10.1103/PhysRevB.87.195424.

[97] I. Silveiro, J. M. P. Ortega, and F. J. G. de Abajo, "Quantum nonlocal effects in individual and interacting graphene nanoribbons," *Light: Science Applications*, vol. 4, no. 1, e241–e241, 2015, ISSN: 2047-7538. DOI: 10.1038/lsa.2015.14.

[98] S. Thongrattanasiri, A. Manjavacas, and F. J. García de Abajo, "Quantum finite-size effects in graphene plasmons," *ACS Nano*, vol. 6, no. 2, pp. 1766–1775, 2012, ISSN: 1936-0851. DOI: 10.1021/nn204780e. [Online]. Available: https://doi.org/10.1021/nn204780ehttps://pubs.acs.org/doi/pdf/10.1021/nn204780e.

[99] J. W. Choi, M. Kim, N. S. Safron, M. S. Arnold, and P. Gopalan, "Transfer of pre-assembled block copolymer thin film to nanopattern unconventional substrates," *ACS Appl Mater Interfaces*, vol. 6, no. 12, pp. 9442–8, 2014, ISSN: 1944-8252 (Electronic) 1944-8244 (Linking). DOI: 10.1021/am501816n. [Online]. Available: https://www.ncbi.nlm.nih.gov/pubmed/24869477.

[100] B. H. Kim *et al.*, "Mussel-inspired block copolymer lithography for low surface energy materials of teflon, graphene, and gold," *Advanced Materials*, vol. 23, no. 47, pp. 5618–+, 2011, ISSN: 0935-9648. DOI: 10.1002/adma.201103650. [Online]. Available: ⟨GotoISI⟩://WOS:000297788600003.

[101] X. Li *et al.*, "Large-area synthesis of high-quality and uniform graphene films on copper foils," *Science*, vol. 324, no. 5932, p. 1312, 2009. DOI: 10.1126/science.1171245. [Online]. Available: http://science.sciencemag.org/content/324/5932/1312.abstract.

[102] F. S. Bates and G. H. Fredrickson, "Block copolymer thermodynamics: Theory and experiment," *Annual Review of Physical Chemistry*, vol. 41, no. 1, pp. 525–557, 1990, ISSN: 0066-426X. DOI: 10.1146/annurev.pc.41.100190.002521. [Online]. Available: https://doi.org/10.1146/annurev.pc.41.100190.002521.

[103] L. Leibler, "Theory of microphase separation in block copolymers," *Macromolecules*, vol. 13, no. 6, pp. 1602–1617, 1980, ISSN: 0024-9297. DOI: 10.1021/ma60078a047. [Online]. Available: https://doi.org/10.1021/ma60078a047.

[104] K. Azuma *et al.*, "Self-assembly of an ultrahigh- block copolymer with versatile etch selectivity," *Macromolecules*, vol. 51, no. 16, pp. 6460–6467, 2018, ISSN: 0024-9297 1520-5835. DOI: 10.1021/acs.macromol.8b01409.

[105] L. Ju *et al.*, "Graphene plasmonics for tunable terahertz metamaterials," *Nat Nanotechnol*, vol. 6, no. 10, pp. 630–4, 2011, ISSN: 1748-3395 (Electronic) 1748-3387 (Linking). DOI: 10.1038/nnano.2011.146. [Online]. Available: https://www.ncbi.nlm.nih.gov/pubmed/21892164.

[106] Z. T. Wu *et al.*, "The influence of chemical solvents on the properties of cvd graphene," *Journal of Raman Spectroscopy*, vol. 46, no. 1, pp. 21–24, 2015, ISSN: 0377-0486. DOI: 10.1002/jrs.4582. [Online]. Available: https://onlinelibrary.wiley.com/doi/abs/10.1002/jrs.4582.

[107] C. F. Chen *et al.*, "Controlling inelastic light scattering quantum pathways in graphene," *Nature*, vol. 471, no. 7340, pp. 617–20, 2011, ISSN: 1476-4687 (Electronic) 0028-0836 (Linking). DOI: 10.1038/nature09866. [Online]. Available: https://www.ncbi.nlm.nih.gov/pubmed/21412234.

[108] J. Horng *et al.*, "Drude conductivity of dirac fermions in graphene," *Physical Review B*, vol. 83, no. 16, p. 165 113, 2011. DOI: 10.1103/PhysRevB.83.165113. [Online]. Available: https://link.aps.org/doi/10.1103/PhysRevB.83.165113https://journals.aps.org/prb/abstract/10.1103/PhysRevB.83.165113.

[109] L. A. Falkovsky and A. A. Varlamov, "Space-time dispersion of graphene conductivity," *The European Physical Journal B*, vol. 56, no. 4, pp. 281–284, 2007, ISSN: 1434-6028 1434-6036. DOI: 10.1140/epjb/e2007-00142-3.

[110] T. Christensen, W. Wang, A.-P. Jauho, M. Wubs, and N. A. Mortensen, "Classical and quantum plasmonics in graphene nanodisks: Role of edge states," *Physical Review B*, vol. 90, no. 24, 2014, ISSN: 1098-0121 1550-235X. DOI: 10.1103/PhysRevB.90.241414.

[111] N. A. Mortensen, S. Raza, M. Wubs, T. Sondergaard, and S. I. Bozhevolnyi, "A generalized non-local optical response theory for plasmonic nanostructures," *Nat Commun*, vol. 5, p. 3809, 2014, ISSN: 2041-1723 (Electronic) 2041-1723 (Linking). DOI: 10.1038/ncomms4809. [Online]. Available: https://www.ncbi.nlm.nih.gov/pubmed/24787630.

[112] G. Toscano, S. Raza, A.-P. Jauho, N. A. Mortensen, and M. Wubs, "Modified field enhancement and extinction by plasmonic nanowire dimers due to nonlocal response," *Optics Express*, vol. 20, no. 4, pp. 4176–4188, 2012. DOI: 10.1364/OE.20.004176. [Online]. Available: http://www.opticsexpress.org/abstract.cfm?URI=oe-20-4-4176https://www.osapublishing.org/oe/abstract.cfm?uri=oe-20-4-4176.

[113] X. Li, X. Wang, L. Zhang, S. Lee, and H. Dai, "Chemically derived, ultrasmooth graphene nanoribbon semiconductors," *Science*, vol. 319, no. 5867, p. 1229, 2008. DOI: 10.1126/science.1150878. [Online]. Available: http://science.sciencemag.org/content/319/5867/1229.abstracthttps://science.sciencemag.org/content/319/5867/1229.long.

[114] X. Wang, Y. Ouyang, X. Li, H. Wang, J. Guo, and H. Dai, "Room-temperature all-semiconducting sub-10-nm graphene nanoribbon field-effect transistors," *Physical Review Letters*, vol. 100, no. 20, p. 206 803, 2008. DOI: 10.1103/PhysRevLett.100.206803. [Online]. Available: https://link.aps.org/doi/10.1103/PhysRevLett.100.206803https://journals.aps.org/prl/abstract/10.1103/PhysRevLett.100.206803.

[115] M. Evaldsson, I. V. Zozoulenko, H. Xu, and T. Heinzel, "Edge-disorder-induced anderson localization and conduction gap in graphene nanoribbons," *Physical Review B*, vol. 78, no. 16, p. 161 407, 2008. DOI: 10.1103/PhysRevB.78.161407. [Online]. Available: https://link.aps.org/doi/10.1103/PhysRevB.78.161407https://journals.aps.org/prb/abstract/10.1103/PhysRevB.78.161407.

[116] M. Y. Han, B. Özyilmaz, Y. Zhang, and P. Kim, "Energy band-gap engineering of graphene nanoribbons," *Physical Review Letters*, vol. 98, no. 20, p. 206 805, 2007. DOI: 10.1103/PhysRevLett.98.206805. [Online]. Available: https://link.aps.org/doi/10.1103/PhysRevLett.98.206805https://journals.aps.org/prl/abstract/10.1103/PhysRevLett.98.206805.

[117] Z. Chen, Y.-M. Lin, M. J. Rooks, and P. Avouris, "Graphene nano-ribbon electronics," *Physica E: Low-dimensional Systems and Nanostructures*, vol. 40, no. 2, pp. 228–232, 2007, ISSN: 1386-9477. DOI: https://doi.org/10.1016/j.physe.2007.06.020. [Online]. Available: http://www.sciencedirect.com/science/article/pii/S1386947707001427https://www.sciencedirect.com/science/article/pii/S1386947707001427?via%3Dihub.

[118] L. Yang, C.-H. Park, Y.-W. Son, M. L. Cohen, and S. G. Louie, "Quasiparticle energies and band gaps in graphene nanoribbons," *Physical Review Letters*, vol. 99, no. 18, p. 186 801, 2007. DOI: 10.1103/PhysRevLett.99.186801. [Online]. Available: https://link.aps.org/doi/10.1103/PhysRevLett.99.186801https://journals.aps.org/prl/abstract/10.1103/PhysRevLett.99.186801.

[119] M. B. Lundeberg *et al.*, "Tuning quantum nonlocal effects in graphene plasmonics," *Science*, vol. 357, no. 6347, p. 187, 2017. DOI: 10.1126/science.aan2735. [Online]. Available: http://science.sciencemag.org/content/357/6347/187.abstracthttps://science.sciencemag.org/content/sci/357/6347/187.full.pdf.

[120] V. Apalkov and M. I. Stockman, "Proposed graphene nanospaser," *Light: Science Applications*, vol. 3, no. 7, e191–e191, 2014, ISSN: 2047-7538. DOI: 10.1038/lsa.2014.72.

[121] J. D. Caldwell *et al.*, "Low-loss, extreme subdiffraction photon confinement via silicon carbide localized surface phonon polariton resonators," *Nano Lett*, vol. 13, no. 8, pp. 3690–7, 2013, ISSN: 1530-6992 (Electronic) 1530-6984 (Linking). DOI: 10.1021/nl401590g. [Online]. Available: https://www.ncbi.nlm.nih.gov/pubmed/23815389.

[122] X. Yang, J. Yao, J. Rho, X. Yin, and X. Zhang, "Experimental realization of three-dimensional indefinite cavities at the nanoscale with anomalous scaling laws," *Nature Photonics*, vol. 6, no. 7, pp. 450–454, 2012, ISSN: 1749-4885 1749-4893. DOI: 10.1038/nphoton.2012.124.

[123] J. D. Caldwell *et al.*, "Sub-diffractional volume-confined polaritons in the natural hyperbolic material hexagonal boron nitride," *Nat Commun*, vol. 5, p. 5221, 2014, ISSN: 2041-1723 (Electronic) 2041-1723 (Linking). DOI: 10.1038/ncomms6221. [Online]. Available: https://www.ncbi.nlm.nih.gov/pubmed/25323633.

[124] R. Chikkaraddy *et al.*, "Single-molecule strong coupling at room temperature in plasmonic nanocavities," *Nature*, vol. 535, no. 7610, pp. 127–30, 2016, ISSN: 1476-4687 (Electronic) 0028-0836 (Linking). DOI: 10.1038/nature17974. [Online]. Available: https://www.ncbi.nlm.nih.gov/pubmed/27296227.

[125] I. Gunkel, "Directing block copolymer self-assembly on patterned substrates," *Small*, vol. 14, no. 46, p. 1 802 872, 2018. DOI: https://doi.org/10.1002/smll.201802872. eprint: https://onlinelibrary.wiley.com/doi/pdf/10.1002/smll.201802872. [Online]. Available: https://onlinelibrary.wiley.com/doi/abs/10.1002/smll.201802872.

[126] J. W. Choi, M. Kim, N. S. Safron, E. Han, M. S. Arnold, and P. Gopalan, "A facile route for fabricating graphene nanoribbon array transistors using graphoepitaxy of a symmetric block copolymer," in *Advanced Etch Technology for Nanopatterning IV*, Q. Lin, S. U. Engelmann, and Y. Zhang, Eds., International Society for Optics and Photonics, vol. 9428, SPIE, 2015, pp. 131 –140. DOI: 10.1117/12.2085836. [Online]. Available: https://doi.org/10.1117/12.2085836.

[127] P. Q. Liu *et al.*, "Highly tunable hybrid metamaterials employing split-ring resonators strongly coupled to graphene surface plasmons," *Nature Communications*, vol. 6, no. 1, p. 8969, 2015, ISSN: 2041-1723. DOI: 10.1038/ncomms9969. [Online]. Available: https://doi.org/10.1038/ncomms9969.

[128] L. Novotny, "Strong coupling, energy splitting, and level crossings: A classical perspective," *American Journal of Physics*, vol. 78, no. 11, pp. 1199–1202, 2010. DOI: 10.1119/1.3471177. eprint: https://doi.org/10.1119/1.3471177. [Online]. Available: https://doi.org/10.1119/1.3471177.

[129] P. Corrigan, R. Martini, E. A. Whittaker, and C. Bethea, "Quantum cascade lasers and the kruse model in free space optical communication," *Opt. Express*, vol. 17, no. 6, pp. 4355–4359, 2009. DOI: 10.1364/OE.17.004355. [Online]. Available: http://opg.optica.org/oe/abstract.cfm?URI=oe-17-6-4355.

[130] J. Haas and B. Mizaikoff, "Advances in mid-infrared spectroscopy for chemical analysis," *Annual Review of Analytical Chemistry*, vol. 9, no. 1, pp. 45–68, 2016, PMID: 27070183. DOI: 10.1146/annurev-anchem-071015-041507. eprint: https://doi.org/10.1146/annurev-anchem-071015-041507. [Online]. Available: https://doi.org/10.1146/annurev-anchem-071015-041507.

[131] D. Rodrigo *et al.*, "Mid-infrared plasmonic biosensing with graphene," *Science (New York, N.Y.)*, vol. 349, Jun. 2015. DOI: 10.1126/science.aab2051.

[132] B.-W. Yoo *et al.*, "Optical phased array using high contrast gratings for two dimensional beamforming and beamsteering," *Opt. Express*, vol. 21, no. 10, pp. 12 238–12 248, 2013. DOI: 10.1364/OE.21.012238. [Online]. Available: http://opg.optica.org/oe/abstract.cfm?URI=oe-21-10-12238.

[133] J. Sun, E. Timurdogan, A. Yaacobi, E. S. Hosseini, and M. R. Watts, "Large-scale nanophotonic phased array," *Nature*, vol. 493, no. 7431, pp. 195–199, 2013, ISSN: 1476-4687. DOI: 10.1038/nature11727. [Online]. Available: https://doi.org/10.1038/nature11727.

[134] J. A. Frantz *et al.*, "Chip-based nonmechanical beam steerer in the midwave infrared," *J. Opt. Soc. Am. B*, vol. 35, no. 12, pp. C29–C37, 2018. DOI: 10.1364/JOSAB.35.000C29. [Online]. Available: http://opg.optica.org/josab/abstract.cfm?URI=josab-35-12-C29.

[135] C. W. Hsu, B. Zhen, A. D. Stone, J. D. Joannopoulos, and M. Soljačić, "Bound states in the continuum," *Nature Reviews Materials*, vol. 1, no. 9, p. 16 048, 2016, ISSN: 2058-8437. DOI: 10.1038/natrevmats.2016.48. [Online]. Available: https://doi.org/10.1038/natrevmats.2016.48.

[136] J.-J. Greffet, R. Carminati, K. Joulain, J.-P. Mulet, S. Mainguy, and Y. Chen, "Coherent emission of light by thermal sources," *Nature*, vol. 416, no. 6876, 61–64, Mar. 2002, ISSN: 1476-4687. DOI: 10.1038/416061a.

[137] V. W. Brar *et al.*, "Electronic modulation of infrared radiation in graphene plasmonic resonators," *Nature Communications*, vol. 6, no. 1, p. 7032, 2015, ISSN: 2041-1723. DOI: 10.1038/ncomms8032. [Online]. Available: https://doi.org/10.1038/ncomms8032.

[138] G. Kirchhoff, "Ueber das verhältniss zwischen dem emissionsvermögen und dem absorptionsvermögen der körper für wärme und licht," *Annalen der Physik*, vol. 185, no. 2, pp. 275–301, 1860. DOI: https://doi.org/10.1002/andp.18601850205. eprint: https://onlinelibrary.wiley.com/doi/pdf/10.1002/andp.18601850205. [Online]. Available: https://onlinelibrary.wiley.com/doi/abs/10.1002/andp.18601850205.

[139] M. A. McCord and M. J. Rooks, *Handbook of microlithography, micromachining, and microfabrication*.

[140] V. Sidorkin, E. van der Drift, and H. Salemink, "Influence of hydrogen silsesquioxane resist exposure temperature on ultrahigh resolution electron beam lithography," *Journal of Vacuum Science & Technology B: Microelectronics and Nanometer Structures Processing, Measurement, and Phenomena*, vol. 26, no. 6, pp. 2049–2053, 2008. DOI: 10.1116/1.2987965. eprint: https://avs.scitation.org/doi/pdf/10.1116/1.2987965. [Online]. Available: https://avs.scitation.org/doi/abs/10.1116/1.2987965.

[141] V. R. Manfrinato *et al.*, "Resolution limits of electron-beam lithography toward the atomic scale," *Nano Letters*, vol. 13, no. 4, pp. 1555–1558, 2013, PMID: 23488936. DOI: 10.1021/nl304715p. eprint: https://doi.org/10.1021/nl304715p. [Online]. Available: https://doi.org/10.1021/nl304715p.

[142] J. Y. Kim *et al.*, "Full 2 tunable phase modulation using avoided crossing of resonances," *Nature Communications*,

[143] E. Huang, L. Rockford, T. P. Russell, and C. J. Hawker, "Nanodomain control in copolymer thin films," *Nature*, vol. 395, no. 6704, pp. 757–758, 1998, ISSN: 1476-4687. DOI: 10.1038/27358. [Online]. Available: https://doi.org/10.1038/27358.

[144] P. S. Johnson *et al.*, "Orientation of a monolayer of dipolar molecules on graphene from x-ray absorption spectroscopy," *Langmuir*, vol. 30, no. 9, pp. 2559–2565, 2014, PMID: 24520997. DOI: 10.1021/la500183b. eprint: https://doi.org/10.1021/la500183b. [Online]. Available: https://doi.org/10.1021/la500183b.

[145] M. Kim, N. S. Safron, C. Huang, M. S. Arnold, and P. Gopalan, "Light-driven reversible modulation of doping in graphene," *Nano Letters*, vol. 12, no. 1, pp. 182–187, 2012, PMID: 22149166. DOI: 10.1021/nl2032734. eprint: https://doi.org/10.1021/nl2032734. [Online]. Available: https://doi.org/10.1021/nl2032734.

[146] R. E. Rogers, T. I. Bardsley, S. J. Weinstein, and B. J. Landi, "Solution-phase adsorption of 1-pyrenebutyric acid using single-wall carbon nanotubes," *Chemical Engineering Journal*, vol. 173, no. 2, pp. 486–493, 2011, ISSN: 1385-8947. DOI: https://doi.org/10.1016/j.cej.2011.08.019. [Online]. Available: https://www.sciencedirect.com/science/article/pii/S1385894711009478.

[147] Y. Zhao *et al.*, "Functionalization of single-wall carbon nanotubes with chromophores of opposite internal dipole orientation," *ACS Applied Materials & Interfaces*, vol. 5, no. 19, pp. 9355–9361, 2013, PMID: 24060382. DOI: 10.1021/am4024753. eprint: https://doi.org/10.1021/am4024753. [Online]. Available: https://doi.org/10.1021/am4024753.

[148] Y. Wu, H. Fan, C. Yang, and L. Zhang, "Pyrene-based amphiphile regulated c60 aggregation in monolayers and langmuir–blodgett films," *Colloids and Surfaces A: Physicochemical and Engineering Aspects*, vol. 585, p. 124111, 2020, ISSN: 0927-7757. DOI: https://doi.org/10.1016/j.colsurfa.2019.124111. [Online]. Available: https://www.sciencedirect.com/science/article/pii/S0927775719311033.

Appendix A: Fabrication

A.1 Introduction

One of the foundational aspects of this work is the fabrication of the optical devices. In this appendix, we will overview the various nanofabrication techniques and tools used in this dissertation and some potential issues that may occur. Exact fabrication recipes are included with additional details provided in footnotes.

A.2 Lift-off Lithography

Lift-off lithography is a technique to create a pattern on the surface of a substrate using a sacrificial material and a deposited material. The sacrificial material (referred to as a resist) will be deposited onto the surface using a spincoater (see A.3) and then patterned using an electron beam lithography tool (see A.4). After the patterning, the uniform resist layer will now be removed in certain areas, exposing the substrate beneath. The material that we want patterned is then deposited using a metal evaporator (see A.5). The deposited material will coat the entire surface, with some parts directly connecting to the substrate and others only connecting to the resist layer After this step, the resist material is removed via an immersion in a solvent. The deposited material that is directly connecting the substrate will remain, whereas the material that was on the sacrificial layer will be removed with the solvent, leaving only the pattern. There are some processes involved that do not include a lift-off step, the material is deposited then the inter-facial layer remains.

A.2.1 Potential Issues

When working with a lift-off based lithography, there are two issues most likely to occur. The first is that the deposited material does not stick to the substrate and instead lifts-off when placed in the solvent. In my experience, that is because there is still is some of the resist present beneath the deposited material. As a result, the deposited material does not connect well to the surface and will be removed. This resist issue is discussed more in section A.4.1.

The secondary issue that may occur is that the resist does not get fully removed by the solvent, leading to a partial or non-existent lift-off. If the resist can be dissolved under normal circumstances with the solvent, the likely issue is that the solvent cannot reach the resist. If, for example, the deposited material was so thick that it fully encases the resist, the solvent cannot dissolve the resist so no lift-off will occur. A less extreme, but more likely to occur issue, is that the pattern itself is not-conducive to the lift-off process. Small, isolated structures (like tiny squares) are more difficult for the solvent to penetrate due to the limited surface area and the deposited material is more likely to stay on the surface as the enclosed nature means that it is difficult to agitate the isolated material to leave the surface. One solution to this issue is to create a pattern with thin connections between originally isolated regions. In this way, if one region starts to lift-off, it will assist all the other regions as they are connected as seen in Figure A.1.

A.3 Spincoater

The spincoater allows for the deposition of a uniform film of resist on the surface of a substrate. A liquid resist is added to the surface of the substrate, which is then spun at a controllable speed to create a uniform film of resist. The spin-speed controls the film thickness and is a resist dependent relation.

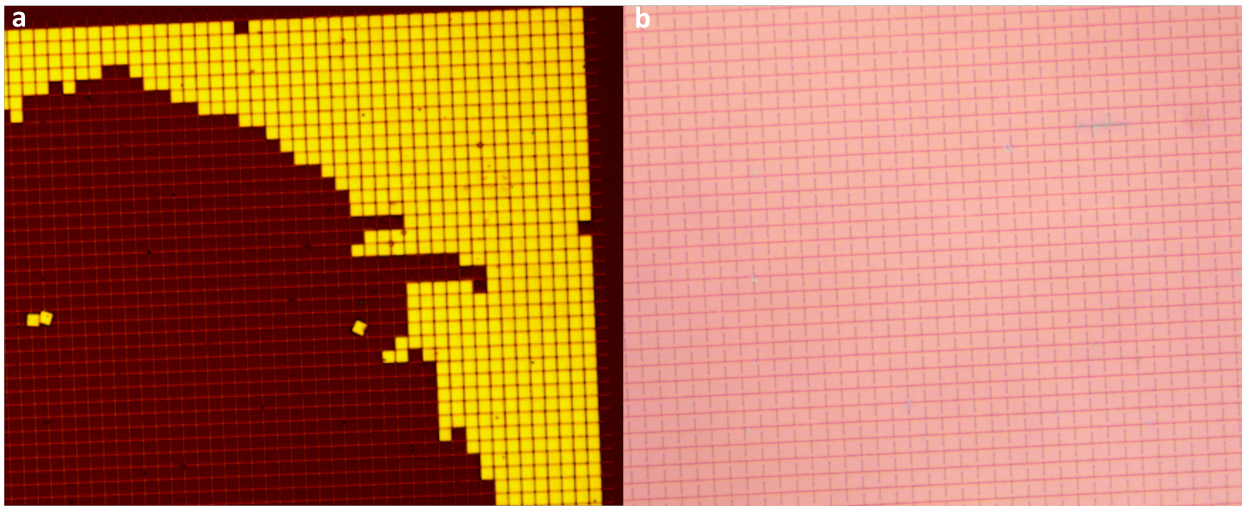

Figure A.1: Optical images of metal deposited to a substrate using lift-off lithography techniques. (a). Partial lift-off with enclosed structures. (b). Full lift-off when those squares are connected.

A.3.1 Suspended Membrane Samples

Special care is required when working with suspended membranes, such as the SiN membranes used in Chapter 4 for the thermal steerer device. To avoid damaging the membrane when spincoating, the SiN is glued to a carrier chip with PMMA on three corners so that the vacuum of the spincoater only interfaces with the carrier chip and not the SiN. As the processing of these samples require them to be put into low pressure environments, it is important that there is not a perfect seal between the membrane and the carrier chip so the PMMA is applied only to three corners to create an imperfect seal. Otherwise, there will be an area of low pressure (surrounding the membrane) and high pressure (between the membrane and the carrier chip) that risks destroying the membrane.

A.4 Electron Beam Lithography

Electron beam lithography (EBL) is a lithographic process that involves the direct writing of a pattern into an electron sensitive resist with a beam of electrons[139]. The electrons interact with the resist and alter the solubility, either weakening or strengthening the areas written. In the case of weakening, the areas written will be removed when immersed in a

developer (generally a solvent), referred to as a *positive-tone* resist. In the opposite case, the areas written will be the only portions to remain after immersion in the developer, which is referred to as a *negative-tone* resist. The main advantage of EBL is that it is a high-resolution process that can create patterns down to a few nanometers [140, 141] in size for any arbitrary design. However, the main limitation of EBL is that it is a low-throughput process, making it more appropriate for research and development applications, such as used in this work.

Resists in this work

- Polymethyl Methacrylate (PMMA) is a positive-tone resist used in Chapter 3.1
- Hydrogen silsesquioxane (HSQ) is a negative-tone resist used in Chapter 4

PMMA is a commonly used positive-tone resist that works well in combination with most lift-off techniques. The PMMA can easily be removed with common solvents, such as acetone or chloroform, allowing for an easy pattern transfer process. HSQ, a negative-tone resist, does not allow lift-off as the areas written are firmly adhered to the surface, but it is a much higher resolution resist than PMMA, allowing for features a few nanometers in size [140, 141]. But the issue remains that the HSQ will still be on the surface, potentially limiting the practicality of this resist. However, it is possible to combine both of these resists to take advantage of the PMMA easy removal and the high-resolution of the HSQ. First pattern the HSQ via EBL/development (note that the developer of HSQ, TMAH, does not develop PMMA), then transfer the pattern to the PMMA beneath via a reactive ion etch. The PMMA beneath the developed HSQ will be protected whereas the unprotected PMMA will be removed. Some material can then be deposited and then the PMMA can be removed as discussed above. Because the HSQ is only in contact with the PMMA, the HSQ will be removed along with the PMMA, allowing for a process that takes advantage of the benefits of both resists.

This process has been proposed to be used for a device that makes use of Si bars with

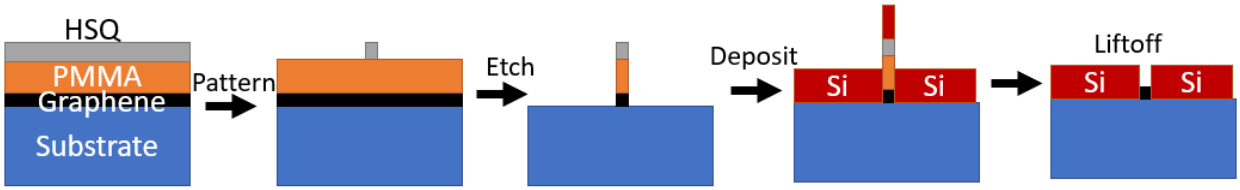

Figure A.2: Cartoon schematic of HSQ/PMMA fabrication process with graphene.

etched graphene ribbons in the gaps and demonstrated in Figure A.3. The exact details of the device are outside the scope of this work, but can be found in Ref [142]. The more vertical bars are resonant and the large bar going perpendicular is to assist in lift-off of the extremely narrow gaps. These images were taken at angle in the SEM, allowing us to see the gaps and sidewalls more clearly. [1]

A.4.1 Potential Issues

This section will detail potential issues when working with the EBL and the strategies to correct them. This is not meant to be an authoritative text, but to serve as an initial resource based solely on the author's experiences using this tool.

The first issue that is almost universally encountered is selecting the appropriate electron dose, where dose corresponds to the number of electrons interacting with the resist. If the dose is too low, then the resist will not be able to fully develop. For positive-tone resists, this results in the top portion of the resist being removed in the development, but the bottom portion will remain on the surface. The substrate beneath the resist will remain covered by the resist, so no deposition onto select areas can occur, which is generally what the positive-tone resist was used for in this work. For negative-tone, this results in the top portion of the resist remaining solid, but the bottom portion will be removed, taking the top portion with

[1]Fabrication details: 2000 RPM 950, 90 sec bake at 180C, wait for sample to cool down, then HSiQ at 3000 RPM. Dose ranged from 1000-1800 μC/cm^2. Development was 90 sec MF321, 30 sec DI water and a quick rinse of IPA. This is in contrast to other HSQ development that uses a 30 sec IPA bath. IPA is a solvent and can remove the PMMA, so we limit its time to just clean the surface. After the HSQ bars are created, a 4 minute etch in the RIE, 50-10-10 recipe (same recipe used in other sections, just different time). This recipe etches PMMA at a rate of 2 nm/sec, so 4 minutes ensures all of the PMMA is removed. Si is then deposited via the metal evaporator and liftoff is 90 minutes in acetone at 40C with low power sonication to assist in removal from the small gaps.

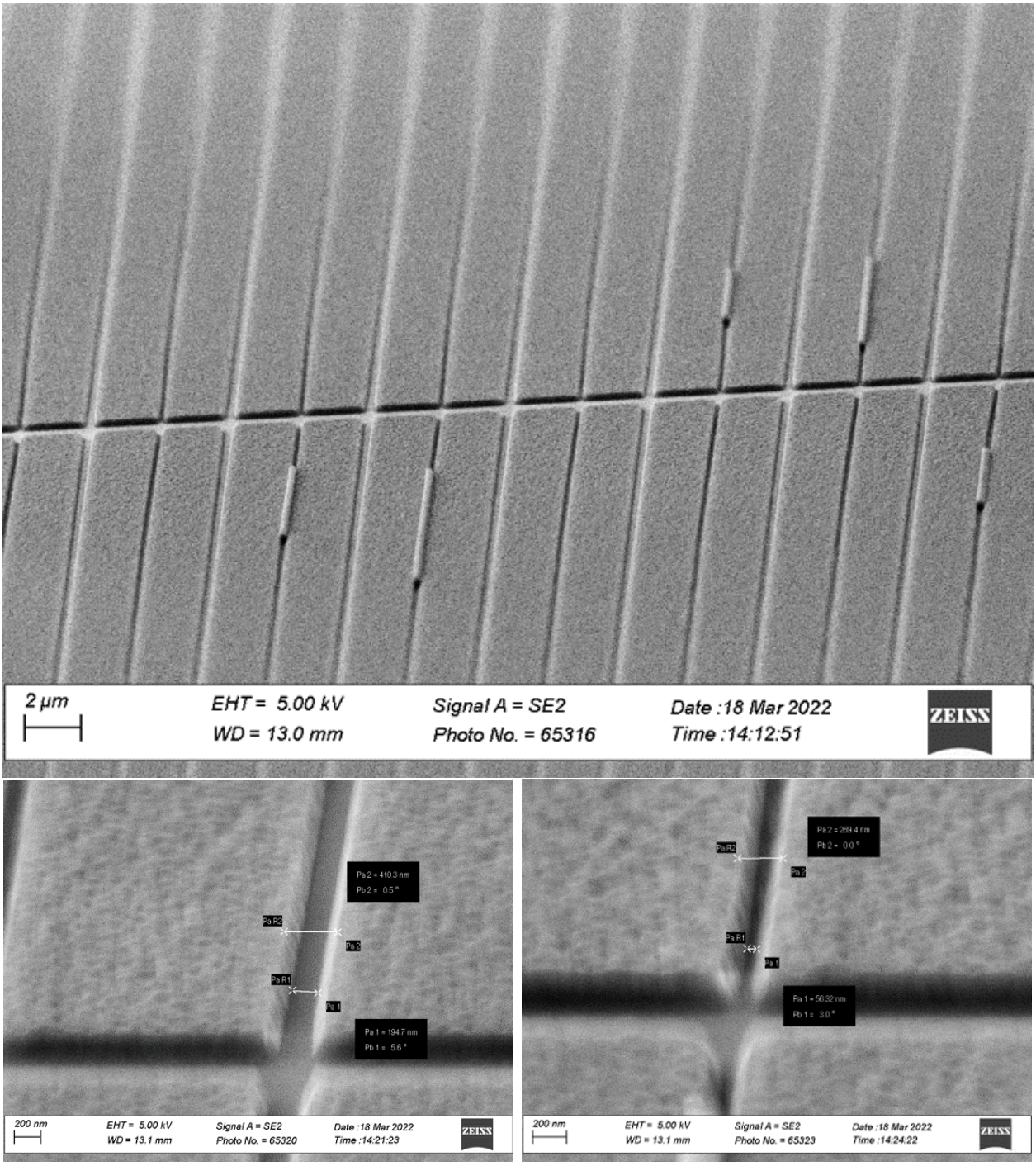

Figure A.3: SEM of Si bars produced via the HSQ/PMMA technique.

it. In either case, the *under-dosing* leads to an undesirable result.

On the other extreme, *over-dosing* occurs when the applied dose is much more than is necessary. At a surface level, a higher dose should not affect the resist as once it is dosed, it cannot be overdosed[2], it is either removed or staying there (depending on type of resist). However, the electrons do not stop when they hit the resist, they will scatter throughout the resist and substrate, creating secondary dosing interactions that dose the area being written and the area around it. As a result, the area around the pattern may get enough secondary dosing to also develop, broadening the features of the write and creating sloped side-walls in the resist. An example of the proper dose and of overdosing in PMMA can be seen in Figure A.4. The left figure has clear, nicely defined features whereas the right figure has a halo like feature surrounding the pattern. That "halo" is a result of the overdosing as the resist is being partially developed in those areas as the color variation comes from the thickness of the resist changing and the resultant thin-film interference effect.

There is a secondary effect present in the right figure that appears as small rectangles insides the pattern. The EBL writes the full pattern one small section at a time before moving to the next area. The rectangles are observed in Figure A.4 because the dose varies across each subsection, i.e. the resist thickness varies. This behavior is indicative of *charging* of the substrate/resist, which occurs when the electrons have not dissipated and create an electric field that deflects the incoming electron beam. With the beam being deflected, the dose across the subsection will vary. In the experiences of the author, reducing the electron beam current (i.e. increasing the time it takes to get to the appropriate dose), adds more time for the system to relax and the electrons redistribute.

A.5 Metal Evaporator

A metal evaporator allows for the deposition of thin films on a substrate in a controllable manner. The basic process is that the sample to be coated is placed in a vacuum chamber

[2]This is not quite true as some positive tone resists, such as PMMA, can actually become cross-linked at high enough dose, turning it into a negative-tone resist

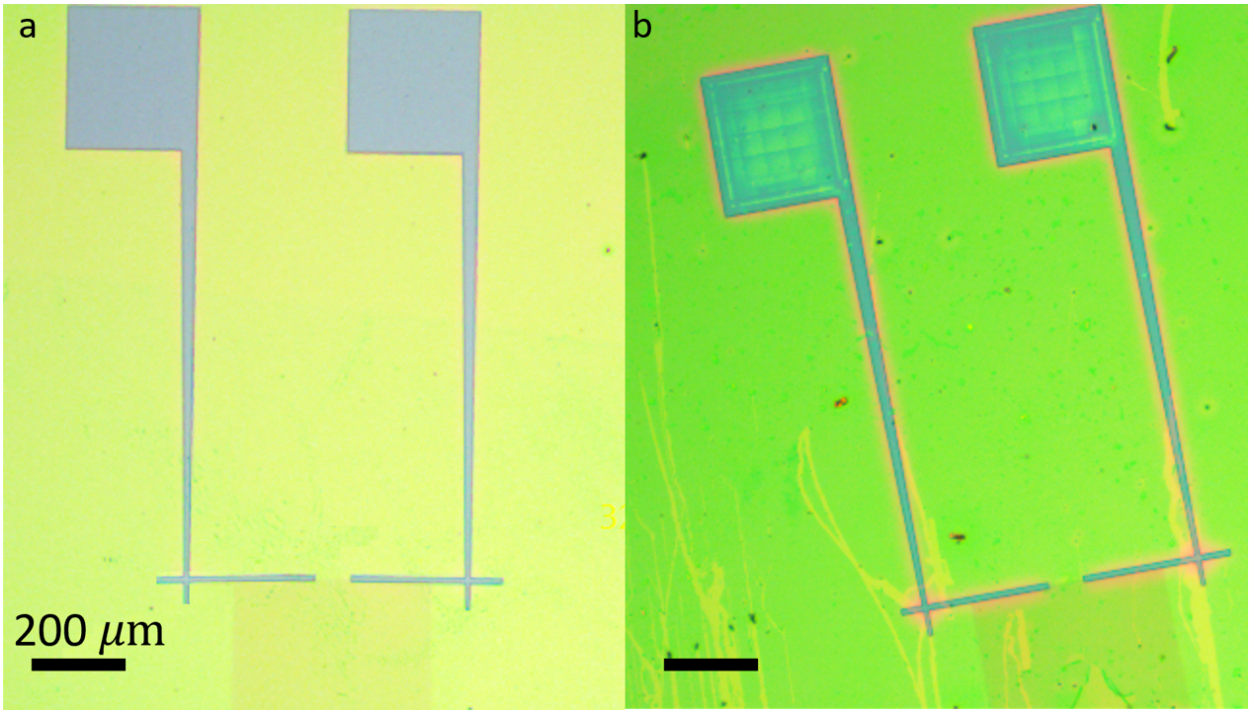

Figure A.4: Optical image of a PMMA resist after development. (a) Ideal behavior of the resist after development. (b) Non-ideal behavior, demonstrating both charging effects and overdosing.

along with the material source (solid pieces of the material). By heating up the source with a beam of electrons, a vapor of the material is released, depositing on the exposed surface of the substrate. By controlling the current, the vapor pressure, and therefore deposition rate, can be controlled.

A.5.1 Potential Issues

Gold, the most common deposition material in this work, has poor adhesion to generic substrates. To correct for this, a thin intermediary adhesion layer is deposited prior to the gold deposition. The adhesion layer used in this work was 2.5 nm of chromium.

A.6 Recipes

A.6.1 Using Bottom-Up Lithography and Optical Nonlocality to Create Short-Wave Infrared Plasmonic Resonances in Graphene

Nanoribbon and Nanoperforated Graphene Fabrication

The monolayer graphene-coated SiO2 substrates were placed in a 1-pyrenebutyric acid (PBA; 257354, SigmaAldrich) solution in THF for 24 h based on a previously developed procedure. A random copolymer (RCP) of glycidyl methacrylate (GMA), styrene (S), and methyl methacrylate (MMA), P(S-r-MMA-r-GMA), was synthesized as reported earlier. For this study, the RCP contained 62.5% S, 4% GMA, and balance PMMA (as confirmed by NMR) for lamellar forming BCPs. For cylindrical BCPs, the RCP contained 72% S, 4% GMA, and balance PMMA. The RCP was dissolved in toluene (320552, Sigma-Aldrich) and spin coated on the PBA-coated graphene/SiO2 substrate. These samples were annealed at 160 °C for 3 h under vacuum to cross-link the GMA unit and soaked in toluene for 15 min to remove any unreacted RCP. We used BCP P(S-b-MMA) with various molecular weights (MWs) all from Polymer Source, Inc., specifically 17k17k and 53k54k MWs for lamellar forming PS-b-PMMA and 21.5k10k MW for cylindrical forming PS-b-PMMA. These BCPs were prepared in toluene and spin coated onto the random copolymer covered samples. Films were thermally annealed under vacuum for BCP self assembly. Pattern transfer from the BCP to the underneath graphene was performed using a reactive ion etcher (PlasmaTherm 790) with oxygen plasma.[3]. Scanning electron microscope (SEM) images were taken with a Zeiss LEO 1550VP SEM for nanopatterned graphene visualization. Back-gated only NPG samples were fabricated with a slightly modified fabrication procedure described in detail in SI, section 4. Additional samples were prepared using these procedures that exhibited optical behavior similar to what was reported in the main text.

[3]The specific recipe was the PlasmaTherm Reactive Ion Etcher 50-10-10 (RF Power 50 W, Etch Pressure 10 mT, O_2 flow 10 SCCM) for 20-25 seconds

Fabrication of Gold Contacts

For the GNR-coated SiO2/Si substrates, they were first coated with a bilayer PMMA (950 A4 at 200 nm and 495 C2 at 300 nm). These samples were then exposed and patterned using the Elionix ELS G-100, an electron-beam lithography tool.[4] After exposure, the substrates were developed in a 3:1 IPA/DI water mixture for 20 s with a 10 s rinse of IPA. Metal deposition consisted of a 2.5 nm chromium adhesion layer and 80 nm of gold. After deposition, the PMMA was removed via a 15 h chloroform bath, a 1 h acetone bath, and then a 5 min IPA bath with a 5 s IPA rinse. The contacts for the GNRs were a gold-electrode mesh of interlocking branches that are 80 nm wide and spaced by 3 m. This pattern ensures reliable contact to the graphene nanoribbons in the "zen-garden" pattern without significantly reducing the optical signal or introducing additional resonances in the wavelength range of interest (26 m). For NPGs, the graphene remained a continuous sheet, so large gold contacts were applied via metal deposition through a mask

A.6.2 Graphioepitaxial Alignment of GNRs

Fabrication of Au/Si Bars

After the surface of the sample is prepared (graphene with neutral layer on top, identical to process for BCP alignment, just no BCP until *after* bars are deposited), the surface is then coated with PMMA (950 A4 at 200 nm) and baked at 180 C for 90 s. The samples were then exposed and patterned via the electron-beam lithography tool. Dimensions as described in Section 3.2. Dose ranged from 500-800 μC/cm^2. Developed in a 1:3 MIBK:IPA mixture for 90 s, with a 15 s IPA rinse and N2 dry. Next, the surface was descummed with a 10 s

[4]Pattern was split into two parts. First part was the thin (80 nm) wide bars that spread across the ribbons and the second part was large electrical pads to wirebond to. The first write for the thin bars used a beam current of 500 pA and an average dose of 600 μC/cm^2 (average as a proximity effect correction was used), 500 micron write fields with 100000 dots and feed/scan pitch of 2. This pattern also had larger bars coming off the edges to allow for the second pattern to contact without requiring precise alignment marks. Essentially, this process used the WeCAS software to place the two patterns such that they overlap and then they were written in sequence. Any error from stage-drift was accounted for by having the matching features be much larger than any shifts. The second write was of the electrical leads that were hundreds of microns in size. The write was done at 2 nA with a 600 μC/cm^2 dose, 1000 micron write fields with 100000 dots and feed/scan pitch of 4. The larger beam current was to reduce the time in the EBL as these features did not need to be precise.

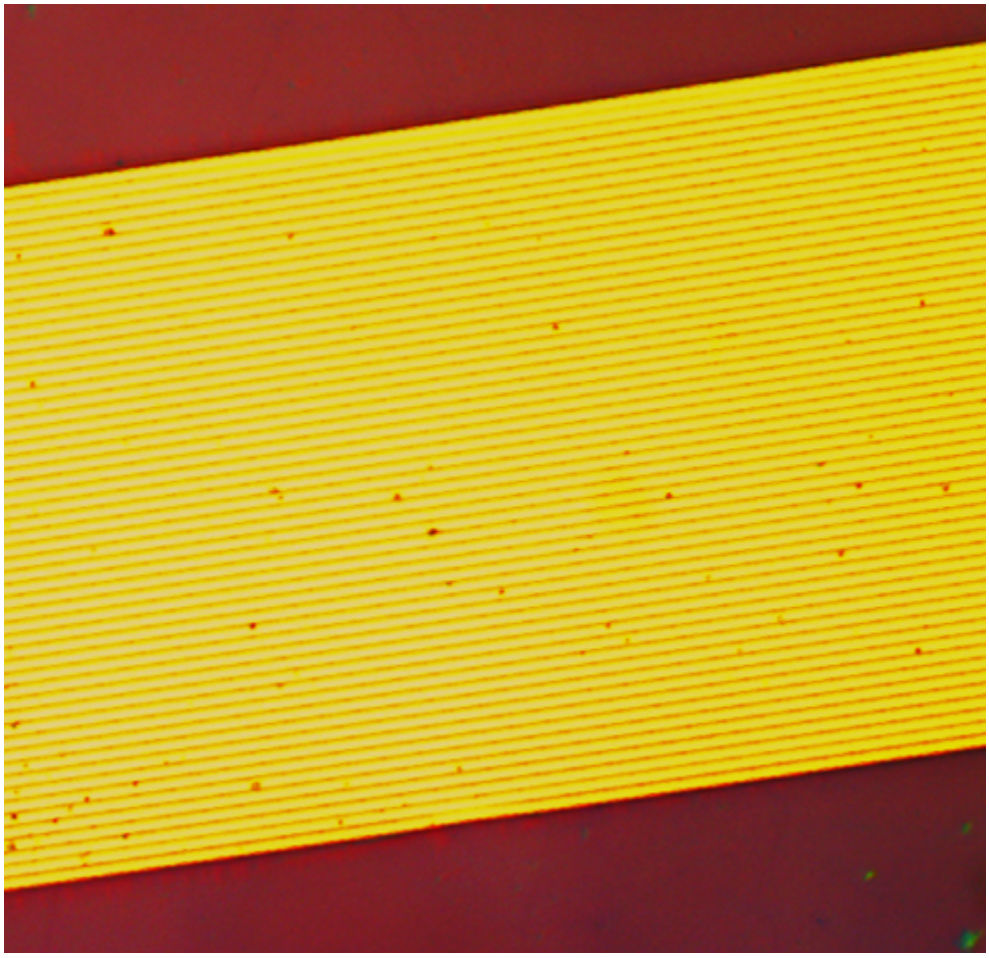

Figure A.5: Optical image of bars after lift-off process. Note that the gaps are difficult to make out relative to bars, but are present. Nearing resolution limit of the microscope.

50:10:10 RIE etch (same recipe as used to etch the GNRs). Deposition consisted of 2.5 nm of Cr, 30 nm of Au, 2.5 nm of Cr, then 50 nm of Si. 90 min lift-off in acetone at 40C with a 1 min sonication at 40% (low power) to assist in the removal of PMMA from the thin gaps with a final IPA rinse. Optical image of device can be seen in Figure A.5. BCP alignment then follows standard procedure after the bars are fabricated.

A.6.3 Dynamic Beam Steering of Thermal Emission by Graphene-Metal Metasurface

A.6.4 Fabrication of Device

2 μm thick, 5 mm x 5 mm SiN membranes on a 200 micron thick Si frame were purchased from

Norcada. Metal deposition of the back-reflector consisted of a 2.5 nm chromium adhesion layer and 100 nm of gold. Atomic Layer Deposition (a Fiji G2 ALD) was used to grow a 30 nm film of Al_2O_3 on the top of the SiN membrane. Once the Al_2O_3 was grown, a prepared graphene sheet was transferred on top of the Al_2O_3 film. Graphene was purchased from Grolltex and was grown on a Cu foil. To remove the foil, first a protective layer of PMMA (950k, A4, MicroChem Corp.) was added on top of the graphene. The Cu foil was etched away with $FeCl_3$ (CE-100, Transene) then the graphene/PMMA stack was rinsed in a series of deionized water baths until transfer to the prepared membranes. Once transferred, the PMMA was removed by soaking in 60^oC acetone for 1 h. After the graphene transfer, a 5 nm film of HfO_2 was grown via atomic layer deposition. To prepare the SiN membranes for the next steps, the Si frame of the sample was glued to a carrier Si chip with PMMA (950k, A8, MicroChem Corp.). The prepared substrate was then coated with a negative tone hydrogen silesquioxane resist (HSiQ, 6%, DisChem Inc.) at 100 nm. The sample was then exposed and patterned using the Elionix ELS G-100, an electron beam lithography tool.[5] After exposure, the samples were developed in MF-321 for 90 s, with a 30 s rinse in DI water and then a 30 s rinse in IPA. For metal deposition of the top, a metal mask was placed above the substrate to create electrically disconnected regions. The deposition consisted of a 2.5 nm chromimum adhesion layer and 30 nm of gold.

[5]1000 micron write field, beam current 500 nA, dose 1000-1800 $\mu C/cm^2$, scan/feed pitch of 1. HSQ spun on at 100 nm nominally develops at 1000 $\mu C/cm^2$, however smaller features require larger doses. For creating 40 nm features, a dose of 1500 was used. Smaller features required larger doses. The resist does have a time component with its behavior, so these doses may shift as it ages. When HSQ ages, it becomes a more sensitive resist and the sidewalls will likely no longer be straight. If this occurs, new HSQ is required.

Appendix B: Supporting Information of: Self-Stabilizing Laser Sails Based on Optical Metasurfaces

B.1 Description of Local Forces on Sail

[1]

As discussed in the main text, the reflection/refraction of light will impart optical forces on the surface. The local lateral and normal forces are shown below in Equations B.1 and B.2.

$$F_x = \frac{P_i}{c}[\vec{R}\sin(\phi - 2\theta) + \vec{T}\sin(\pi - \phi)] \tag{B.1}$$

$$F_z = -\frac{P_i}{c}[1 + \vec{R}\cos(\phi - 2\theta) + \vec{T}\cos(\pi - \phi)] \tag{B.2}$$

where F_x is the lateral, tangential force, F_z is the normal force, $\vec{R}$ and $\vec{T}$ are the reflected and transmitted optical rays, respectively, P_i is the incident power, θ is the structure's rotation relative to normal, ϕ is the angle of deflection relative to surface normal, and c is the speed of light in vacuum. This analysis applies to scenarios where the reflected and transmitted phase gradients are identical, while in actual metasurfaces this assumption may not be true and will result in modification of the above equations.

In Figure B.1, we show a visual representation of the motion the ICE sail can undergo (lateral offsets and rotations) and how these changes alter the lateral forces and torques on the sail. When the sail is offset, the right side of the sail is in a more intense region

[1] This section is a reproduction of an already published work found in [1]. The text and figures are unaltered, except for formatting changes.

of the beam, so the lateral forces on the right side of the sail (restoring forces) increase in magnitude. Simultaneously, the left side of the sail is shifted to a region of lower beam intensity, creating weaker lateral forces on the left side of the sail (non-restoring). We note that while the magnitudes changes, the direction of the force vectors remain constants. The lateral motion also leads to a torque on the sail created by the left(right) side of the highly reflective center region moving to an area of higher(lower) beam intensity. When the sail is rotated (far right in B.1), the angle of reflection for each point on the sail changes by 2θ which causes a change in the magnitude and direction of the local force vectors, as detailed in equations B.1 and B.2. Note that the inner, highly reflective, region reflects light normal to the surface, so lateral forces in this region are only be present when the sail is rotated about the x or y axes, not when the sail is laterally shifted.

B.2 Accuracy of leapfrog integration technique

In order to verify the accuracy of our leapfrog integration technique, we compared the approximation with the exact result of the coupled oscillator system; an example is shown in Figure B.2. We can see that there is a high degree of agreement between the two methods, and this agreement holds for indefinite time scales (the 5 second time scale was chosen to highlight the agreement).

B.3 'V'-type sail motion

As described in the main text, the 'V'-type sail reflects light at two constant angles that are equal and opposite on the left and right sides of the sail. The motion of two such sails are illustrated in Figure B.3 for 3° deflection angles with 95% or 65% reflection efficiency. As we can see, both sails attempt to correct for the lateral offset by moving towards the center of the beam, but they are simultaneously rotating and eventually pushed out of the beam. The difference in behaviors can be attributed to the difference in reflection coefficients: 'V'-type Sail A is 95% reflective and 'V'-type Sail B is 65%. The reduction in reflection coefficient

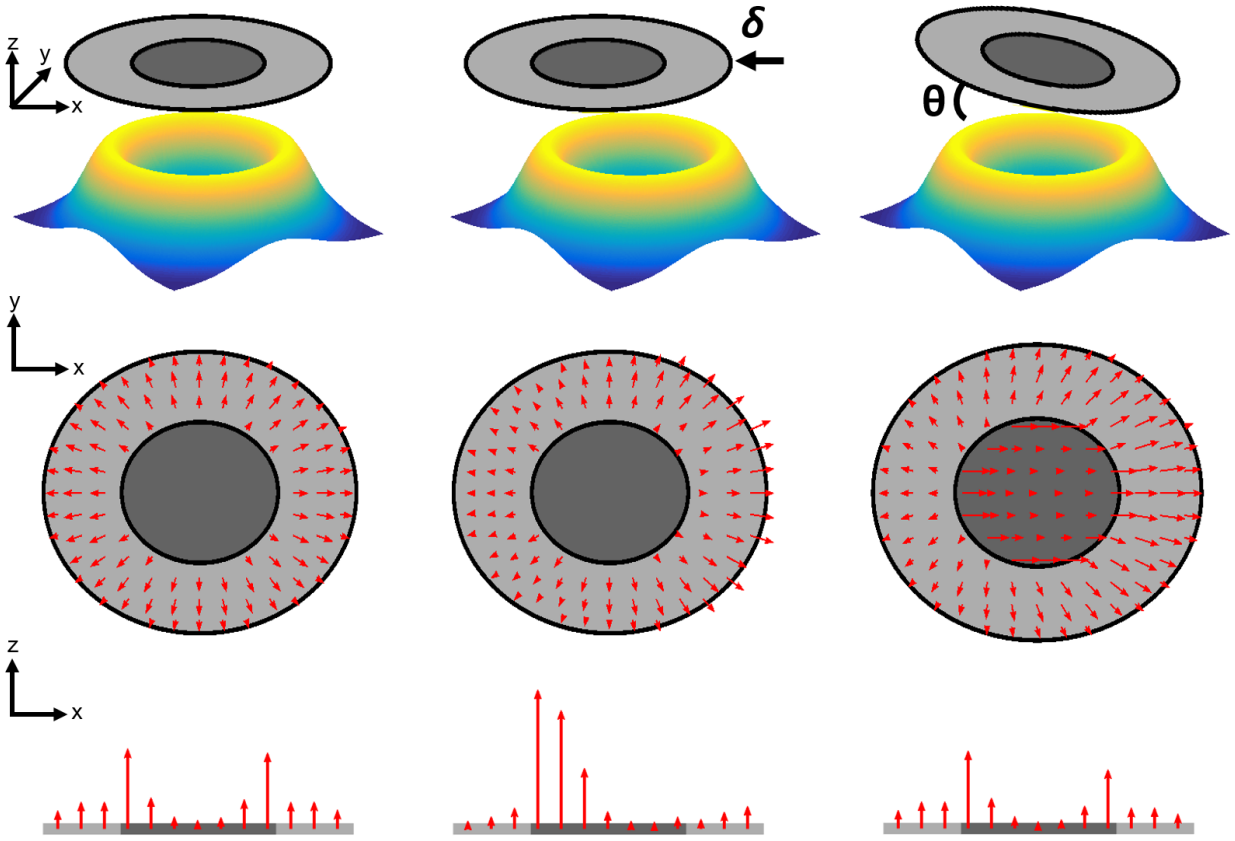

Figure B.1: 3D representation of the ICE sail with an annular drive beam where the sail is centered in the beam (upper left), offset by δ (upper center), and rotated by θ (upper right). Lateral optical forces of the sail when it is centered in the beam (middle left), offset by δ (middle center), and rotated by θ (middle right). Normal optical forces of the sail when it is centered in the beam (lower left), offset by δ (lower center), and rotated by θ (lower right).

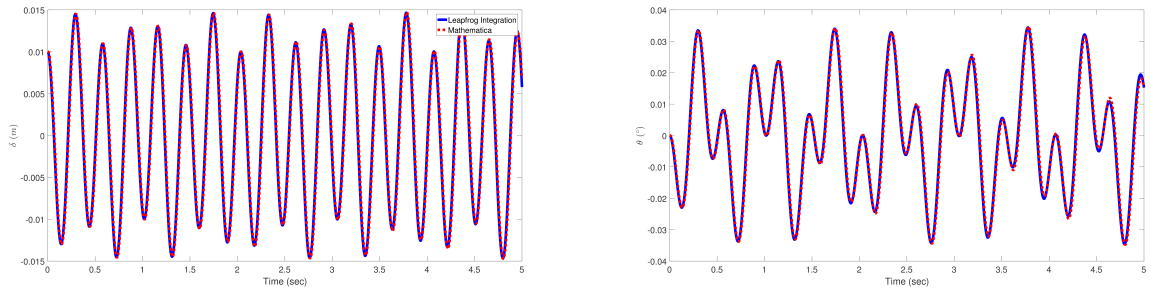

Figure B.2: Motion (left) and rotation (right) for a single sail calculated using Leapfrog Integration technique and the exact solution derived from Mathematica.

leads to weaker torques, which makes the sail rotate more slowly, allowing for 'V'-type Sail B to remain stable for slightly longer.

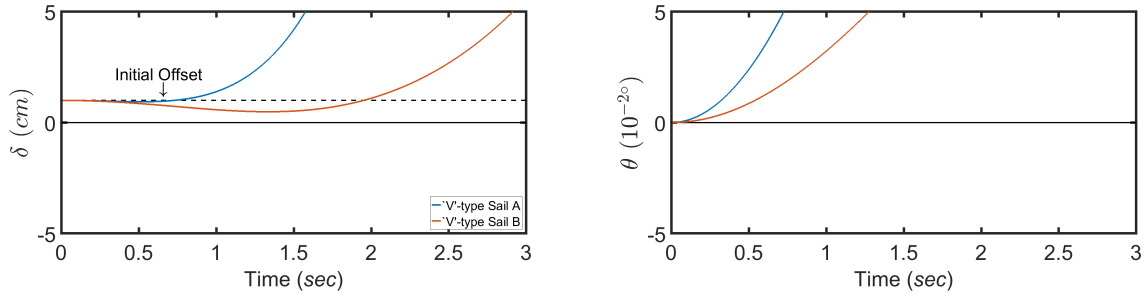

Figure B.3: Plots of the displacement (left) and rotation (right) for two different 'V'-type sails. Each sail is four meters wide with an initial offset of 1 cm. The incident beam power is 100GW. For both sails, the incident beam is a Gaussian with a 4 meter FWHM. 'V'-type sail A was a 95% reflective structure with a 3° deflection. 'V'-type sail B was a 65% reflective structure with a 3° deflection.

B.4 Constants for ICE Sail

Figure B.4 shows an example of the first-order dynamical force constants on an ICE sail with $R_{out} = 0.15$ and D_{in}= 2 m (see Figure 3d in main text). C_1 and C_3 vary most significantly as the beam parameters shift, at least an order of magnitude shift greater than either C_2 or C_4. The magnitude of C_4 is the least dependent on the incident beam, demonstrating that the optical torques are least affected by rotations. This can be understood by considering that for small rotations, the force normal to the surface is relatively unchanged, and this force dominates the torque. In contrast, the lateral force can change more significantly as the sail is rotated, which we can see by the relative increase in magnitude of C_2.

We also note that there is a region of maximum magnitude intensity near beam separations of 2 m and FWHM of less than 1 meter for the offset dependent coefficients ($C_{1,3}$). This occurs because the majority of the beam power is concentrated on the border between inner and outer regions; a small offset will lead to a comparatively large change in the optical forces. As the beam width increases, this effect is lessened as there is no longer the same concentration of light.

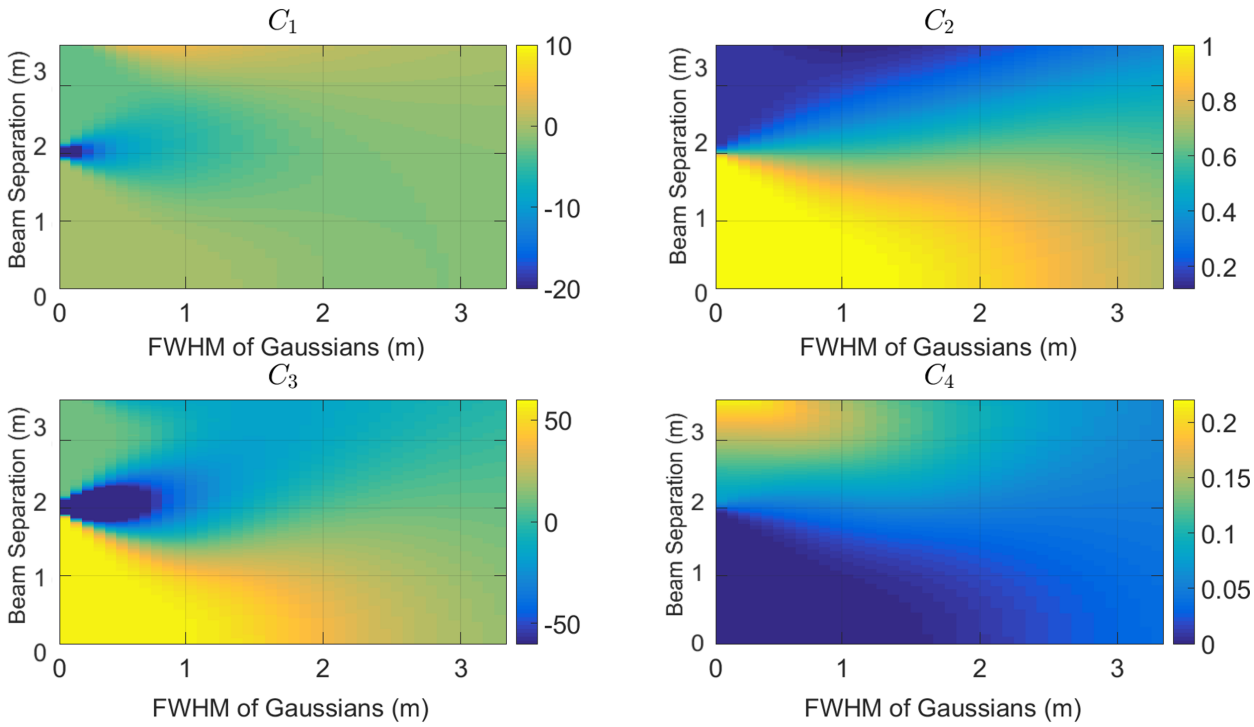

Figure B.4: First order dynamical force constants C_1, C_2, C_3, and C_4 for an ICE-sail ($R_{out} = 0.15$ and $D_{in} = 2$ m) in a double Gaussian beam with continuously varying diameter and beam width.

B.5 Expanded Stability Analysis

Increasing R_{in}

In the main text, the stability analysis was restricted to a maximum $R_{out} = 0.3$, but in Figure B.5, we show that same analysis for $R_{out} = 0.5$. As we can see, the increase in reflectivity leads to a decrease in stable and marginally stable regions when compared to Figure 3 in the main text. When the outer region of the sail has higher reflectivity ($R_{out} = 50\%$), two stable regions form.

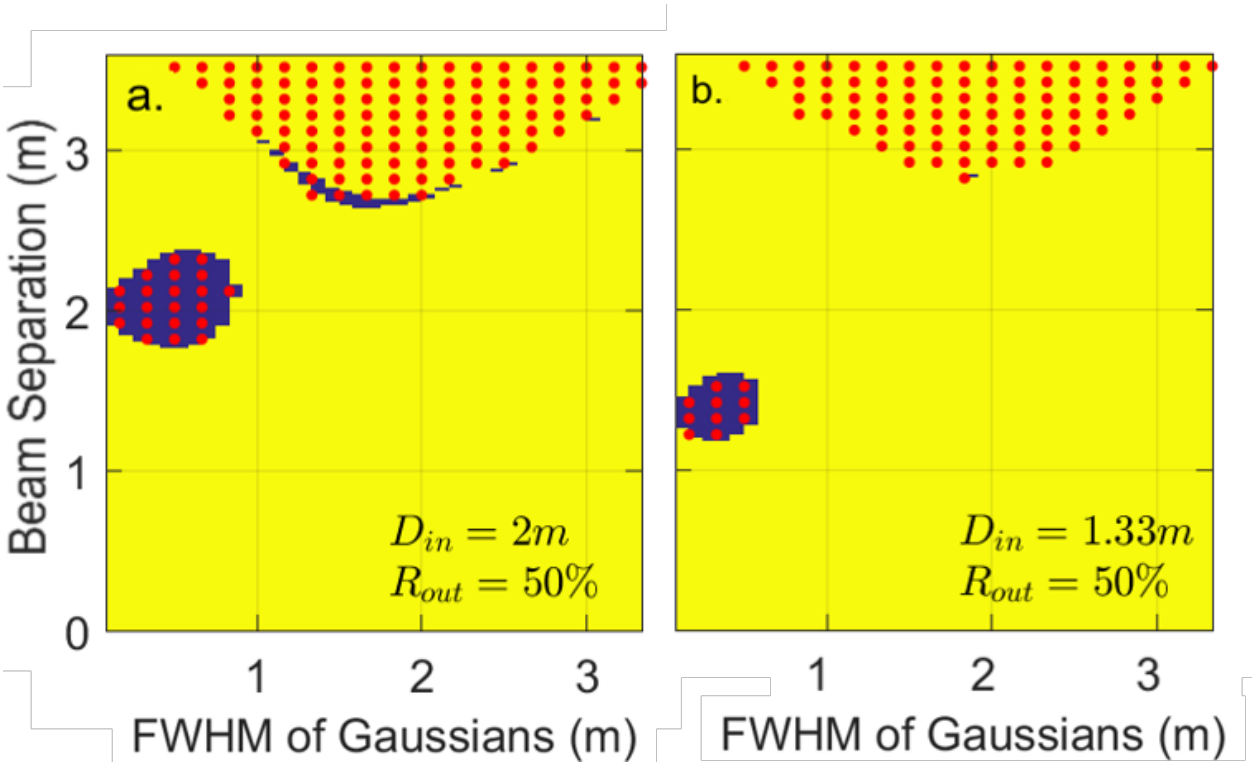

Figure B.5: Analysis of stability for 2 ICE-sail configurations driven by double-Gaussian beams with varying beam separation and FWHM for an initial offset of 1cm, 50% of the maximum allowable offset for stability. Yellow (purple) regions indicate sails configurations that are unstable (stable). The dotted red areas indicate sail configurations that satisfy the $C_1C_4 + C_2C_3 < 0$ condition. (a,b), are ICE sails with $R_{out} = 0.5$ and $D_{in} = 2$ m, 1.33m, respectively. The motion was simulated over a 60 second period.

Payload Positioning

The analysis in the main text considered the effects of beam shaping and the reflection/-transmission profile of the sail, but there is one additional parameter we wish to consider: the placement of a payload, which we assume to be 5 g with a controllable mass distribution. In order to protect the payload from laser heating and prevent it from affecting the dynamical force coefficients, the payload must be placed behind the highly reflective region of the sail, but it can be arranged to optimize the moment of inertia, I_s, for stability. We model two extreme scenarios, first where the payload is placed in the center of the sail which leads to a negligible change in I_s, and second with the payload distributed on the outer edge of the reflective region, which increases I_s by $\sim 29\%$; in both cases we consider sails with a 2 m inner reflective region, and an outer region with R_{out}=0.3. The motion of these modified sails is then simulated and tested for stability as described in the main text, with initial offsets of 1 cm and 5 minute simulation times. The results of those simulations are shown in Figure B.6, which shows that in both scenarios the margins of stability are decreased as compared to designs that do not include the payload (found in main text Fig. 3a). However, a radially distributed payload clearly shows larger regions of stability than a payload concentrated in the center. We note that while the payload has no effect on the dynamical force coefficients ($C_{1,2,3,4}$), it does effect the characteristic lateral and angular oscillation times of the sail, which modifies the overall stability. For desirable payload geometries, such changes can be compensated both by changing the reflected/refracted angle of the outer region, and by changing the reflection efficiency of the outer region.

B.6 Noise Simulations [49]

To model the noise on the beam, we introduced time dependent noise; a new perturbation was included every ms of the simulations. We used the following equation to determine the noise on the system after n time steps.

$$r_n = f^n g_0 + \sqrt{(}1 - f^2) \sum_{i=1}^{n} g_i f^{n-i} \tag{B.3}$$

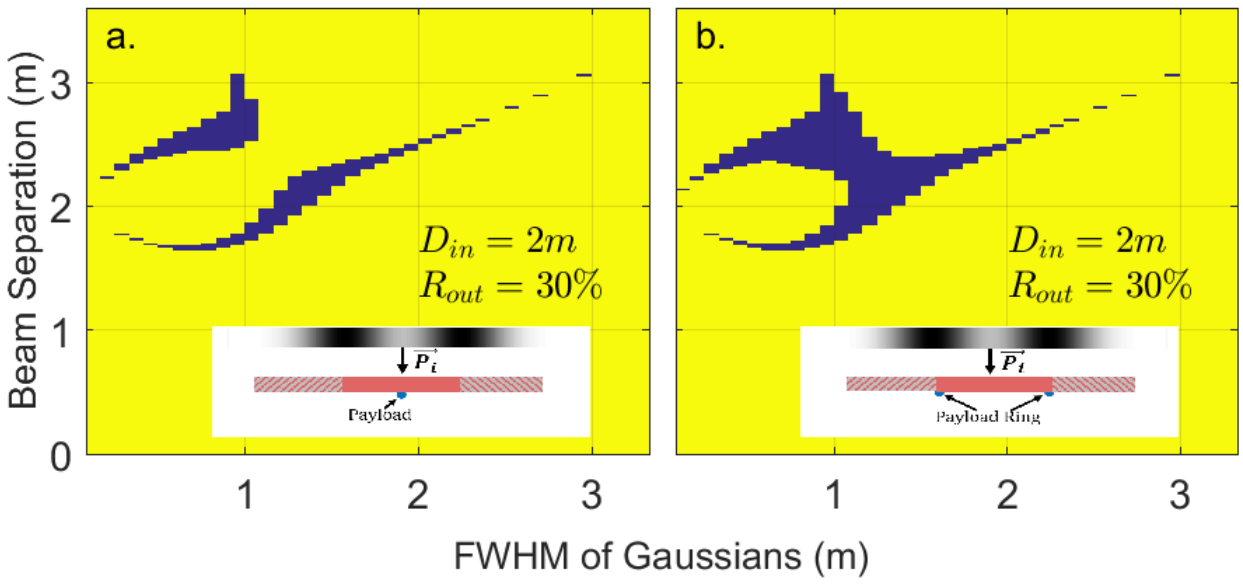

Figure B.6: Analysis of stability of a single ICE sail configuration with a 5g payload included at different positions behind the reflective region of the sail. The ICE sail has $R_{out} = 0.3$ and $D_{in} = 2$m. Yellow (purple) regions indicate configurations that are unstable (stable) when offset by 1 cm. Insets indicate the payload position on the underside of the sail.

where r_n is collective noise at the nth step, f is the decay function, and g_i is the noise introduced at the ith step. Figure B.7 shows example of distortions of the beam for one time step with the undistorted beam in blue, the magnitude distortions in red, and the distorted beam in yellow. The length-scale of the noise was chosen to be 10 cm. Figure B.8 shows the stability analysis over various magnitudes of noise (0.1, 0.15, 0.2, 0.3, and 5%) for a single noise profile. By the time the noise is increased to 5%, no sails can remain stable. In the main text, 100 randomly generated noise profiles were used with an average noise value of 0.12%.

B.7 3D Model Comparison

By expanding the analytic methods used in the main text, we can calculate the coefficients of a 3D, cylindrically symmetric sail. The incident beam is an annular beam, as shown in Figure B.9. The cross section at the center of the sail (red line in Figure B.9) is a double Gaussian, which is what we used in the 2D model in the main text. However, if we take a cross-section further to the top (black line in Figure B.9), the cross section is a Gaussian

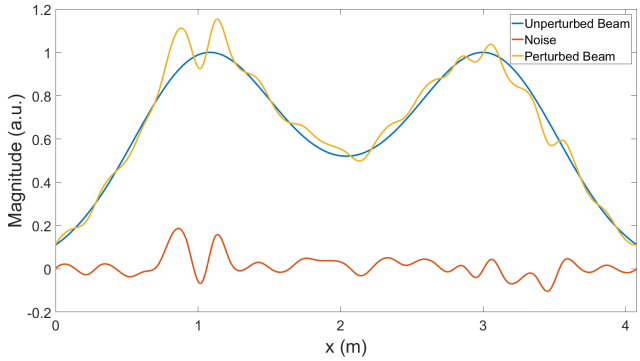

Figure B.7: Example of the noise introduced to the beam.

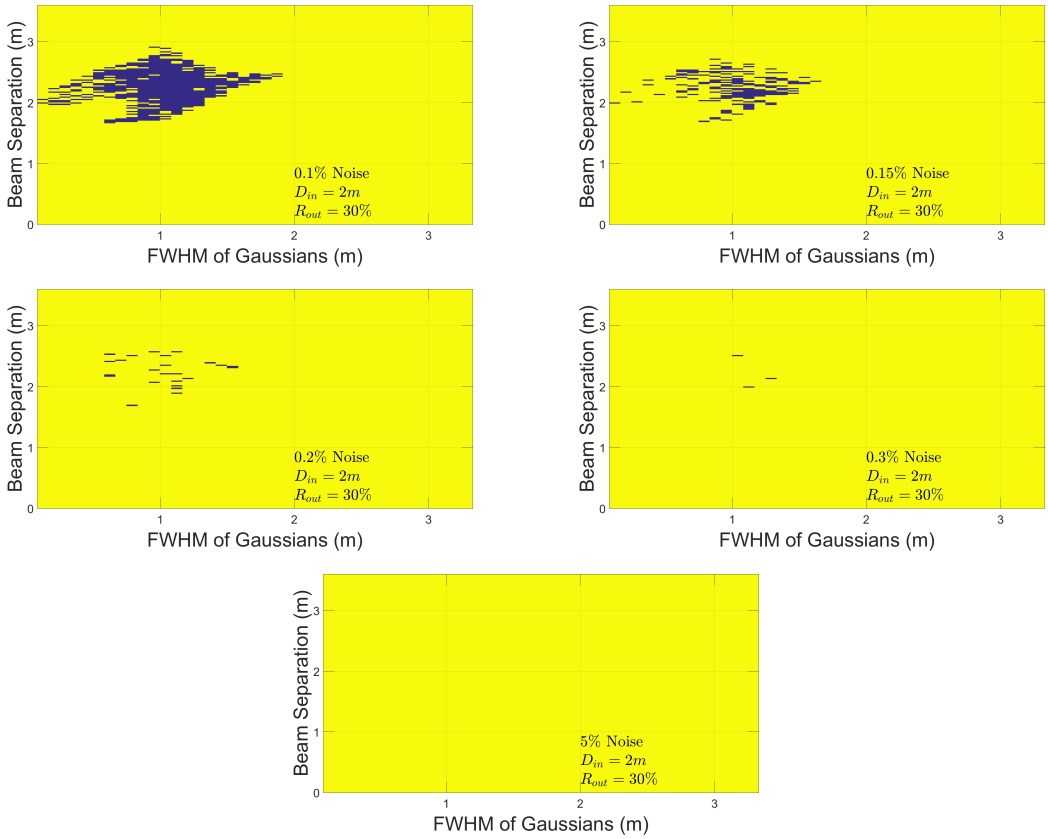

Figure B.8: Stability analysis for noise of various magnitudes ranging from 0.1% to 5%. Yellow (purple) regions indicated sail configurations that are unstable (stable). The motion was simulated over a 5 minute period.

beam. Our 2D model assumes that the cross section does not change, but we can see that is not accurate for a 3D model. We would also like to note that due to the cylindric symmetry, the force in the x or y directions will be dependent not only on the radial position, but also the azimuthal angle. We compare the coefficients derived from the 3D model to the 2D model in Figure B.10 for an ICE sail with $R_{out} = 0.3$ and $D_{in} = 2$ m. We note that for the majority of beam combinations, the 3D model has coefficients with similar magnitudes to the 2D model, albeit with reduced magnitudes. This is a result of the azimuthal dependence of the lateral forces and the beam cross sections varying as we calculate the optical forces across the sail.

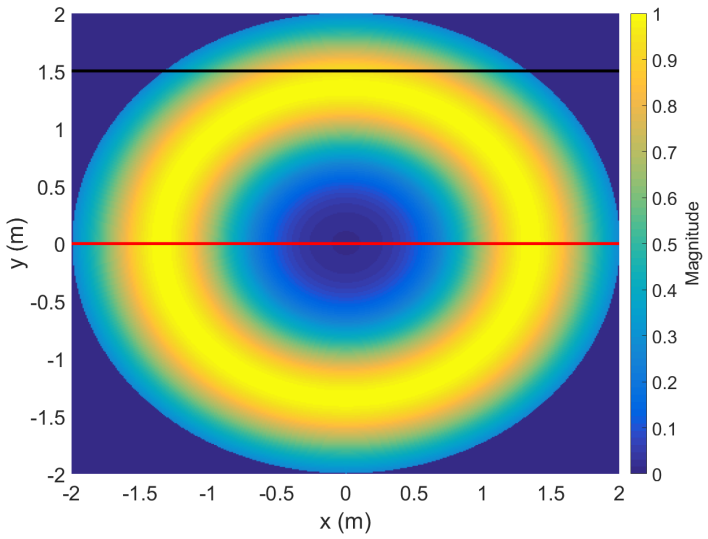

Figure B.9: Visualization of input beam magnitudes on sail.

B.8 Simulation Methods

The phases/magnitude in Figure 4 of the main text were extracted using Lumerical FDTD where we used periodic boundary conditions along the x- and y- direction. To extract the reflected/transmitted phase, we placed a point monitor above/below the surface (where "above" means the positive z-direction). To extract the reflection/transmission, we placed a transmission monitor above/below the surface. To generate the lines shown in Figures 4b-4d

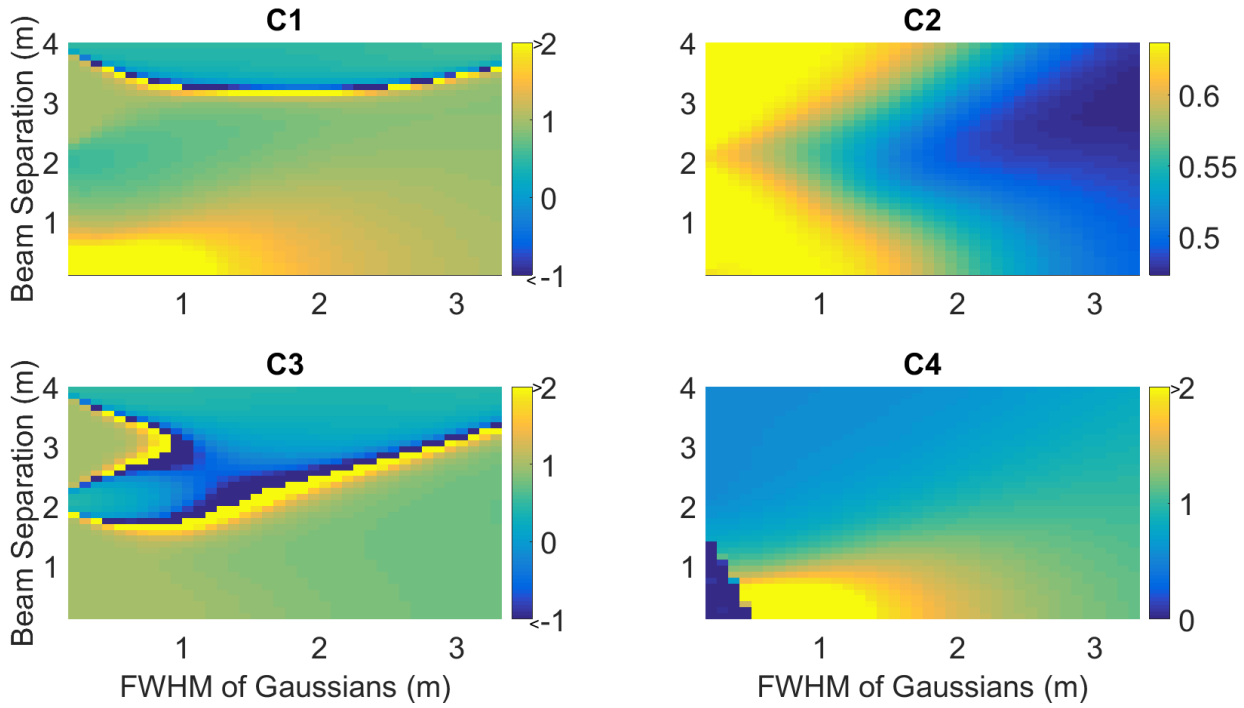

Figure B.10: Ratio of 3D to 2D Dynamic Force Coefficients.

(main text), we picked points to ensure that the lines had a consistent reflection (i.e. 95% or 30%) while maintaining a 2π phase coverage.

To arrange the resonators on the surface, we used the generalized Snell's law. We wanted a particular reflection angle at each part on the sail, and we knew the resonators had to be 1.2 μm apart. Thus, we knew what reflection phase we needed at each point on the sail. Then, we picked the resonator with the desired phases and placed it in the correct position. The phases of our resonators and desired are shown in Figure B.11. We find that the reflected phases match with our desired behavior as they can cover 2π. However, the transmitted phases can only cover π, so there are portions where the phase is parallel to the ideal, but is offset. The angle of reflection/diffraction is determined by the slope of the phase gradient, so this offset to the ideal does not change the transmitted behavior per se, however, it does introduce a phase mismatch at the boundary of these resonators, which can lead to anomalous forces/behaviors.

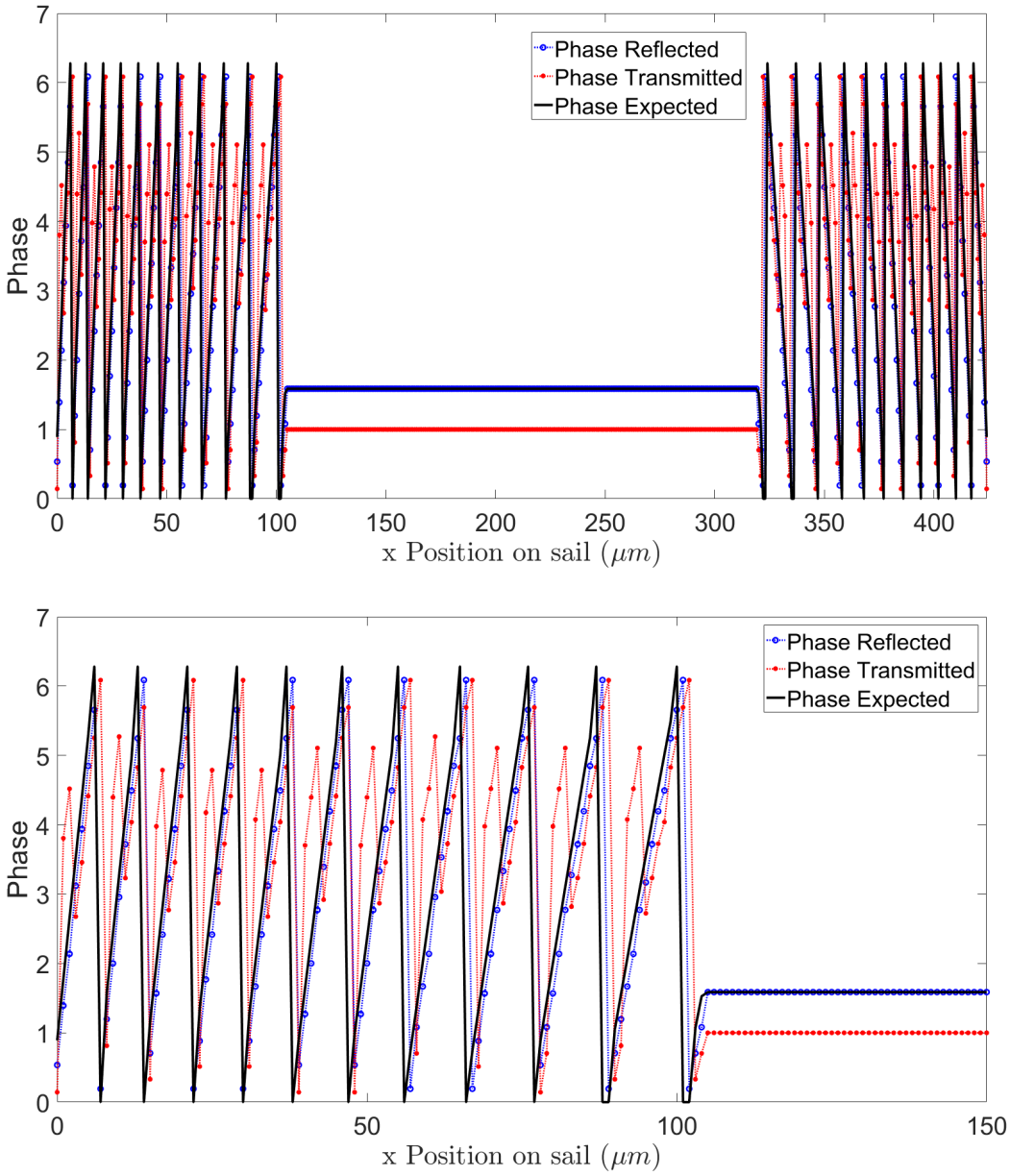

Figure B.11: Phase of the reflected and transmitted light from the chosen resonators compared to the ideal phase at each resonator to produce the desired phase profile for the ICE sail simulated in the main text. The upper figure shows the phases for the entire sail, while the lower figure shows a zoomed-in portion of the sail to highlight the transmission discontinuities.

B.9 Optical Force Abnormalities

We have identified three causes for the local forces fluctuations that can, in some cases, change the direction of the lateral force from the expected behavior. These fluctuations can be caused by the presence of a metasurface edge as shown in Fig. B.12(a), where light diffracts off the edge. This diffraction causes additional scattering of light from the expected behavior. In Figure B.12(b), there are 'phase slips' in the metasurface, which can be seen in positions 100 and 110 μm where the lateral force changes sign in that area. The last case is caused by inter-resonator interactions as seen in Fig. B.12(c). The last case is the most challenging to eliminate because it cannot be predicted by an analysis of individual resonators, or from the phase profile of the reflected/transmitted wave: although this surface produces the desired far-field profile, the lateral optical forces on individual resonators show variability, and even changes in direction.

The correlation between inter-resonator coupling and anomalous local forces can be established by analyzing the far-field scattering cross section (SCS) for each pair of neighbor resonators as demonstrated in Figure B.13 (left). The net lateral force on this resonator pair can be calculated by integrating the scattered light that goes in the left and right directions. As shown in Figure B.13 (right), the anomalous force fluctuation is associated with the region where scattering by neighboring pairs of resonators changes its symmetry in right-left direction. This leads to an interference between differently directed scattered waves, which causes force fluctuation. We also observed the same effect for an array with different inter-resonator distances (but same resonator sizes) in order to confirm that the effect originates from the local scattering pattern of resonators and not by the array properties (Fig. B.13 (right)). These effects are compounded further by next-nearest neighbor interactions and, in general, controlling the local forces is a difficult problem to solve through intuition.

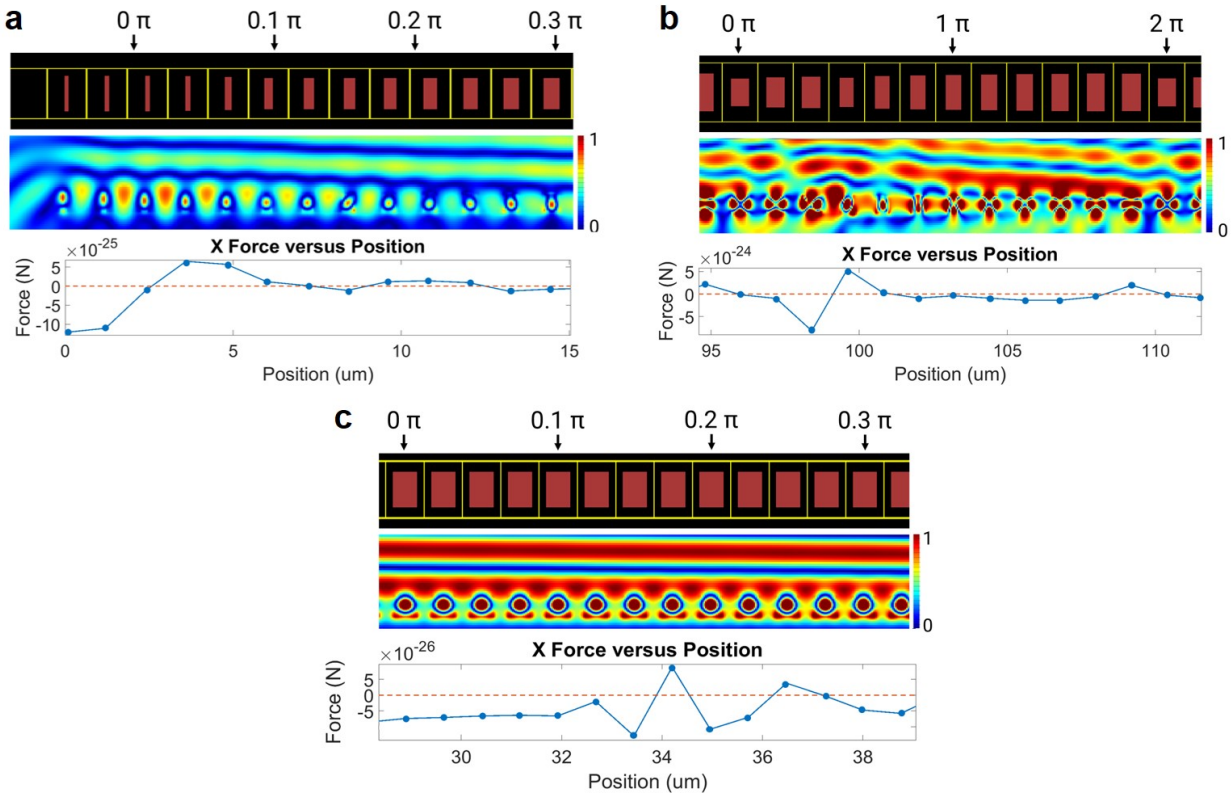

Figure B.12: **a** (Top to bottom) Cross-section of the 3D Si-resonator phased array, field profile, and optical forces at individual resonators for the edge region of the 1 degree-steering reflecting metasurface. **b** Same as in **a**, for the central region of the 2 degree-steering transmitting metasurface with phase slips and 30% reflectivity. **c** Same as in **a**, for the central region of the 1 degree-steering reflecting metasurface with continuous phase and (seemingly) near-field profiles but exhibiting the force fluctuation.

Figure B.13: (left) Scattered field intensity in far-field domain for a pair of resonators. (right) Lateral optical forces on individual resonators in a 1D beam-steering array (blue), and the ratio of [SCS to the right]/[SCS to the left] for each corresponding pair of neighbor resonators (red), both as a function of the resonator index in the array. Note that the ratio of light scattering to the right/left abruptly changes at the position of resonators that also show anomalous forces.

B.10 Extracting Dynamic Force Coefficients

In order to extract the dynamical force coefficient from our simulations, it is necessary to calculate the local and net optical forces as the metaurface sail is shifted and tilted within the beam, and then perform linear fits to the position/tilt vs. force/torque dependencies. In Figure B.14, we show the coefficient extraction for a 3°, 95% reflective 'V'-type sail. This sail's motion was simulated in Figure B.3, 'V'-type sail A. Shifted simulations were performed over lateral and rotational steps of 5 μm and 0.25°. We found that the force/torque showed a linear dependence on offset/rotation angle over ranges of 40 μm and 3°. First order fits were then used to determine the effective dynamical force coefficients, $C_{1,2,3,4}$. We can see that there is good agreement between our analytic models and the simulated sails. We summarize the analytic and full-wave extractions in Table B.1. We note that the simulated 'V'-type sail is a less complex metasurface than the ICE sail, so there are fewer force abnormalities to cause disagreement between our analytic model and full-wave models.

To extract the coefficients used in the main text, we performed a similar analysis to the ICE sail. Shifted simulations were performed over lateral and rotational steps of 20 μm and

'V' Sail	C_1 $(\frac{N}{Wm})$	C_2 $(\frac{N}{Wdeg})$	C_3 $(\frac{N}{W})$	C_4 $(\frac{Nm}{Wdeg})$
Analytic	-2.02E-6	2.25E-10	7.95E-9	1.22E-15
Full-wave	-1.21E-6	2.15E-10	6.76E-9	5.89E-15

Table B.1: Dynamic Force Coefficients of a 'V'-type sail.

1°, respectively. The larger step sizes are due to the increased computational time required for these more complex ICE sails in comparison to the 'V'-type sails. We found that the force/torque showed a linear dependence on offset/rotation angle over ranges of 20 μm and up to 3°. We note that the analytic model and full-wave models are consistent up to 40 μm offsets, but that behavior is non-linear for the torque beyond 20 μm.

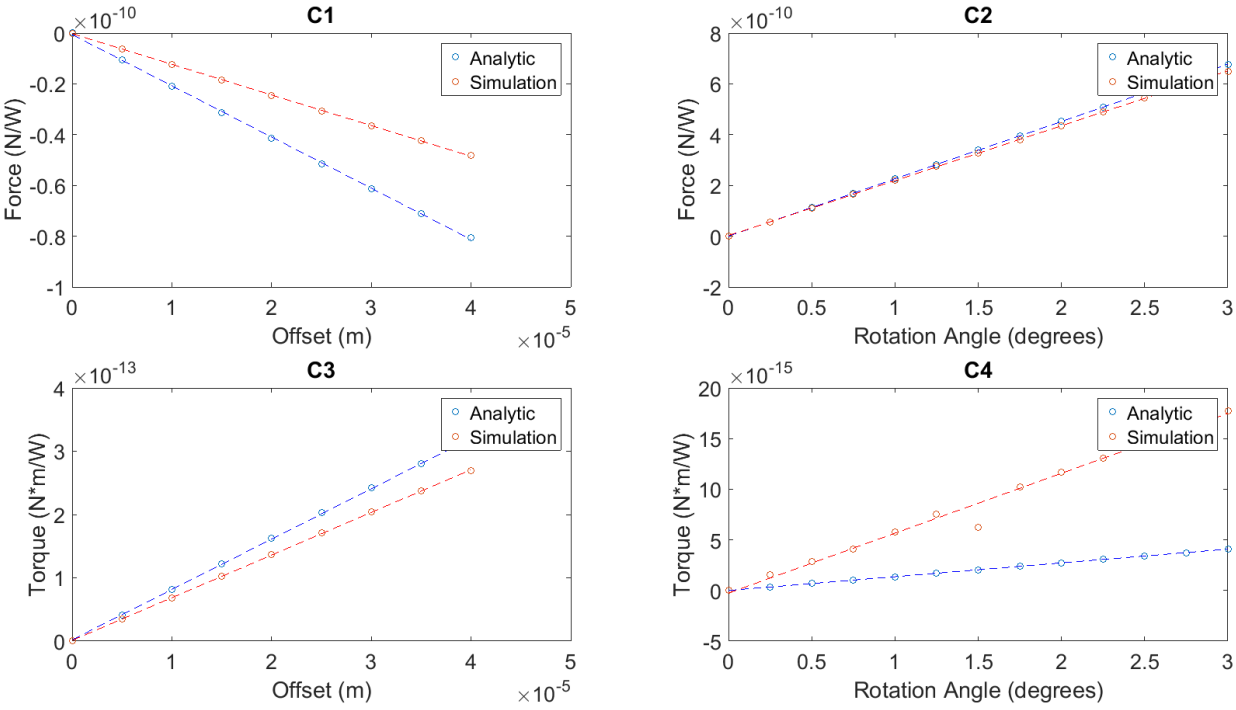

Figure B.14: Extracting the Dynamic Force Coefficients for the 3 Degree 'V' Sail

B.11 Scaling Laws

Due to computational limitations, we are unable to simulate a 4 meter wide sail, but we can derive a basic set of scaling laws that allow us to approximate the dynamic force coefficients

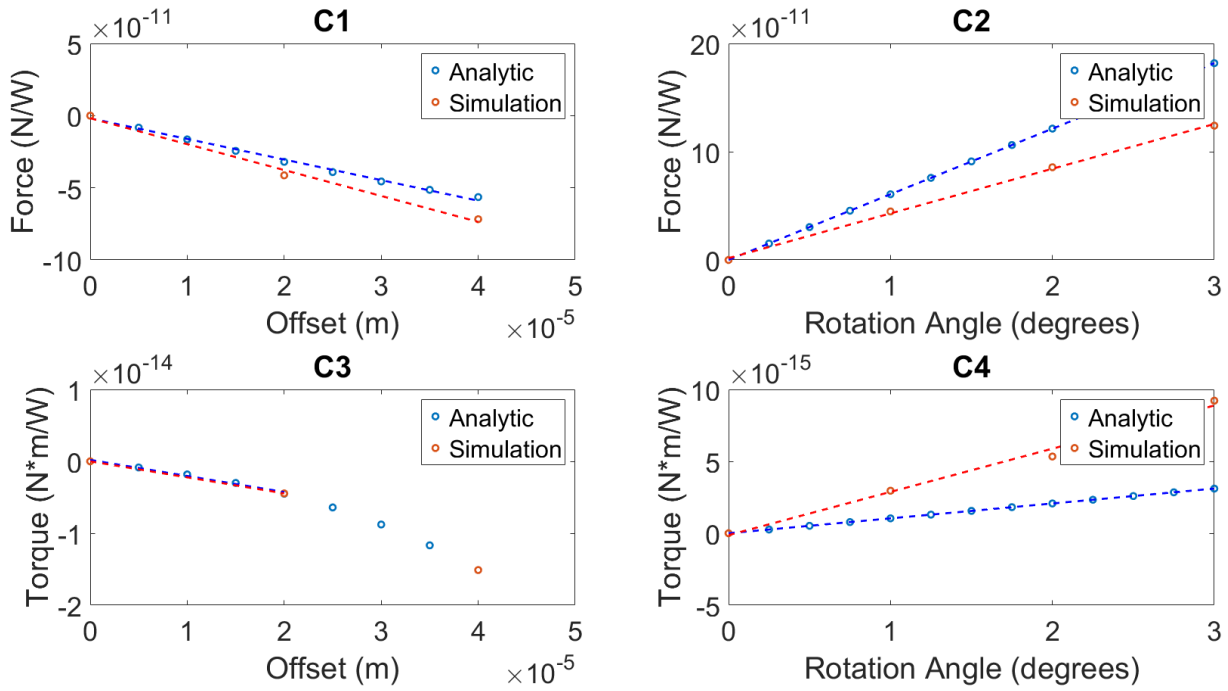

Figure B.15: Extracting the Dynamic Force Coefficients for the 5 Degree 'ICE' Sail

for the 4 meter sail from a much smaller (but proportional) sail. The constant C_1 is derived from the lateral restoring force when the sail is offset. If the sail size is increased by a factor S, the sail needs to move S times as far to get the same lateral response as the original sail; C_1 will decrease by a factor S. We note that the scaling of the sail will not affect the reflection/transmission when rotated, so C_2 should remain unchanged. However, by increasing the size of the sail, each element of the sail is now a factor of S further from the center of the sail, which will influence the torques. C_3, the torque dependence on offset, will remain unchanged as a result. In contrast, C_4, the torque dependence on rotation, should increase by a factor S as the force dependence on rotation is unchanged, but the distance from the center is increased by a factor of S. This is summarized in Table B.2.

Original	C_1	C_2	C_3	C_4
Scaled By Factor S	$C_1' = C_1/S$	$C_2' = C_2$	$C_3' = C_3$	$C_4' = C_4 S$

Table B.2: Summarizing the scaling laws

To test this theory, we ran simulations of an ICE sail with two different sizes: 500 μm and

1000 μm, found in Figure B.16. While there is some agreement, particularly with regards to C1, we note that our predicted scaling laws can be off by as much as 40%. The most likely cause of these such effects is that in the larger sail, the force abnormalities become even more prevalent and significant, further altering the optical forces beyond our expectations.

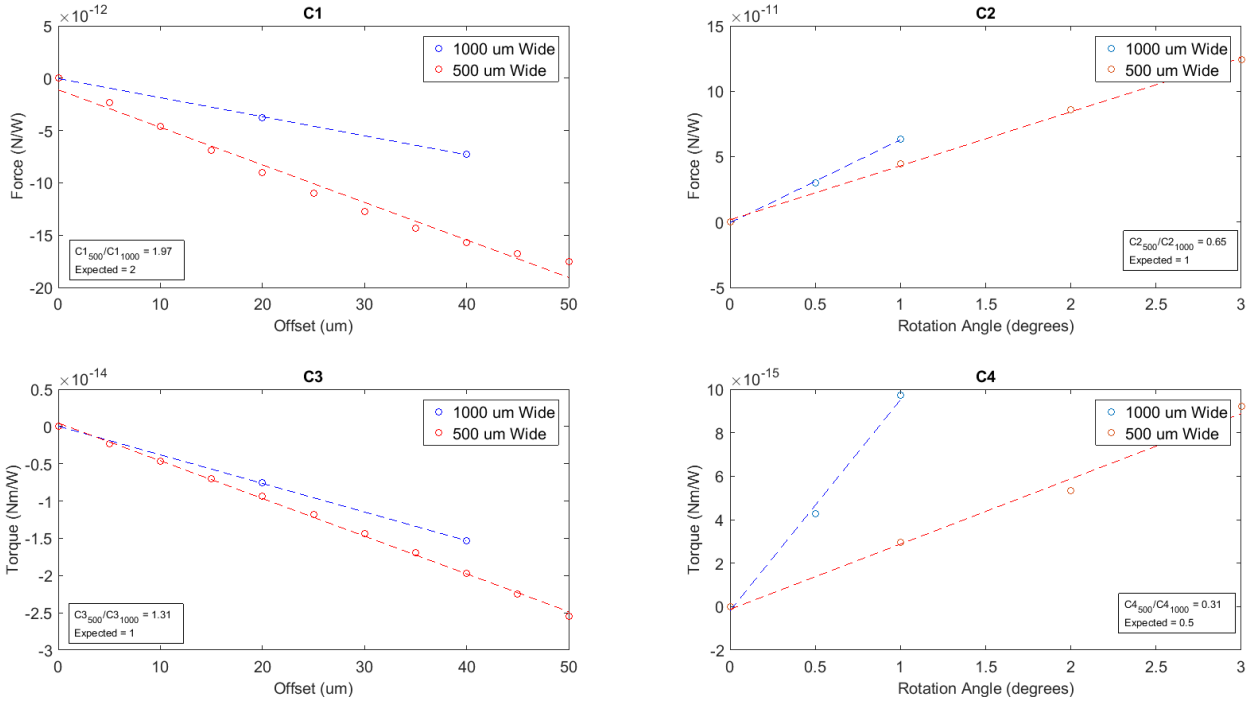

Figure B.16: Comparison of dynamic force coefficients for 500 μm wide sail and 1000 μm wide sail

B.12 Temperature derived from Stefan-Boltzmann Law

The temperature of a material absorbing radiation can be approximated with the following equation

$$\frac{P}{A}a = \epsilon\sigma T^4 \tag{B.4}$$

where P is the beam's power, A is the surface area, a is the absorption, ϵ is the emissivity, σ is the Stefan-Boltzmann constant, and T is the temperature of the sail. By rearranging the equation, we find that $T = \sqrt[4]{\frac{P}{A\epsilon\sigma}a}$.

Appendix C: Supporting Information of: Using Bottom-Up Lithography and Optical Non-Locality to Create Short-Wave Infrared Plasmonic Resonances in Graphene

C.1 Discussion of Block Copolymer Choice and Pyrenebutryic Acid Interfacial Layer

[1]

We selected poly(styrene-b-methyl methacrylate) as the BCP to fabricate graphene nanostructures on SiO2 substrates due to the nearly equal surface energies of polystyrene (PS) and poly(methyl methacrylate) (PMMA) blocks, which makes thin-film assembly feasible, and the good reactive ion etch selectivity of PS to PMMA (1:2).[104] Typically, inducing vertical orientation in the BCP domains on a substrate requires altering the surface to be energetically non-preferential to either blocks. We used a neutral layer chemistry developed by Han et.al.[143], based on a random copolymer poly(styrene-r-methyl methacrylate-r-glycidyl methyl methacrylate), abbreviated as RCP. However, the RCP does not wet the surface of graphene, leading to dewetting of the film (see Figure C.1). The precense of the pyrenebutryic acid (PBA) increases the graphene wettability for RCP and BCP deposition. The pyrene ring effectively binds to graphene by - stacking interactions while the carboxylic acid group is directed away from the substrate to alter graphene wettability. The polar carboxylic

[1]This section is a reproduction of an already published work found in [25]. The text and figures are unaltered, except for formatting changes.

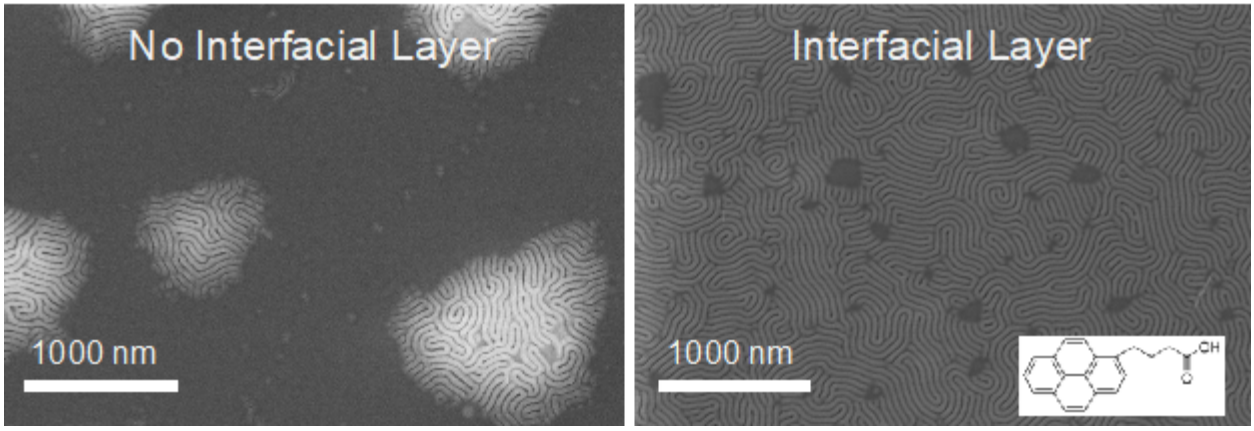

Figure C.1: SEM images illustrating the effect on pyrenebutyric acid (PBA) on BCP self-assembly. Only the substrate with PBA in between graphene and the polymer thin film shows large area self-assembly.

acid groups provide the hydrophilicity needed for deposition of subsequent copolymer films. Pyrene-containing moieties have been used to functionalize conjugated carbon allotropes such as graphene[144, 145] carbon nanotubes[146, 147] and C-60[148] via π–π stacking, with the goal of altering the surface wettability and chemistry to anchor specific molecules for biosensing or selective doping.

C.2 Calculating Width of Graphene Nanoribbons

To measure the widths of our of GNRs, we used both SEM and AFM as described in this section. Additionaly, as noted in the main text, the actual widths of the smallest GNRs would need to be almost one-half of what is measured in SEM to account for the observed, which is beyond the uncertaintly of our measurements. While there is some chance that the GNR ribbons are damaged on the edge, we note that previous measurements of GNRs prepared using e-beam lithography combined with an RIE etch did not show such edge damage. In those experiments, SEM imaging of the width provided values that agreed well with theory.[24] Finally, we note that RIE is a directional etch method, and AFM measurements reveal that the PS etch mask is intact after the etch process. The blue shift we observe would require 4-6 nm of overetching beyond the boundaries that we observe in SEM, which would necessitate extreme RIE etch angles of 45 deg., which is inconsistent

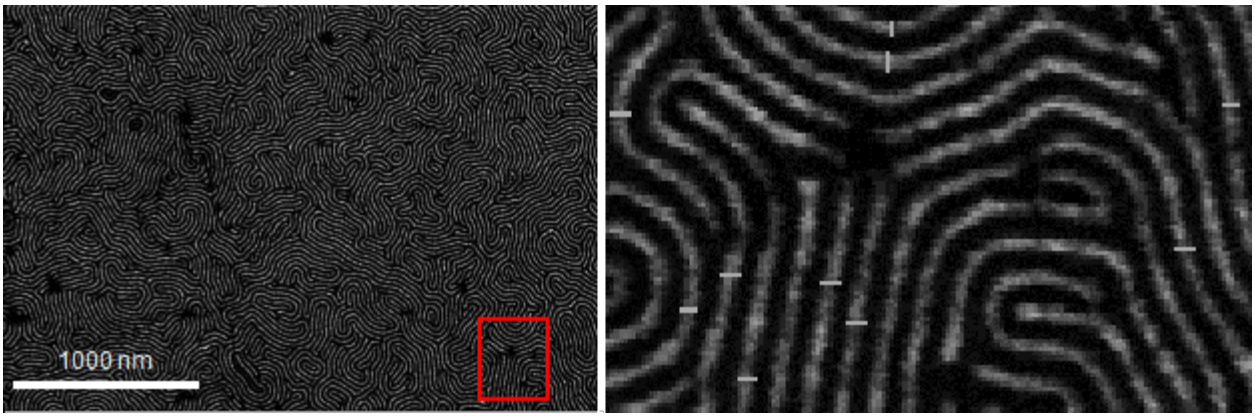

Figure C.2: Representative SEM image of smallest graphene nanoribbons. We get an average ribbon width of 12 +/- 2 nm, with our error representing standard deviation of averaged line widths plus pixel size image resolution added in quadrature.

with the RIE process. While a minor overetch is possible, it would not explain the observed deviations.

C.2.1 Calculating Width of Ribbons and Thickness via SEM

We measured the width of our graphene nanostructures using SEM image analysis. Using ImageJ software, we measured the width of these graphene nanoribbons by averaging 20 different ribbons. We report our errors as standard deviation plus pixel size image resolution added in quadrature. We considered ribbon width area using binary contrast transformation cutoffs in ImageJ. Using Figure C.2 as an example, we get a graphene nanoribbon width of 12 +/- 2 nm.

C.2.2 Estimating Width of Ribbons and Thickness via AFM

We measured the height of our ribbons, including any residual mask polymer with an UHV cryogenic AFM at 4K as shown in Figure C.3. We can see that there is the finger-print pattern, indicative of the BCP ribbons. From this measurement extract the height difference between the valleys (no graphene) and the peaks (graphene with polymer) and an estimate of the ribbon thickness. Measurements were done using Gwyddion software. We found the height to be 2+/-0.5nm. Noting that graphene is approximately 0.3 nm thick, we estimate

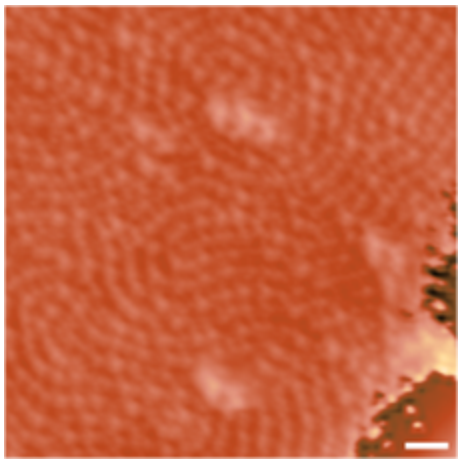

Figure C.3: Representative AFM image of smallest graphene nanoribbons. Using Gwyddion software we measure the width of these graphene nanoribbons and the residual polymer height. Scale bare is 50 nm.

the height of the remaining polymer as 1.7 +/- 0.5nm. This means that the residue on the surface of the GNRs are the Pyrene and the Neutral layer. For this device, we found a ribbon width of 13.1 +/- 1.3 nm, comparable to the SEM measurements of the device at 13 +/- 2 nm.

C.3 Removing Polymer Mask

In Figure C.4, we show three different methods to clear off the residual polymer on the surface. Vacuum annealing left a large amount of residual polymer on the surface. Commercial photoresist strippers like AZ 400T NMP-based solvent removed more of the polymer mask, but still left residual polymer and regions of the substrate showed GNRs that delaminated from the SiO2 surface. The oxygen plasma etch left a thin layer of polymer on the surface, but no graphene ribbons shifted during the removal process.

C.4 Fabrication and Measurement of Nanoperforated Graphene (NPG)

NPG samples were fabricated with a minor modification of the GNR process with a replacement of the BCP used. Instead of the lamellar-forming Ps-b-PMMA to form ribbons, 21.5k-

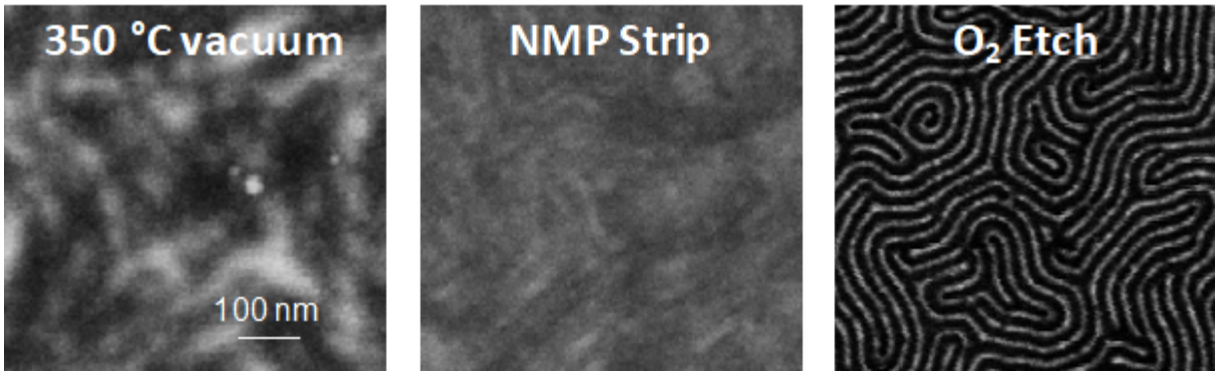

Figure C.4: SEM images of various attempts to remove the polymer mask after pattern transfer to graphene. Scale bars are the same for all SEM images.

10k MW for cylindrical-forming PS-b-PMMA was used to form perforations. These samples were electrostatically gated and showed a blue-shift at increased Fermi-levels, matching the behavior of the GNRs (see Figure C.5).

C.5 Electrostatic Gating to tune the Fermi Level of Samples

There were two methods available for doping the graphene samples: an ionic gel and a backgate. Due to the increased range of doping levels among other issues discussed in this section, the ionic gel data was used in the main text.

C.5.1 Ionic Gel

To dope the graphene with an ionic gel, the surface is coated with an ionic liquid (DEME) and the graphene is separated into two regions. These regions will act as electrode and count-electrodes. By applying a voltage bias between the two electrodes, the ions in the ionic liquid will gather on one of the electrodes and charge of opposite sign will build up on the other set of electrodes, doping the graphene. We can measure the source/drain current across the electrode to measure the resistance of the graphene. See Figure 3.1b in main text for schematic.

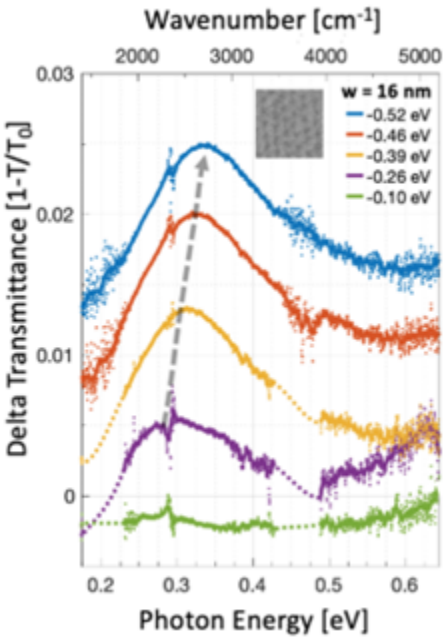

Figure C.5: Backgate-induced doping of 16 ± 3 nm wide NPGs with SEM inset. Gray arrow follow the peak shift as the Fermi level is shifted. Dashed colored lines indicate regions where the signal strength was small due to atmospheric effects.

C.5.2 Backgated Geometry

As an alternative to the ionic gel geometry used in the main text, we also made use of an electrostatic back-gate to dope the graphene. See Figure C.6 for the schematic. In this method, a voltage bias (VG) is applied between the graphene and the substrate (Si). This configuration is equivalent to a capicator, so by applying a voltage, charge will build up on the graphene, doping it. In this electrical set-up, a maximum doping corresponding to a Fermi level of 0.59 eV was achieved.

Measurements from a GNR sample gated with the backgate configuration can be seen in Figure C.7. Similar to the ionic-gel data in the main text, the plasmonic resonance blue-shifts as the doping in the system is increased. The plasmonic resonance was tuned to a frequency as high as 3800 cm-1 (2.6 m), the maximum we were able to achieve with the backgate geometry and our smallest ribbons at 12 nm. If we compare the data in Figure C.7 and Figure 3.2c from the main text, the resonance shift as a function of doping level is significantly smaller in the backgated sample than those gated by the ionic gel. We attribute

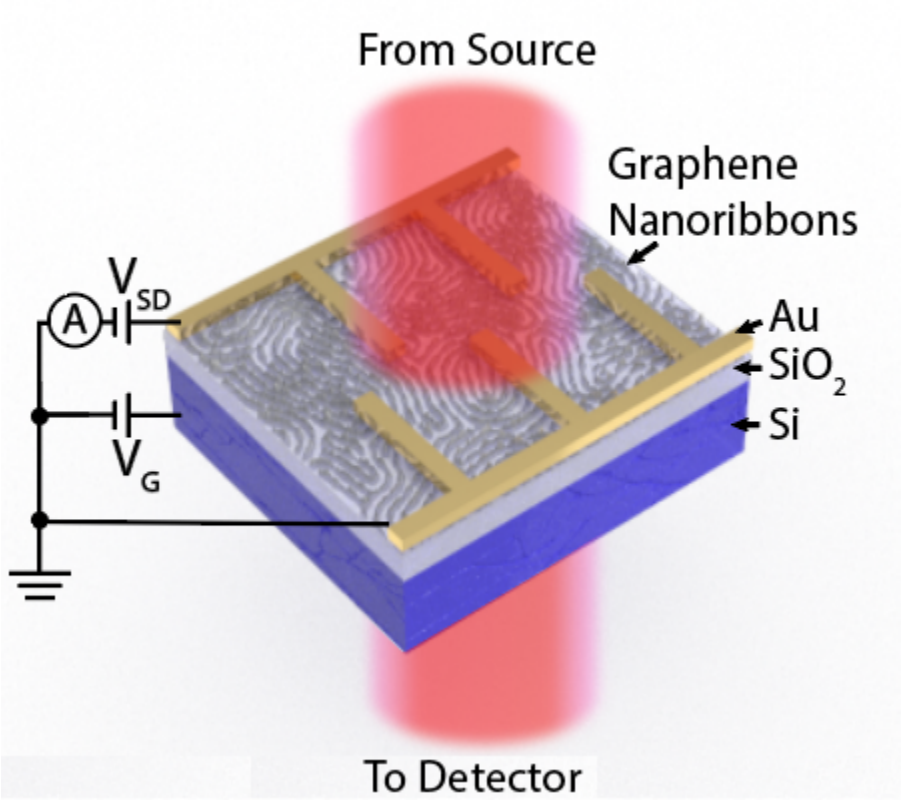

Figure C.6: Schematic of back-gate geometric configuration with SEM inset of the GNRs.

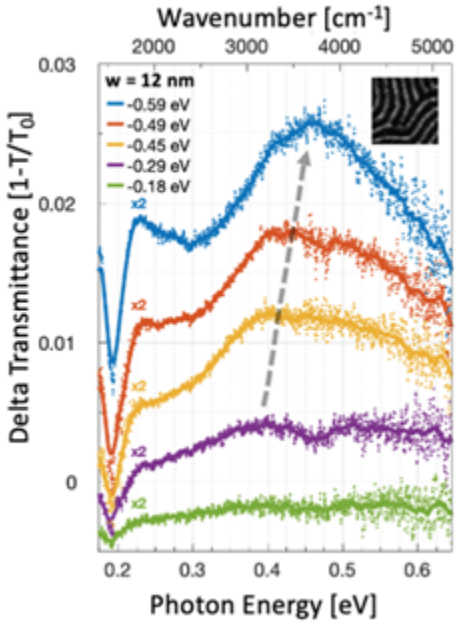

Figure C.7: Modulation of transmittance through graphene nanostructures by electrostatically doping the graphene with a backgate geometry. GNRs were 12 ± 2 nm wide. Gray arrow follow the peak shift as the Fermi level is shifted.

these effects to inhomogeneous doping in the samples, which changes the local Fermi level. For electrostatic-gate measurements, inhomogeneous doping creates an averaging effect of multiple Fermi levels, whereas the ionic gel can screen these charge inhomogeneities and maintain a constant Fermi level across the sample (see C.7). An attempt was made to measure this sample using the ionic gel as it consisted of our smallest ribbons, but the sample was damaged during processing and no further measurements could be made.

C.6 Measuring Fermi Levels

To understand the doping of our samples, we employed two approaches in tandem which find the charge neutral point and the Fermi levels directly. S6.1 Measuring the Charge Neutral Point

In the first approach, we varied the applied voltage (works for both backgated and ionic gel samples) until we found a resistance maximum, corresponding the charge neutral point. This is shown in Figure C.8. One problem we experienced with backgating was that the CNP

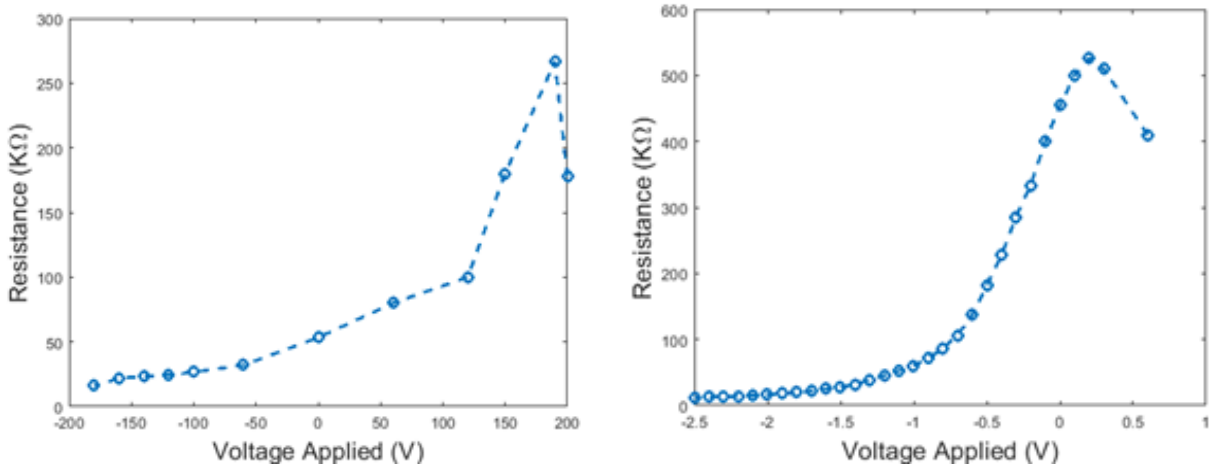

Figure C.8: Representative resistance curves of a backgated (left) and ion-gel (right) doped samples. The presence of the peak in the curve corresponds to the CNP.

would be beyond the dielectric breakdown voltage of the oxide on sample, at approximately 200V -although the exact voltage was sample dependent. As the CNPs we were able to measure were around this breakdown voltage, we expect the CNPs of the other samples to be at similar values, but past the breakdown voltage of the sample.

C.7 Measuring the Drude Peak

We can also directly measure the Fermi level of our graphene structures by measuring the Drude peak, seen in Figure C.9. Due to Pauli blocking, there will be increased transmission up to a threshold photon energy of $2E_F$, where interband transitions begin to occur. This feature can be identified as the region of maximum slope of the Drude peaks. Gating the graphene to increase the carrier density will shift location of this feature to a higher energy, as expected.

C.8 Modeling Reduced Plasmon Dispersion

As noted in C.5.2, we observed a crowding behavior where the estimated Fermi levels in backgated samples were much less dispersive than the theoretical Fermi levels based on the observed plasmonic resonances. We believe this effect to be due to the ribbons on a

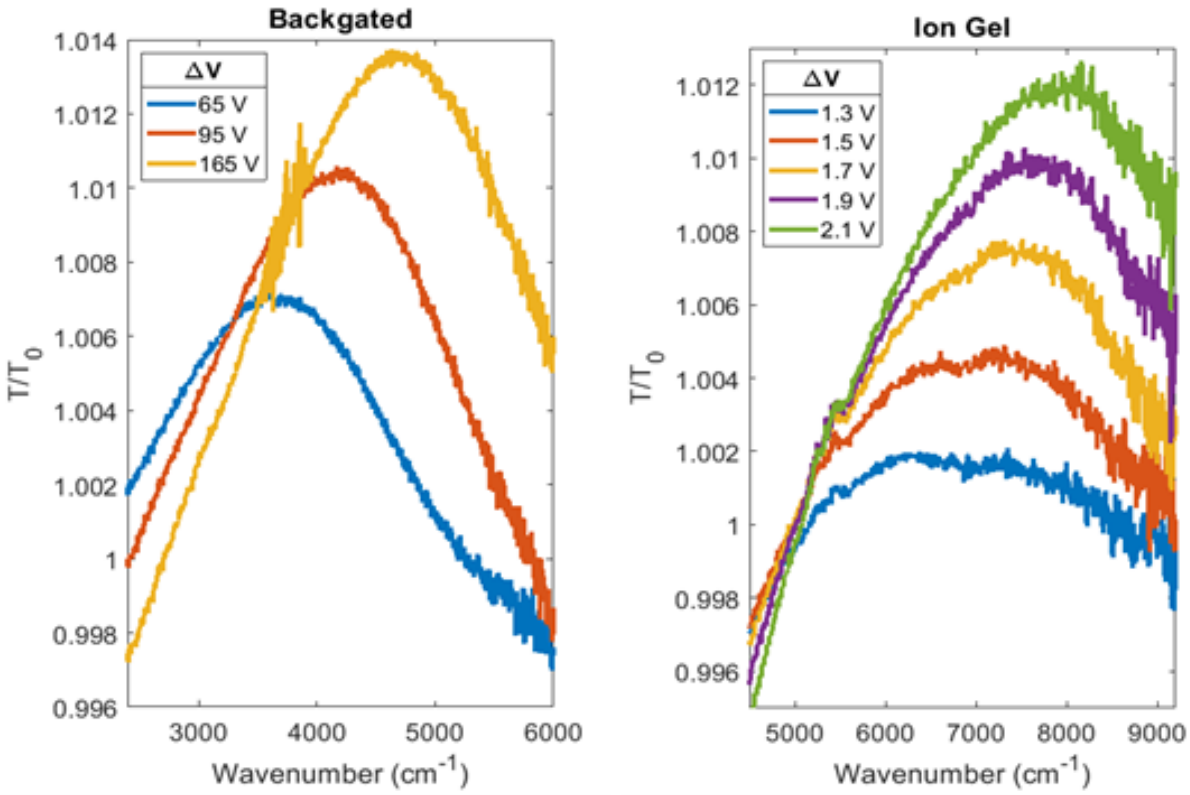

Figure C.9: Representative Drude spectrum of a backgated (left) and an ionic gel (right) doped nanostructured graphene.

single sample not sharing the same background doping caused by our fabrication process introduction of charge inhomogeneity. This effect only occurred in our backgated samples as the ions in the ionic gel can screen charge inhomogeneities to maintain a constant CNP across the graphene eliminating the biasing effect. To model this effect, we simulated two sets of ribbons sizes (12 and 30 nm), each with three different background doping levels (0.4, 0.45, 0.5 eV), corresponding to CNP's at approximately 160, 200, and 245 V. For the gating measurements, we control the measurement voltage, but that will apply a different doping level dependent on the background doping of the graphene, which is detailed in Table C.1.

	Measurement Voltage (V)	120	0	-120
CNP (V)				
245		0.356653	0.499314	0.609449
200		0.285322	0.451134	0.570645
160		0.201753	0.403507	0.533789

Table C.1: Doping levels of the GNRs for different CNPs at different measurement voltages. The colors correspond to the lines in Figure C.10.

In Figure C.10, we plot the weighted sum (our effective measured spectra) of the GNRs for three different measurement voltages. The left figure is for 12 nm ribbons, and the right is for 15 nm ribbons. For this representative example, we set the weighting of 0.4 eV to 2/3, 0.45 eV to 1/5, and 0.5 to 2/15. As we can see, our "measured" spectra have resonance peaks much closer together than the spectra of the ribbons at one Fermi level.

C.9 Comparison of Simulated Spectra to Measured Spectra

We modeled our graphene nanostructures using both local and non-local models for the graphene, by using FDTD (local) and FEM (non-local) simulations to calculate the frequency-dependent transmittance of the graphene nanostructures for different doping levels. In the

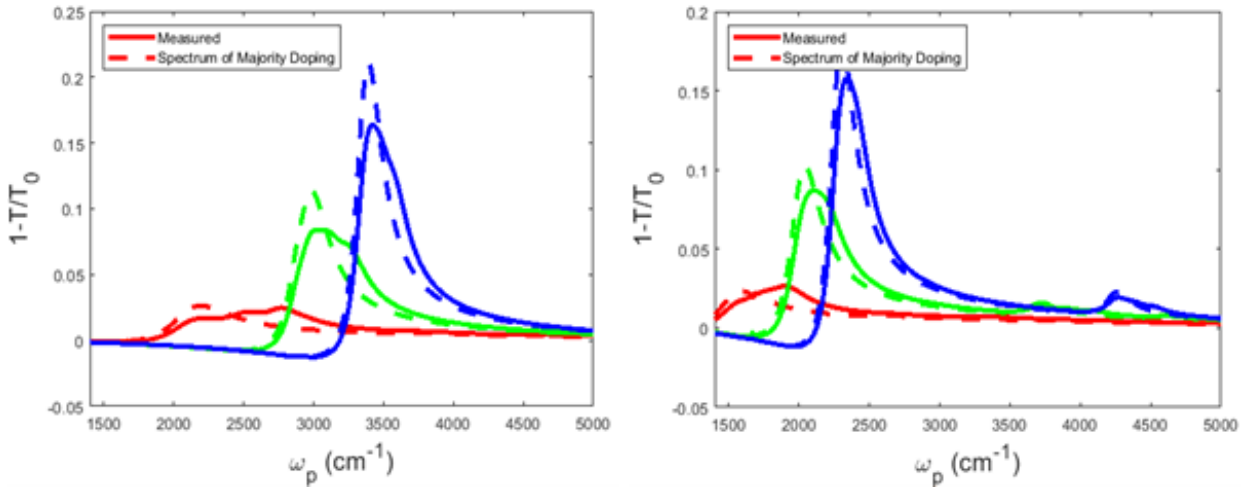

Figure C.10: Comparison of spectra of GNRs with single background doping (solid), set to majority doping value, compared to spectra of the weighted sum (dashed lines). 12 nm (left) and 30 nm (right) were considered.

main text, we used those simulations to infer the theoretically predicted resonance peak position (plotted as lines in Fig. 3) by selecting the maximum of the calculated Transmittance function. In figure C.11, we plot the full theoretical spectra, and directly compare them to experimental spectra from GNRs with the same parameters (width, width variance, doping level). The left and right hand figures shows the results for 29 nm and 13 nm ribbons, respectively. For the 13 nm ribbons, we include theoretical results from both non-local and local simulations, illustrating how non-local effects can blue-shift the spectral features. We note that these calculations include broadening due to GNR width inhomogeneity, but they do not include broadening due to doping inhomogeneity, which we could not measure directly. Doping inhomogeneity, defect and edge scattering, and reduced mobility can all contribute to the larger experimental linewidths that we observe in comparison to theory.

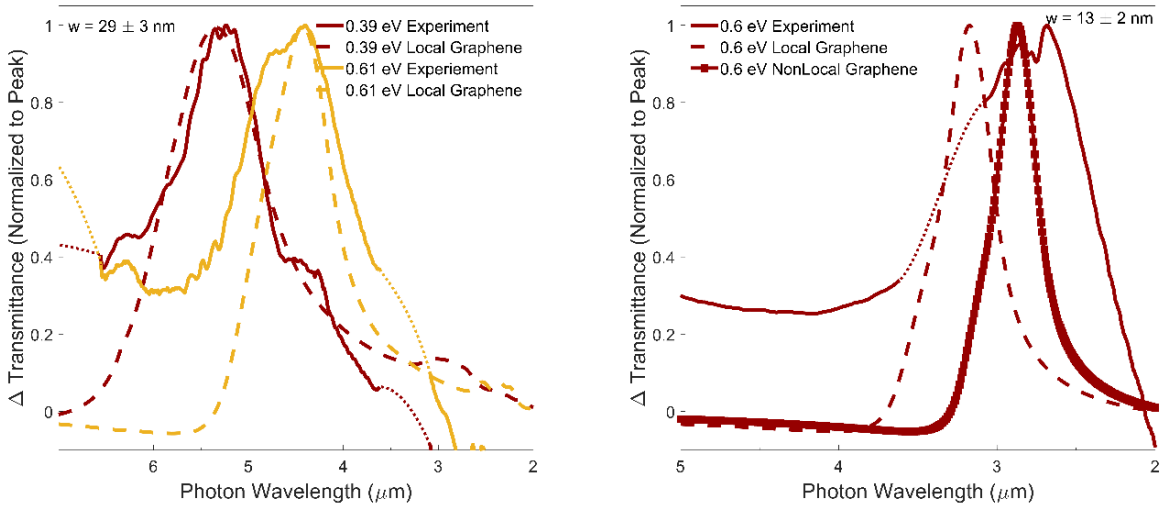

Figure C.11: Comparison of spectra of GNRs of simulations to experimental measurements. In the left figure, measurements of the 29 nm ribbons at two different doping levels (0.39 and 0.61 eV) are compared to the simulations using the local model of graphene. In the right figure, measurements of the 13 nm ribbons at a single doping level (0.6 eV) are compared to the simulations using the local model of graphene and the non-local model of graphene. These results are normalized to the peak value.